REVIEW

Biologically inspired artificial eyes and photonics

View the article online for updates and enhancements.

IOP ebooks™

Bringing together innovative digital publishing with leading authors from the global scientific community.

Start exploring the collection−download the first chapter of every title for free.

Review

Biologically inspired artificial eyes and photonics

Jae-Jun Kim[1], **Hewei Liu**[1], **Alireza Ousati Ashtiani**[1]
and Hongrui Jiang[1,2,3,4,5]

[1] Electrical and Computer Engineering, University of Wisconsin-Madison, Madison, WI 53706, United States of America

[2] Materials Science and Engineering, University of Wisconsin-Madison, Madison, WI 53706, United States of America

[3] Biomedical Engineering, University of Wisconsin-Madison, Madison, WI 53706, United States of America

[4] Ophthalmology and Visual Sciences, University of Wisconsin-Madison, Madison, WI 53706, United States of America

[5] McPherson Eye Research institute, University of Wisconsin-Madison, Madison, WI 53706, United States of America

E-mail: hongrui@engr.wisc.edu

Abstract

Natural visual systems have inspired scientists and engineers to mimic their intriguing features for the development of advanced photonic devices that can provide better solutions than conventional ones. Among various kinds of natural eyes, researchers have had intensive interest in mammal eyes and compound eyes due to their advantages in optical properties such as focal length tunability, high-resolution imaging, light intensity modulation, wide field of view, high light sensitivity, and efficient light management. A variety of different approaches in the broad field of science and technology have been tried and succeeded to duplicate the functions of natural eyes and develop bioinspired photonic devices for various applications. In this review, we present a comprehensive overview of bioinspired artificial eyes and photonic devices that mimic functions of natural eyes. After we briefly introduce visual systems in nature, we discuss optical components inspired by the mammal eyes, including tunable lenses actuated with different mechanisms, curved image sensors with low aberration, and light intensity modulators. Next, compound eye inspired photonic devices are presented, such as microlenses and micromirror arrays, imaging sensor arrays on curved surfaces, self-written waveguides with microlens arrays, and antireflective nanostructures (ARS). Subsequently, compound eyes with focal length tunability, photosensitivity enhancers, and polarization imaging sensors are described.

Keywords: artificial eyes, photonics, biomimetics, mammal eyes, compound eyes, optics

(Some figures may appear in colour only in the online journal)

1. Introduction

The eye is one of the most essential organs to those animals that have eyes, owing to its ability to extract useful information of objects or the surrounding environment from the light. Whether the information is from a simple pit eye of a flatworm with low-resolution vision or from a corneal lens eye of an eagle with an acute vision, all kinds of information obtained from their eyes can help the owners to plan their next behavior and make critical decisions for their survival. Although the information extracted from the eye is useful, all eye-possessing animals have different kinds and levels of vision systems because their eyes have evolved depending on their demands, environment, visual information processing capacity, and usefulness of the visual information in improving their behavior [1]. As a result, researchers have been mostly interested in mammal eyes and compound eyes rather than other simpler ones among the various types of eyes, for the more complicated functions that these two categories of eyes can provide.

In the past decades, many researchers have studied mammal eyes and compound eyes, and a variety of photonic devices were inspired by these natural visual systems (figure 1). In developing optical systems, scientists and engineers have only spent centuries perfecting the glass-based optics; yet natural eyes have been evolving for millions of years. Therefore, from antireflection to image sensing, natural living organisms usually have better performance than those artificial approaches. For example, the lens of the human eye is a natural miniaturized tunable-focus lens with a wide focal range by changing its shape, and the curved retina also significantly reduces the aberration. Moreover, the human eye provides foveal vision that sees a small field at much higher resolution than the rest of the field of view (FoV). These specifications cannot be achieved by the traditional refractive glass lenses and image sensors. The compound eyes exhibit a wide FoV and great sensitivity in an extremely small form factor. Furthermore, antireflective nanostructures (ARS) of some compound eyes effectively reduce the light reflectance on the surface of the eye, which can improve the light sensitivity as well as reduce the visibility of the owners to predators. These intriguing features of the animal eyes have inspired researchers to develop bioinspired artificial eyes and photonic devices for various applications.

Thanks to the huge progress in micro- and nano-technologies as well as materials science, researchers have succeeded in mimicking the key optical components of the mammal eyes (the tunable lens, the retina, and the tunable iris) (figure 1(a)) and the compound eyes (microlens or micromirror arrays, waveguides, photoreceptor cells, and ARS) (figure 1(b)). The schematic illustrations in the boxes in figure 1 show representative bioinspired photonic devices that mimic the key optical components of natural eyes. Since most of the bioinspired photonic devices focus on reproducing the key functions rather than anatomical structures of the natural eyes, the dimensions or materials of the devices are not limited to those of natural eyes. Hence, a wide spectrum of research has been conducted to develop advanced photonic devices for numerous different kinds of applications, including not only

imaging devices but also light intensity modulators, solar cells, light-emitting diodes, and biomedical devices. Detailed descriptions of these works will be presented in the following sections in this review.

First, we introduce visual systems in nature, including mammal eyes and compound eyes, in section 2. In the rest of this article, we provide an overview of previous research on bioinspired visual systems. The photonic devices including tunable lenses, curved image sensors, and tunable irises are described in section 3. Bioinspired compound eyes fabricated on planar and curved substrates and integrated with image sensors are presented in section 4. Other types of bioinspired visual systems including compound eyes with tunable lenses, high-sensitive photodetectors, and polarization detectors are introduced in section 5. Conclusions and perspectives of bioinspired visual systems are given in section 6.

2. Visual systems in nature

2.1. Mammal eyes

The mammal eye is one of the most well-known natural visual systems due to the research interest in its attractive optical features as well as ophthalmology. The main optical features of the mammal eye are focal length tunability (accommodation), high-resolution imaging with low aberration, and light intensity modulation (adaptation).

The mammal eye can adjust focal length by changing the curvature of the crystalline lens using ciliary muscles and zonular fibres. When the ciliary muscles contract, the radial tension of the zonular fibres is released, so that both the curvature and the focal length of the crystalline lens decrease. On the contrary, when the ciliary muscles relax, the zonular fibres are stretched, so that the crystalline lens assumes a more flattened shape that has longer focus. Studies of the human eye have shown that the mean amplitude of accommodation is about 15 dioptres (corresponding to an ability to focus from about 7 cm to infinity) at the ages 2–4 years [2] and the reaction time of accommodation is about 300 ms [3]. Although the amplitude of accommodation declines with age, the human eye generally can offer a wide range of focal length adjustment with fast response time.

The retina of the mammalian eye can produce high-resolution images with low aberration due to its curved image surface. The resolution of the eye is related to the spacing between the photoreceptor centres (s) and the focal length (f) of the crystalline lens (the focal length is the distance from the image to the nodal point where rays pass through without refraction by the lens). As shown in figure 2(a), the eye can resolve black and white parts of a grating if the period of the image of the grating on the retina is $2s$. Thus, the resolvable period of the grating is $2\Delta\varphi = 2s/f$, which is expressed as an angle. In addition, the resolvable spatial frequency is $1/(2\Delta\varphi) = f/2s$. This equation indicates that the resolvable spatial frequency as well as the resolution of the eye can be increased by increasing the focal length and/or reducing the spacing between the photoreceptors. Because of this relationship, the human eye is relatively large and has small
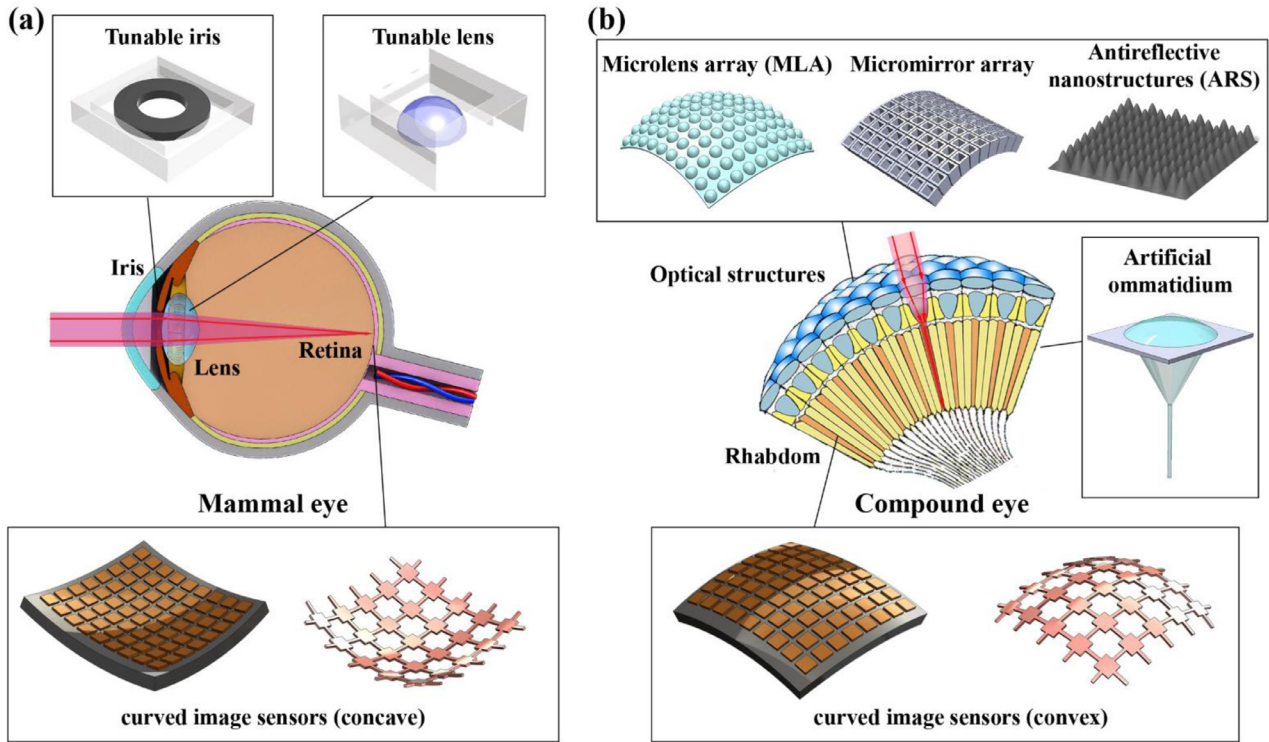
Figure 1. Schematic illustrations of natural eyes ((a) a mammal eye and (b) a compound eye) and bioinspired photonic devices that mimic the key optical components of natural eyes.

photoreceptors (about 2 μm in diameter). The size of the photoreceptors is not smaller than 2 μm because further reduced size of the photoreceptors would cause light leakage.

The pupil of the mammal eyes can modulate the light intensity by changing its size. The human pupil can change its size from 2 to 8 mm in diameter, which modulates the light intensity by a factor of roughly 16 [4]. The pupil constricts in response to bright light in about 1 sec and dilates in response to darkness more slowly (several tens of seconds) than constriction.

2.2. Compound eyes

2.2.1. Apposition compound eyes. A natural apposition compound eye is composed of an array of optical units called ommatidia. Each ommatidium consists of a facet lens, a crystalline cone, a light-guiding rhabdom, and photoreceptor cells. The omnidirectional arrangement of the ommatidia facilitates wide FoV detection. In addition, the compound eye has opaque walls with pigment to prevent cross-talk between adjacent ommatidia that would produce ghost images or contrast reduction.

Kirschfeld described the relation between the resolution and the size of the compound eye by combining the following three equations [5].

$$\Delta r = 1.22 \, \frac{\lambda}{D} \tag{1}$$

$$\Delta \Phi = \frac{D}{R} \tag{2}$$

$$\Delta \Phi_{\mathrm{s}} = \frac{\lambda}{2D} = \frac{\Delta r}{2.44} \tag{3}$$

where Δr is the radius of Airy disk, λ is the wavelength of light, D is the diameter of the microlens, $\Delta \Phi$ is the interommatidial angle, R is the radius of the compound eye, $\Delta \Phi_{\mathrm{s}}$ is the sampling interval. Equation (1) describes the diffraction limit of the compound eye, (2) represents a geometric relationship (figure 2(b)), and (3) states the optimal condition considering optical and anatomical resolution. After combining the equations (1)–(3), Kirschfeld obtained

$$\frac{1}{\Delta r} = \left[\frac{R}{2.98\lambda} \right]^{1/2} \tag{4}$$

This equation indicates that the resolution of the compound eye increases only with the square root of the eye size, compared to the resolution of the mammal eye, which increases linearly with the eye size. Thus, the compound eye would need about at least a 1 m diameter to achieve the same angular resolution as the mammal eyes. Although the compound eye cannot provide high-resolution images, it has other intriguing features such as low aberration imaging, huge depth of field, and high motion sensitivity [1, 6, 7].

2.2.2. Superposition compound eyes. A natural superposition compound eye has a clear zone between the photoreceptor cells and the optical structures that can refract or reflect the incident light. Therefore, the light through the multiple optical structures can be focused onto certain spots on the surface of photoreceptor cells to form a single erect image (figure 2(c)). Thanks to this anatomical difference from the apposition
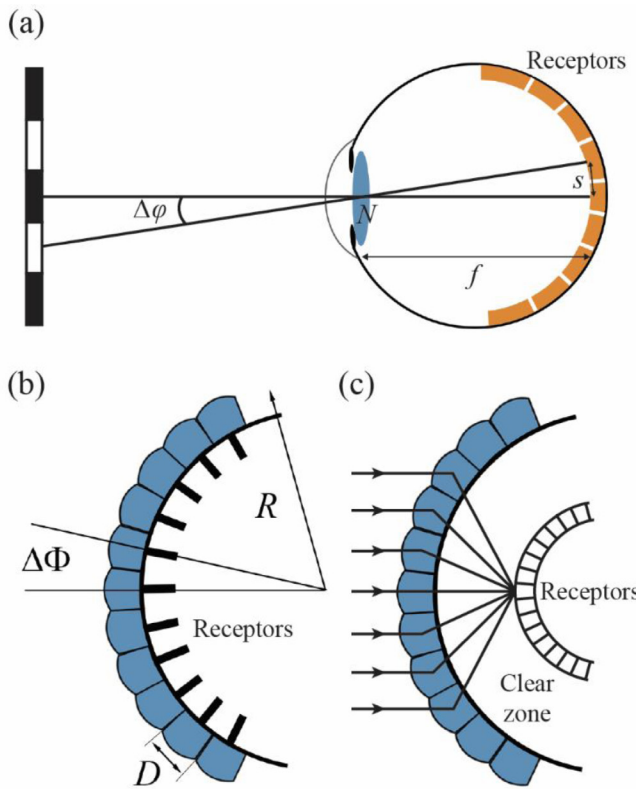
Figure 2. Visual systems in nature. (a) A mammal eye and the finest grating that the mammal eye can resolve. The angular period of the grating is $2\Delta\varphi$. N is the nodal point. f is the focal length. s is the spacing between the photoreceptor centres. (b) An apposition compound eye. $\Delta\Phi$ is the interommatidial angle. D is the diameter of the microlens. R is the radius of the compound eye. (c) A superposition compound eye that has a clear zone between the optical structures and receptors. The clear zone allows focusing of the light through the multiple optical structures.

compound eye, which has optically isolated ommatidia, the superposition compound eye has better light sensitivity than the apposition one. Hence, unlike the apposition compound eye that is found in most diurnal insects, the superposition compound eye is commonly found in nocturnal insects and deep-water crustaceans that live in dim environments.

3. Bioinspired mammal eyes

Image-forming eyes in mammals are one of the most delicate and complicated organs, which may have been evolving for millions of years since the first fossil of eye found to date was from the early Cambrian (about 530 million years ago) [1]. The many different components of the mammal eyes have attracted scientists and physicians in the past centuries to study their functions and how they came into existence. Among the optical components of the mammal eyes, scientists and physicians paid particular attention to first the crystalline lens (as early as second century A.D.) and later on, the retina (starting from sixteenth century B.C.), as the main components of vision. Developing optical apparatus inspired by mammal eyes has also been going on for centuries, starting from pin-hole cameras (camera obscuras), then to photographic cameras.

The past decades witnessed tremendous improvement in camera design and technology with the invention and evolvement of semiconductor imaging sensors. With the recent advent of tunable optical devices, including lenses and irises, as well as curved imaging sensors, another era of enormous advancement in camera technology is foreseeable.

3.1. Tunable lenses

3.1.1. Hydrogel actuators.
Stimuli-responsive hydrogels have enormous potential in many fields due to their properties of large mechanical deformation, reversible volumetric change, and responsiveness to various stimuli including temperature, pH, light, pressure, electric field, and external chemicals. Taking advantage of the stimuli-responsive hydrogels, Jiang's group demonstrated many types of tunable liquid microlens devices, using stimuli-responsive hydrogels as actuators [8–15], inspired by ciliary muscles of human eye, to tune the shape of curved liquid-liquid interfaces and hence focal length of the resultant liquid microlenses.

Dong *et al.* first demonstrated a tunable liquid microlens system using temperature- (NIPAAm, N-isopropylacrylamide) and pH- (AA, acrylic acid; DMAEMA, 2-(dimethylamino) ethyl methacrylate) responsive hydrogel [8]. This system, shown in figure 3(a), consists of a hydrogel ring, microchannels, glass plates, and an aperture slip. Water was injected through the microchannels and a water droplet was confined within the hydrogel ring. The whole structure was then covered with silicone oil. The water–oil meniscus, and as a result, a liquid microlens, was thus formed by and pinned at a hydrophilic–hydrophobic (H–H) boundary between the hydrophilic bottom and sidewall surface of the aperture ('ca') and the hydrophobic top surface ('ts'). When the hydrogel ring was activated by its stimulus, here temperature or pH, the volume of the hydrogel ring underwent significant changes, and this led to a volumetric change of the water droplet in the central part of the ring. Such volumetric change in the water droplet in turn resulted in a change of the lens curvature due to the H–H boundary and tuned the focal length of the microlens. When the microlens was divergent and convergent, the focal length was changed from $-\infty$ to -11.7 mm and from 22.8 mm to $+\infty$, respectively. The response time of the hydrogel actuators were a few to tens of seconds. Slow response time is one of the important limiting issues of hydrogel actuators to be addressed. Miniaturization of the hydrogel structures is one solution to improving the response time. Zeng *et al.* studied the relationship between the response time and different structures of hydrogel actuators [12]. They showed that instead of the using one single hydrogel microactuator, for example, a hydrogel ring, forming multiple smaller hydrogel posts with similar total hydrogel volume had better response time, because the diffusion time required for smaller hydrogel structures is less.

After demonstrating the liquid microlens system using the ring-shaped hydrogel actuator and a fixed lens aperture, Dong *et al.* showed another design concept of liquid microlens using pH-responsive hydrogel microposts actuated in
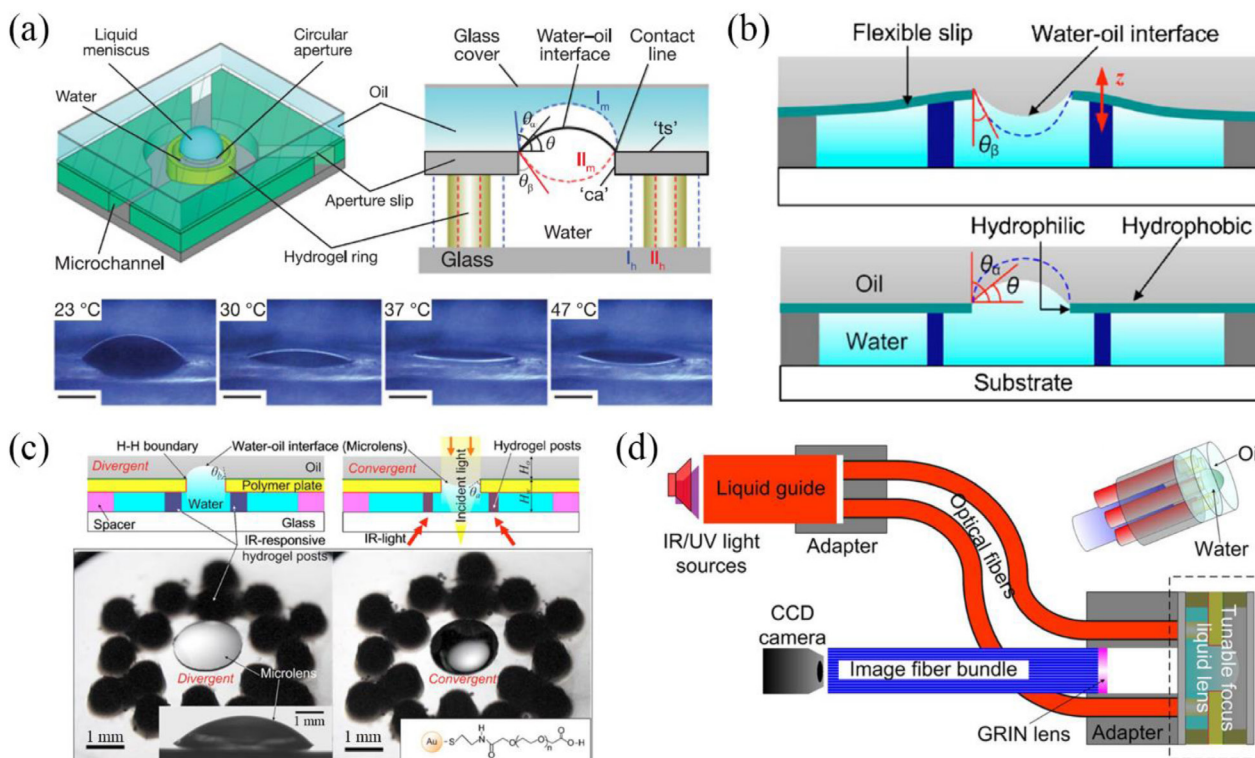
Figure 3. Hydrogel-actuator based tunable lenses. (a) Schematic diagrams of a liquid microlens actuated by ring-shaped stimuli-responsive hydrogels. Hydrophilic surface ('ca') and hydrophobic surface ('ts') of the aperture slip pin a water–oil interface along the contact line. Expansion and contraction of the hydrogel ring lead to a change in the curvature of the water–oil meniscus. Reprinted by permission from Springer Nature Customer Service Centre GmbH: Nature. [8] © 2006 (b) Working mechanism of a tunable microlens which uses pH-responsive hydrogel microposts and a flexible slip. Reprinted from [10], with the permission of AIP Publishing. (c) A tunable liquid microlens tuned by IR light-responsive hydrogel actuators. Reprinted from Zeng (2008) [11], with permission from American Institute of Physics and authors. (d) A fibre endoscope integrated with an IR-responsive tunable microlens system. © 2011 IEEE. Reprinted, with permission, from [13].

the perpendicular direction to the lens aperture and a flexible aperture slip (figure 3(b)) [10]. This liquid microlens system also used pinned H–H boundary to form a water–oil meniscus; however, the actuation mechanism is different from utilizing the hydrogel rings. The schematic diagrams of the working mechanism in figure 3(b) show the tuning of the curvature of the liquid microlens. When the hydrogel microposts were activated by the change in the pH value in the surroundings, the hydrogel microposts bent the flexible aperture slip upward by expansion or restored its position by contraction. Correspondingly, the water droplet could be in either concave or convex shape. Therefore, the hydrogel microposts with a flexible aperture slip could tune the focal length of the microlens. The focal length was varied from $-\infty$ to $-7.6\,\mathrm{mm}$ when the microlens was divergent and from $8.5\,\mathrm{mm}$ to $+\infty$ when the microlens was convergent. It is worth noting that the capillary length is many times longer than the lens aperture, so we can neglect the effect of gravity. For example, in the case of silicone oil and water, the densities of liquids are matched within 1%, which leads to a capillary length of around $27\,\mathrm{mm}$, more than one order of magnitude bigger than the lens aperture.

Using thermally driven NIPAAm hydrogel synthesized with gold (Au) nanoparticles that have a strong absorption of the infrared (IR) light and high heat efficiency, Zeng *et al.* developed a tunable liquid microlens tuned by IR light-responsive

hydrogel actuators (figure 3(c)) [11]. This tunable microlens system has the same mechanism as the previous systems but instead utilized a different stimulus to actuate the hydrogel. The IR light-responsive hydrogel microposts were photopatterned in a water container to actuate the microlens under IR light irradiation. The Au nanoparticles in the NIPAAm hydrogel absorbed the IR light and generated heat. The hydrogel then contracted in response to the heat. When the IR stimulus disappeared, the hydrogel expanded back to its original volume with the heat dissipated to the surrounding fluid. The volumetric change could tune the curvature of the pinned water–oil meniscus as in the previous microlens systems. Therefore, the focal length of the liquid microlens was controlled by the IR light. The tunable range of the focal length was from $-\infty$ to $-17.4\,\mathrm{mm}$ (divergent) and from $8.0\,\mathrm{mm}$ to $+\infty$ (convergent). This IR-responsive tunable microlens system has advantages in integration into other systems compared with other types of hydrogel actuators because it can be activated by light. As an example, it was integrated with a fibre endoscope and showed potential clinical benefit by integration in fibre endoscopes and provided clinically relevant images (figure 3(d)) [13].

Other research groups have also demonstrated different types of tunable lenses actuated by hydrogels. Duan *et al.* used bilayer hydrogels that possess swelling/deswelling

behaviors to fabricate a tunable lens [16]. The tunable lens fabricated by bilayer hydrogels could adjust the focal length by changing the pH conditions. Under high pH conditions, the lens-shaped hydrogels were in the contracted state, whereas the hydrogel disk formed between two lens-shaped hydrogels expanded, leading to an increased focal length. On the contrary, under low pH conditions, the lens-shaped hydrogels swelled, whereas the hydrogel disk shrunk, resulting in a decreased the focal length. The focal length of the tunable lens varied from 30.00 mm to 59.45 mm when the pH changed from 1 to 7. Wirthl *et al.* bonded transparent hydrogel sheets on both sides of a fluid-filled elastomeric lens to fabricate a tunable lens [17]. When applying a DC voltage to the hydrogel sheets, the lens was flattened and the focal length of the lens was increased by up to 110% compared to that without the applied voltage. The tunable lens showed relatively fast response time (in the 300 ms range) compared to other tunable lenses actuated by hydrogels.

3.1.2. Thermopneumatic actuators. In a thermopneumatic microlens, a gas-filled heat engine is used to drive the microlens [18–21]. A small air bubble in a sealed chamber is heated. In response to the temperature change, the air bubble expands and pushes the liquid onto a flexible membrane, as shown in figure 4. As a result, the flexible membrane bulges out, which changes the curvature of the diaphragm that is holding the liquid inside the lens chamber.

The fabrication of these microlenses are relatively straightforward. However, they generally suffer from a slow response time of around 2 min in the cool-down cycle [21]. The main factor that hinders agility of these microlenses is that they rely on natural convection to dissipate the heat.

3.1.3. Thermoelectric actuators. In the abovementioned microlens actuation, buoyancy forces acts on the bubble inside the lens chamber due to a large difference between the densities of the gas and the surrounding liquid. This in turn results in a microlens that is prone to vibration-induced aberration. Further, as mentioned above, these microlens actuators are inherently slow during the cool-down cycle, which makes them not quite practical in many applications. To tackle these two issues, a fully liquid, thermoelectrically driven microlens was proposed [22, 23]. In this design, as seen in figure 5, no air bubble is used and the actuation comes from a change in the density of the working fluid as a function of its temperature. Furthermore, this actuator has a very low aspect ratio; i.e. the depth of the actuation chamber is very small compared to the width and length of the device, which makes it faster as we will discuss later. Finally, since the device is equipped with a closed-loop controlled thermoelectric (TE) element, the temperature adjustment in both cooling and heating cycles can be fine-tuned to be made agile and stable at the same time.

The purely liquid-driven lens described above uses a TE element to control the temperature of the working fluid, in this case, water. Compared to using a resistive heater, the use of TE provides the benefit of temperature tuning in a bi-directional way; i.e. both increasing and decreasing. This essentially
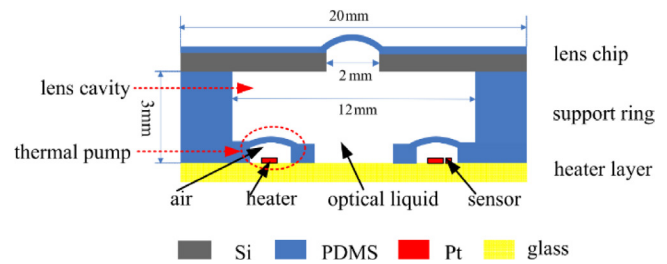

Figure 4. Schematic of a thermopneumatic tunable liquid lens. Reprinted from [23], with the permission of AIP Publishing.

circumvents issues related to slow cooling time of the heat engine of the device. The cross section is shown in figure 5. The device is laid on top of a glass slide, and multiple layers of photo-defined poly(isobornyl acrylate) (Poly-IBA) are laid to define device cavities. From the right, water is injected, passing through microfluidic channels, fills the heat engine in the middle, and then passes from another channel to reach the left side of the device. Water is pinned at the opening on the left. On top of that, a silicone oil (Dow Corning 550) droplet is injected into the shallow chamber on top of the water meniscus. This chamber and the water injection opening on the left are sealed with a thermoplastic polymer resin (polyethylene terephthalate, or PET) cap. When current passes through the TE element, depending on the current direction, the water either expands in volume when heated or shrinks when cooled. Since water can be assumed nearly incompressible in this device, the net result of this volume change in the working fluid is then reflected as a change in the shape of the pinned water meniscus, which in turn creates a tunable microlens. The optical performance of this device is shown in figure 6. As can be seen, the resulting device functions as a thermally controlled tunable microlens.

3.1.4. Electrohydrodynamic actuators. Thermopneumatic and hydrogel-based actuation mechanisms that are described in prior sections rely on the external (out of the lens) environment to cool down. A thermally actuated microlens inherently needs a heatsink to reject the heat generated when not needed. It is thus a challenge for these two driving methods to be harnessed in a micro-packaged device. If the miniaturization of the optical system is a must, one needs to look for an encapsulated actuation mechanism.

Electrohydrodynamically actuated microlens is a category of microlenses that solely rely on solid/liquid/electrostatic field interaction to alter the curvature of the microlens. In these drivers, an electrostatic field is generated via electrodes embedded in the microlens structure [24–29]. This field would in turn interact with two immiscible liquids and the resulting energy balance will define the shape of the liquid microlens. These types of microlenses can be further divided into electrowetting and dielectrophoretic (DEP) types based on the subtle differences in the driving mechanisms.

Electrowetting driven tunable microlenses are among the most well-known and widely studied types of liquid lenses. In typical applications, a conductive droplet is placed on an insulator, which in turn is placed on top of an electrode. This arrangement is usually called electrowetting on dielectric
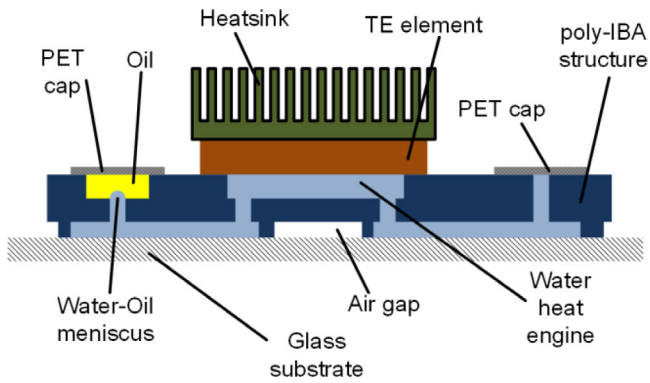
Figure 5. The cross section of a thermoelectrically driven tunable liquid microlens. On the left side, a small aperture pins a water meniscus. A water–oil meniscus is subsequently formed inside an oil chamber. This meniscus consisting of two materials with different refractive indices forms the microlens. An air gap between the heat engine and the substrate provides extra thermal insulation. Reprinted from Ousati Ashtiani [23], with permission from American Institute of Physics and authors.

Figure 6. The back focal length of a thermally controlled tunable microlens as a function of temperature. The back focal length has negative values since the microlens has a convex water-into-the-oil meniscus shape that forms a diverging microlens. The microlens shows a slight hysteresis, similar to electrowetting driven and some other liquid microlenses. Reprinted from [23], with the permission of AIP Publishing.

(EWOD) [25]. A schematic view of an electrowetting driven microlens is shown in figure 7.
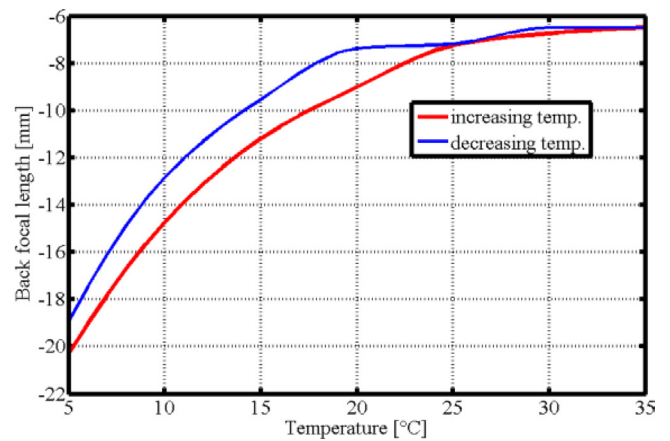
In an EWOD device, the conductive liquid and the electrode constitute a capacitor. By applying a voltage, charge is accumulated between the conductive liquid and the electrode. This charge accumulation at the insulator/liquid interface modulates the surface tension. Thus, the contact angle of a droplet on top of the solid surface varies accordingly. The relationship between the contact angle and the voltage follows the modified Young equation [30]:

$$\cos \theta = \cos \theta_Y + \frac{\varepsilon_0 \varepsilon_{\mathrm{d}}}{2d\sigma_{\mathrm{lv}}} U^2. \tag{5}$$

In equation (5), θ is the contact angle at an applied voltage U, θ_Y the contact angle at zero voltage, ε_{d} the dielectric constant of the insulator, ε_0 the vacuum permittivity, d the thickness of the insulator, and σ_{lv} the liquid/vapor surface tension. Since the volume of the droplet is constant, the change of the contact angle will induce a change in shape of the liquid droplet. Consequently, the curvature of the droplet will change and the focal length of the tunable microlens is altered. These flat electrode designs, although simple, does not provide any centring mechanism for the droplet to stay in the position during the actuation process. Therefore, other means of droplet centring must be incorporated into the device.

Based on the EWOD principle, various microlens structures have been proposed [25–28]. In almost all designs, the conductive liquid is surrounded by an immiscible and insulating liquid. This serves two purposes: (i) it prevents evaporation of the conductive liquid and (ii) it substantially reduces buoyancy forces that act upon the liquid droplet. As a result, gravity and other acceleration forces will not affect the shape of the droplet and the dominant force will be the surface tension. Ultimately, this results in a spherical shape of the liquid droplet.

In another embodiment of EWOD microlenses, a 3D structure is used [31]. As can be seen in figure 8, instead of having

a flat electrode, this design exploits conductive walls that are covered with an insulator. Such a 3D structure has the inherent advantage of liquid centring, since the droplet is physically confined in the middle of the chamber.

The robustness, simple construction, low power and good optical quality make this variable-focus microlens especially suitable for mobile applications. A potential drawback is, however, the complicated 3D structure of the device is poorly compatible with mass production in readily available fabrication facilities that are optimized for surface micromachining. Therefore, various planar structures have been proposed to tackle the difficulty in manufacturing.

As mentioned above, One of the main hurdles in fabricating an EWOD liquid tunable microlens with a centred optical axis comes from their complicated 3D structure. From the perspective of mass production, planar surface micromachining is preferred. Hence, it is highly desired to come up with a design that incorporates simple surface micromachining to create a self-centring, EWOD liquid tunable microlens. One such design is called areal density modulated electrode [32]. In this design, electrodes are arranged in such a way that provides a naturally favourable droplet position at the centre. In other words, the electrostatic actuation centres the droplet while at the same time tunes the curvature of the liquid microlens. The device structure is shown in figure 9(a) and the electrode arrangement in figure 9(b). An insulating liquid is placed on a micro-stage to define the initial droplet shape. When a voltage is applied to the interdigitated electrodes, the surrounding conductive liquid squeezes the central insulating liquid inward, thus changing its shape and creating a tunable microlens. The interdigitated electrode arrangement of this design has a varying gap as a function of radius; i.e. the farther from the centre, the smaller the gap becomes. For a given droplet diameter, any lateral movement of the droplet from the centre will result in an increase of the capacitance seen from the electrical circuit, and thus an increase in energy, due
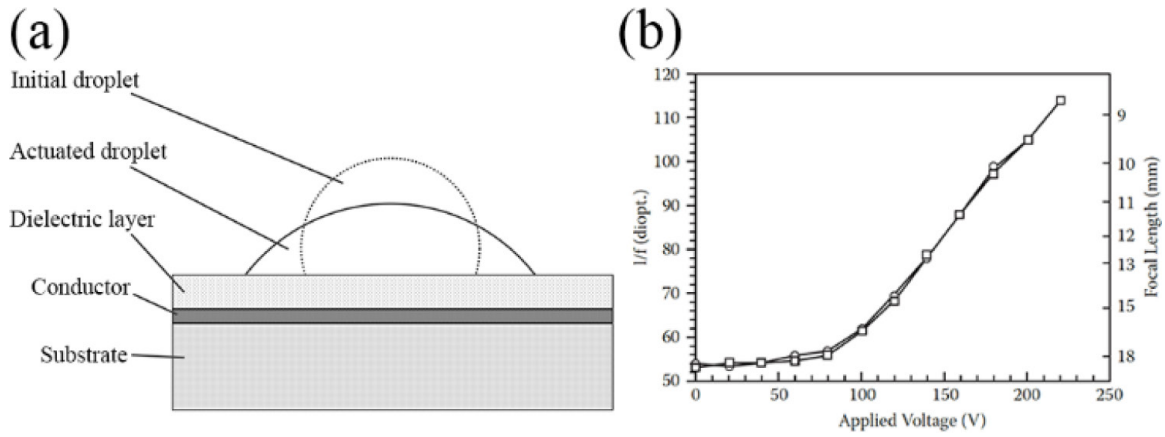
Figure 7. (a) A microlens based on EWOD. A conductive liquid is placed on top of an insulator that covers an electrode. By applying a voltage, solid/liquid surface tension is changed and as a result, the contact angle is tuned. This in turn will alter the shape (and thus the radius of curvature) of the liquid droplet placed on top of a dielectric layer, forming a tunable lens. (b) The optical power of the fabricated microlens as a function of applied voltage. Reprinted by permission from Springer Nature Customer Service Centre GmbH: Nature. [24] © 2000.
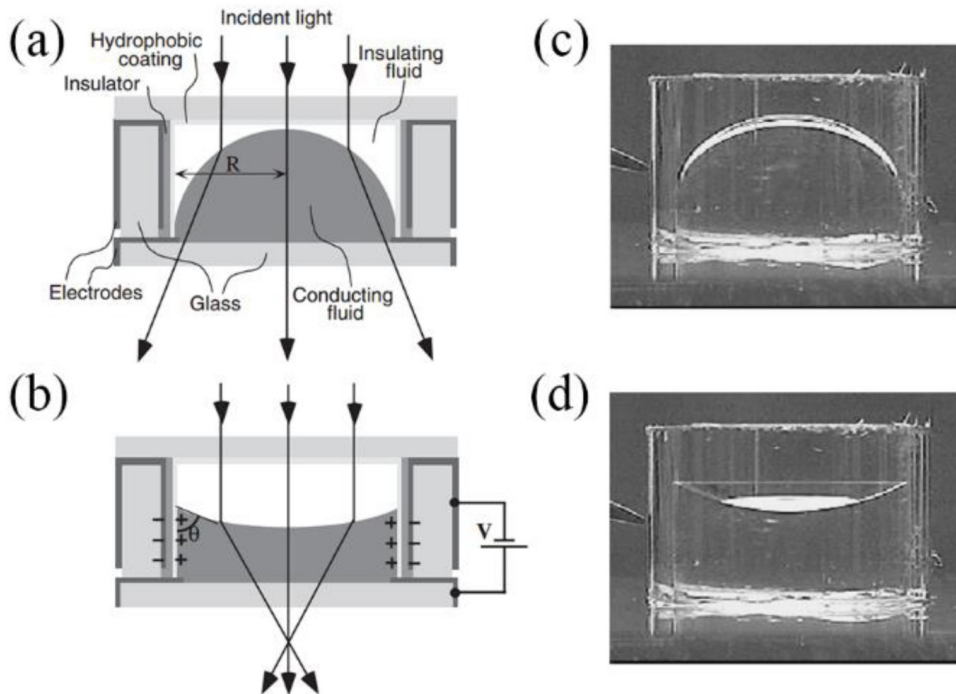
Figure 8. (a) Schematic cross section of a liquid-based variable lens in a cylindrical housing. (b) Under the application of a voltage charge accumulates in the wall electrode whereas opposite charge is induced in the conducting liquid near the solid/liquid interface. (c) Photograph of a 6 mm diameter electrowetting lens without a voltage applied and (d) with a voltage applied. [31] 2005 © Springer Nature Switzerland AG. With permission of Springer.

to abovementioned radially varying gap between electrodes. Therefore, the droplet tends to be self-centred to maintain a lower energy state.

The self-centring mechanism of the areal density modulated electrodes is shown in figures 9(c)–(e). As seen, by increasing the voltage, the insulating liquid is squeezed towards the middle and thus the liquid droplet curvature increases, while remaining at the centre of the device. The back focal length of the resulting microlens was measured and shown to vary from 10.2 mm to 5.8 mm when the voltage changed from 0 to 100 V.

DEP forces present another driving method for tuning liquid microlenses [26, 29]. In these devices, two immiscible liquids have substantially different dielectric constants. When exposed to an electrostatic field, the liquids will change their shapes to minimize the potential energy stored in the electrohydrodynamic system [29]. The DEP mechanism used to deform the droplet can be described using the Kelvin polarization volume force density f as:

$$f = -\frac{1}{2}\nabla\left[\,(\varepsilon_1 - \varepsilon_2)\,|E|^2\,\right].\qquad(6)$$

In equation (6), ε_2 and ε_1 are the permittivity of the droplet and the sealing liquid, respectively, and E denotes the intensity of the electric field.
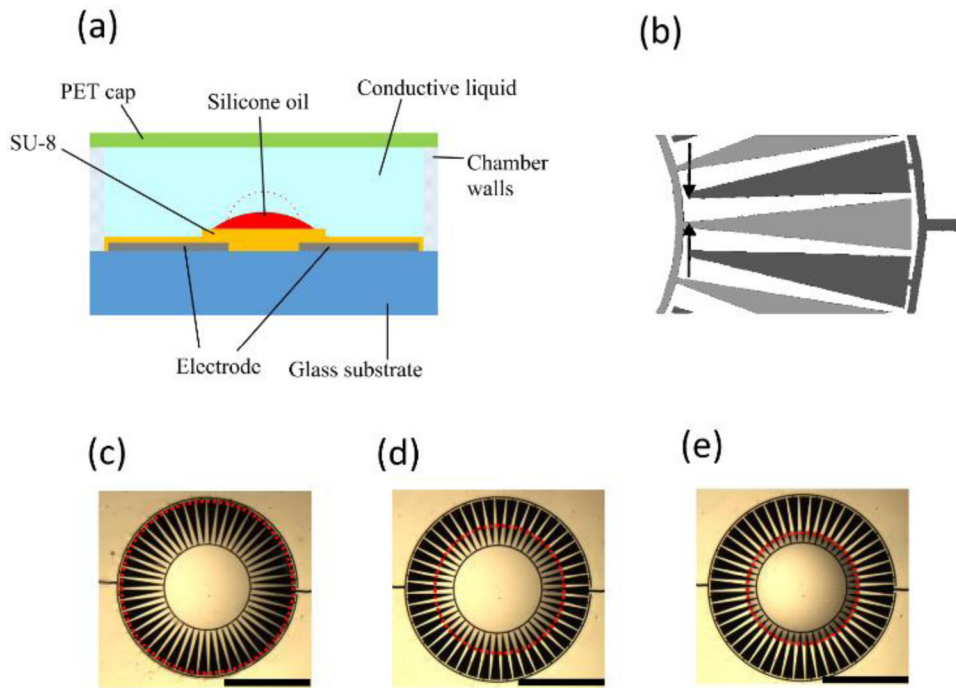
Figure 9. (a) The cross section of a liquid microlens with areal density modulated electrodes. The insulating liquid (here, silicone oil), is placed on a predefined SU-8 micro-stage. The rest of the chamber is filled with a water based conductive liquid. By applying a voltage to the electrodes, the silicone oil droplet is radially pushed inward (shown by the dotted red line), and its curvature changes, resulting in a change of the focal length of the microlens. A variable capacitance is seen from the electrodes. It consists of a water based conductive liquid as a floating electrode that moves on top of the insulated electrodes. (b) Top view of a section of electrode design. A plurality of interdigitated electrode and counter electrode pairs (shown in dark and light grey) are connected to a voltage source. The lateral gap between electrodes (highlighted by arrows) decreases as it goes farther radially. (c) Top view of the microlens at different actuation voltages. The scale bar is 1.5 mm. The dashed circle highlights the edge of the droplet. Initially at 0 V, the droplet is pinned at the edge of the micro-stage. (d) The centred droplet at 60 V. (e) The centred droplet at 100 V. Adapted from [32]. © IOP Publishing Ltd. All rights reserved.

In the configuration shown in figure 10, a plurality of annular, interdigitated rings are placed on a substrate. By applying a voltage, the high-dielectric liquid squeezes the low-dielectric liquid towards the centre. The centre droplet is usually pinned at the electrode rings; thus this design provides a centring mechanism. Compared to EWOD, this design does not need a conductive liquid, and dielectric liquids usually are more stable and have a lower vapour pressure. Furthermore, DEP microlenses do not suffer from possible bubble formation known to aqueous based EWOD microlenses [33]. However, due to the digitized nature of the electrodes, the resulting tunable focal length will be discretized and the microlens lacks a continuous tunable focal range.

3.1.5. Electroactive polymer actuators. Electroactive polymers (EAPs) are among the emerging actuators for tuning membrane-based liquid tunable microlenses. One advantage of EAPs comes from their large strains under electrical stimulation that can be an order of magnitude greater than those produced by, for instance, piezoelectric devices, while at the same time can produce forces that are higher than conventional electrostatic MEMS (Microelectromechanical system) actuators. Recently, poly(vinylidene fluoride-trifluoroethylene-chlorofluoroethylene) [P(VDF-TrFE-CFE)] and poly(vinylidene fluoridetrifluoroethylene-chlorotrifluoroethylene) [P(VDF-TrFECTFE)] polymers demonstrated
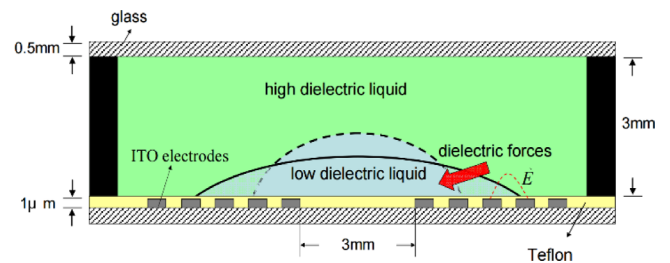
Figure 10. A cross section of a DEP microlens. The droplet shrinks to a new state (dashed line) due to the dielectric force. Reproduced from [42]. CC BY 3.0.

electrostrictive strain of more than 5% [34, 35]. Nonetheless, P(VDF-TrFE-CFE) or P(VDF-TrFECTFE) thick (greater than 20 μm) actuators require operating voltages greater than 1 kV [36], which is considered impractical for smaller electronic devices. Rather, polymer actuators consisting of multi-layered thin films of polymers sandwiched between conductors can be fabricated to possess similar a performance under much lower actuation voltage [37]. Such a tunable microlens with an EAP actuator is shown in figure 11(a). In this device, actuators are arranged at four corners of a liquid filled chamber. Fomblin perfluoropolyether (PFPE) M03 was used as the optical liquid. Its viscosity and refractive index are 54 cP at 20 °C and 1.29, respectively. The chamber is made from two silicon (Si)
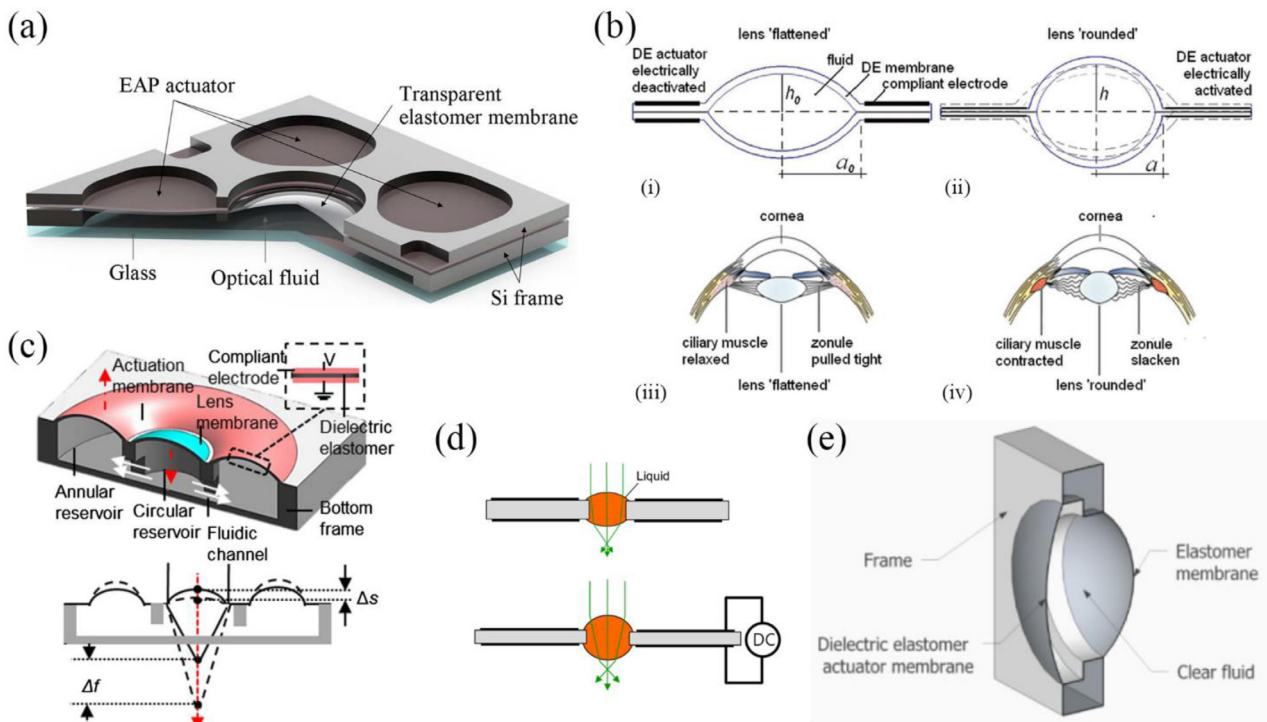
Figure 11. Tunable lenses with electroactive polymer (EAP) actuators. (a) The schematic design of a varifocal microlens suitable for wafer-scale microfabrication, utilizing an EAP. The focal length of the liquid-filled microlens varies owing to the deformation of the transparent elastomer membrane under hydraulic pressure tailored by the EAP actuator. The varifocal microlens was combined with a commercial fixed-focus five-megapixel phone camera. Reproduced with permission from [37]. © The Optical Society (OSA). (b) Analogy between the tuning mechanisms of (i) and (ii) the bioinspired tunable lens system actuated by a DE film and (iii) and (iv) the human eye system. Both systems have a flattened lens shape in (i) and (iii) the rest state and a rounded lens shape in (ii) and (iv) the activated state. The annular DE actuator functions as the combined ciliary muscle and zonular fibres. Adapted with permission from [38] John Wiley & Sons. Copyright © 2011 WILEY-VCH Verlag GmbH & Co. KGaA, Weinheim. (c) An electroactive liquid lens driven by an annular dielectric membrane, which can tune the focal length of the liquid lens by changing the fluid volume of the circular reservoir. Reproduced with permission from [40]. © The Optical Society (OSA). (d) A tunable liquid lens using a DE film with a through hole. Reproduced with permission from [41]. © (2016) COPYRIGHT Society of Photo-Optical Instrumentation Engineers (SPIE). (e) A tunable lens system using transparent DE actuators. Reproduced from [42]. CC BY 3.0.

wafers that are bonded together to create a sealed microfluidic-based liquid microlens. By applying a voltage between the parallel-plate multi-layered electrodes (not shown in here), a strain is induced that deforms these 4 membranes, bulging them inwards. This results in a liquid flow towards the centre of the device, where the liquid lens membrane with an aperture of 2.4 mm resides, thus pushing the membrane outward, altering the radius of curvature of the microlens, and induces a change in the focal length. In [37], an EAP actuator membrane showed a deflection of 9 μm under a voltage of just 40 V, while the centre membrane exhibited a movement of 37 μm, which resulted in an optical power of 50 diopters.

Carpi *et al.* demonstrated a bioinspired tunable lens made by an annular dielectric elastomer (DE) actuator functioning as the artificial muscle, as shown in figure 11(b) [38]. This tunable lens system consists of a fluid-filled elastomeric lens combined with an annular DE actuator, which is functionally analogous to the ciliary muscle and zonular fibres of the human eye. When the DE actuator is electrically activated, the annular region of the DE membranes is compressed in thickness and deformed and expanded in plane as a result of Maxwell stress. This deformation reduces the lens diameter and increases the lens thickness due to the constant volume

of the fluid filled in the lens; as a result, the DE actuation reduces the lens curvature and its focal length. In the human eye system, the crystalline lens has a flattened shape when the zonular fibres are stretched and the ciliary muscles are relaxed in the rest state. When the ciliary muscles contract, the radial tension of the zonular fibres is released, so that both the curvature and the focal length of the crystalline lens are decreased in the activated state. Therefore, the DE actuators successfully mimicked the lens actuation of the human eye system from the functional point of view. A few years afterward from the first demonstration of such a bioinspired tunable lens, Maffli *et al.* developed an improved DE actuator for an ultrafast tunable lens by using low-loss silicone elastomers [39]. This silicone-based tunable lens showed very short optical settling time (shorter than 175 μs) and good mechanical stability.

In addition to the tunable lens designs described above, a few different tunable lens systems using DE actuators have been demonstrated in recent years. Wei *et al.* developed an electroactive fluidic lens using an annular DE actuator, which can induce a deformation of the lens membrane and the tuning of the focal length by transporting the fluid between the lens part and the actuation part (figure 11(c)) [40]. The DE actuator proposed in this work eliminated the pre-straining process

and required lower voltage (less than 1 kV) for stable operation. Jin *et al.* presented a simple type of tunable liquid lens using a DE film that has a through hole (figure 11(d)) [41]. A liquid droplet was trapped in the hole of the DE film; the curvature and the resultant focal length of the liquid lens was tuned by varying the size of the hole. Unlike the other types of DE actuator-based tunable lenses, Shian *et al.* developed a tunable lens system using transparent DE actuators (figure 11(e)) [42]. In this tunable lens system, the lens curvature and the focal length can be tuned by actuating the transparent DE films that act as the lens surfaces themselves. Hence, this system can remove the separate space set aside for the actuators to adjust the lens curvature, and thus improve the system simplicity and compactness.

3.1.6. Magnetic actuators. Magnetic force is one of the most widely used actuation mechanism in various industrial applications. In microdevices, however, it is not as favored mostly due to ohmic loss. Nonetheless, when large displacements in actuations are needed, when designed properly, magnetically actuated devices may become more favorable. An example of relatively large-displacement-actuator that was used to drive a tunable microlens was presented in [43]. The device structure is shown in figure 12. Au wires are integrated into a polydimethylsiloxane (PDMS) membrane. A pair of permanent magnets (not shown) are placed to create a magnetic field that is perpendicular to the wires, and parallel to the PDMS membrane. When current passes through the wires, Lorentz force is induced on the wires, which in turn exerts a force on the deformable PDMS membrane. A deformation of 51.4 μm was reported for a 30 mA actuation current. Since the PDMS membrane encapsulates an incompressible liquid (glycerol), the liquid is moved from one side of the device to the other. In the optical part of the device, the deforming PDMS due to this liquid movement creates a curved surface with a refractive index higher than that of the air, thus acting as a tunable microlens.

3.2. Curved image sensors

More than a hundred years ago, Joseph Petzval described in his optical aberration theorem, namely Petzval field curvature, that even thin lenses would cause image planes to curve [44]. In the traditional camera systems with flat image sensors, this aberration can partially be compensated by bulky and expensive multiple-lens systems that consist both positive and negative surfaces. The natural eye (e.g. human eye) only has positive surfaces, thus producing significant field curvature, but can effectively compensate the aberration by curving its retina [45]. Studies have been conducted to explore the potentially dramatic improvements in performance with curved sensor surfaces [46–50], including improvements such as 7 $\times$ reductions in length and 37 $\times$ in weight of lenses, and significantly better modulation transfer function (MTF) and relative illumination, especially at the edges of the image field. Currently, the first practical application of the curved focal plane was achieved in Kepler photometer, in which 42
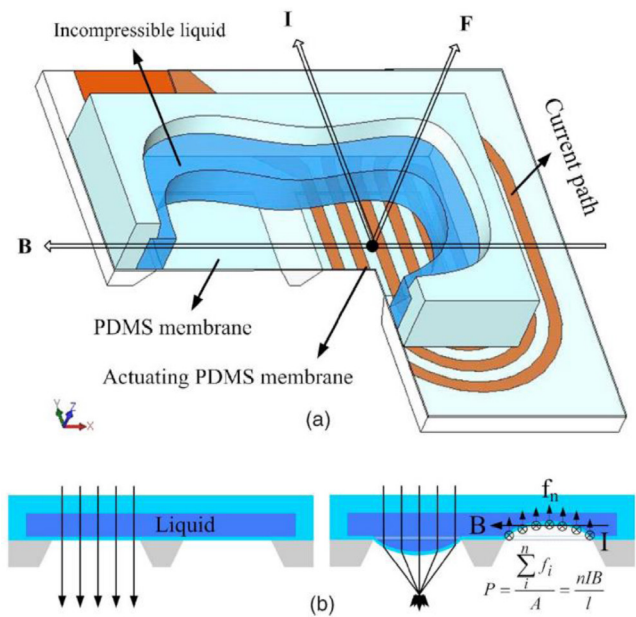
Figure 12. (a) The schematic view of a magnetically actuated microlens. (b) The working principle: forces are induced on the wires as a result of a current passing through the parallel wires. The incompressible liquid is then pushed, bulging out from the other side of PDMS membrane, forming a tunable microlens. Reprinted from [43], with the permission of AIP Publishing.

mosaics of flat charge-coupled devices (CCDs) imaging sensors were assembled on a curved substrate. Because integration of these flat CCDs onto a curved surface requires bulky components and intrinsically generates 'dead zones' between sensors, such configuration has limited applications, especially in commercial-grade imaging devices. Owning to the mainstream planar semiconductor processing technologies, fabrication of monolithic truly curved digital image sensor is still challenging. In the past decade, efforts have been made to develop novel technologies that can fabricate curved image sensors, and a few prototypes have been demonstrated. Based on the fabrication process and substrate materials, these prototypes can be generally categorized into image sensors on fixed curved surfaces and deformable curved surfaces, respectively.

The ability to transfer a flat, thin-film-based electronic and optoelectronic systems onto elastomer substrates opens up many applications in flexible electronics and wearable devices, and also provides a promising strategy to realize curved image sensors. Such a concept was demonstrated by Lee and co-workers at the University of California at Berkeley [51]. An array of Si micro-squares connected with S-shaped suspensions was fabricated on a PDMS membrane, and configured into a hemispherical shape by a pneumatic pump, as shown in figure 13(a). In their work, the S-shaped suspensions as shown in figure 13(b) were made of silicon dioxide with a thickness of 1 μm. The suspensions would provide spring constants of 7.3 N m^{-1} in the direction perpendicular to the membrane and 424 N m^{-1} along the stretching axis. In this manner, the Si micro-squares would not be broken during the stretching of the PDMS membrane. By coating a thin layer of Cr/Au, resistance of the S-shaped
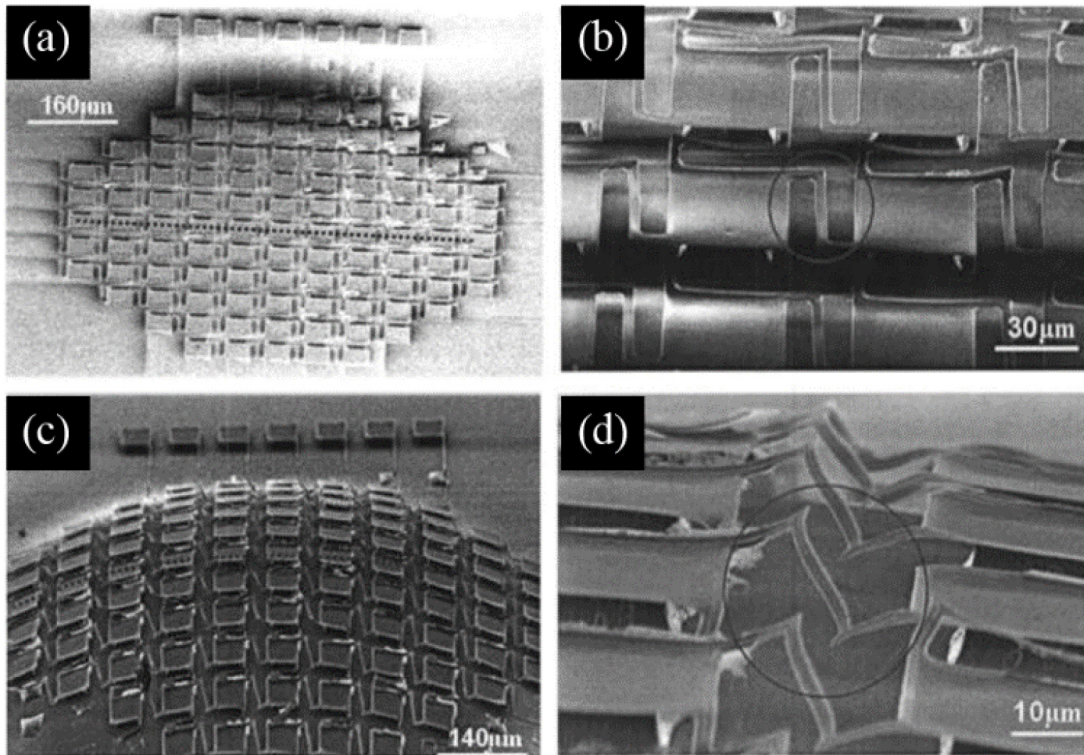
Figure 13. Scanning electron microscope (SEM) images of a fabricated array of Si micro-squares connection with S-shaped suspensions. (a) and (b) The device and S-shaped suspensions on a flat membrane. There is no pressure applied to the membrane (c) and (d). SEM images of the device and S-shaped suspensions on a hemispherical shape, which was bended by a 50 kPa of applied pressure. Reprinted from [51], with the permission of AIP Publishing.

suspensions across the PDMS membrane were measured under different pneumatic-pumping pressures, confirming electrical connections under the membrane deflection. Such design shows the feasibility to fabricate image sensors on large-curvature surfaces without breaking the metal connections between pixels.

The first functional image sensor on a curved elastomer substrate was demonstrated by Rogers *et al.* at the University of Illinois at Urbana-Champaign, as shown in figure 14 [52]. They introduced an electronic eye imager that used well-established electronic materials and planar processing approaches to create optoelectronic systems on a flat surface in unusual designs enabled to be geometrically transformed to nearly arbitrary curvilinear shapes. Figure 14(a) illustrates the fabrication process. In general, a hemispherical dome of PDMS substrate is transformed into the planar shape of a 'drumhead' by a biaxial tension produced by ten independent paddle arms. Meanwhile, conventional planar processing forms a passive matrix focal plane array on a Si-on-insulator (SOI) wafer. The focal plane array was then transferred onto the planar 'drumhead' PDMS substrate. Moving the paddle arms to their initial positions causes the elastomer to relax back, approximately, to its initial hemispherical shape but with a slightly (10% for the systems investigated) larger radius of curvature, as shown in figure 14(b). A critical design feature in this device is the use of thin, narrow lines to connect nearest-neighbor pixel elements (see figure 14(c)), which enables elastic compressibility in the system. Figure 14(d) demonstrates the electronic eye camera by integrating the curved focal plane with a lens.

Grayscale images were successfully captured by this prototype with 16-by-16 pixels, as shown in figure 14(e). Because adjacent pixels in the camera eye need to be connected through soft 'bridges' so that the focal plane can be wrapped onto a hemispherical surface, the density of pixels would be lower than the conventional flat image sensors. To obtain images with fine spatial features, rapid scanning of the whole image plane by eccentrically rotating the camera eye was needed to reconstruct the final image with higher resolution.

After realizing their first camera eye with functional curved image sensor, Rogers and co-workers made further improvement of the camera systems. For example, to overcome the limitation induced by the fixed detector curvature that could be incompatible with changes in the Petzval surface of the variable zoom lenses, a dynamically tunable electronic camera eye was developed based on a curved focal plane with adjustable curvature [53]. In addition, hexagonal arrangement of the pixels was also demonstrated, which could improve the density of the pixels as well as the coverage area [54]. Several other research groups have also been studying on the fabrication of optoelectronics on deformable polymer substrates for curved image sensors. However, all these works are at the proof-of-concept stage and far from commercial maturity. Furthermore, these approaches share some limitations, including low pixel density due to the substrate stretching, incompatibility with sophisticated active pixel complementary metal–oxide–semiconductor (CMOS) or CCD arrays, and the inability to scale to small pixel pitches (e.g. <10 μm) due to the processing limitations.
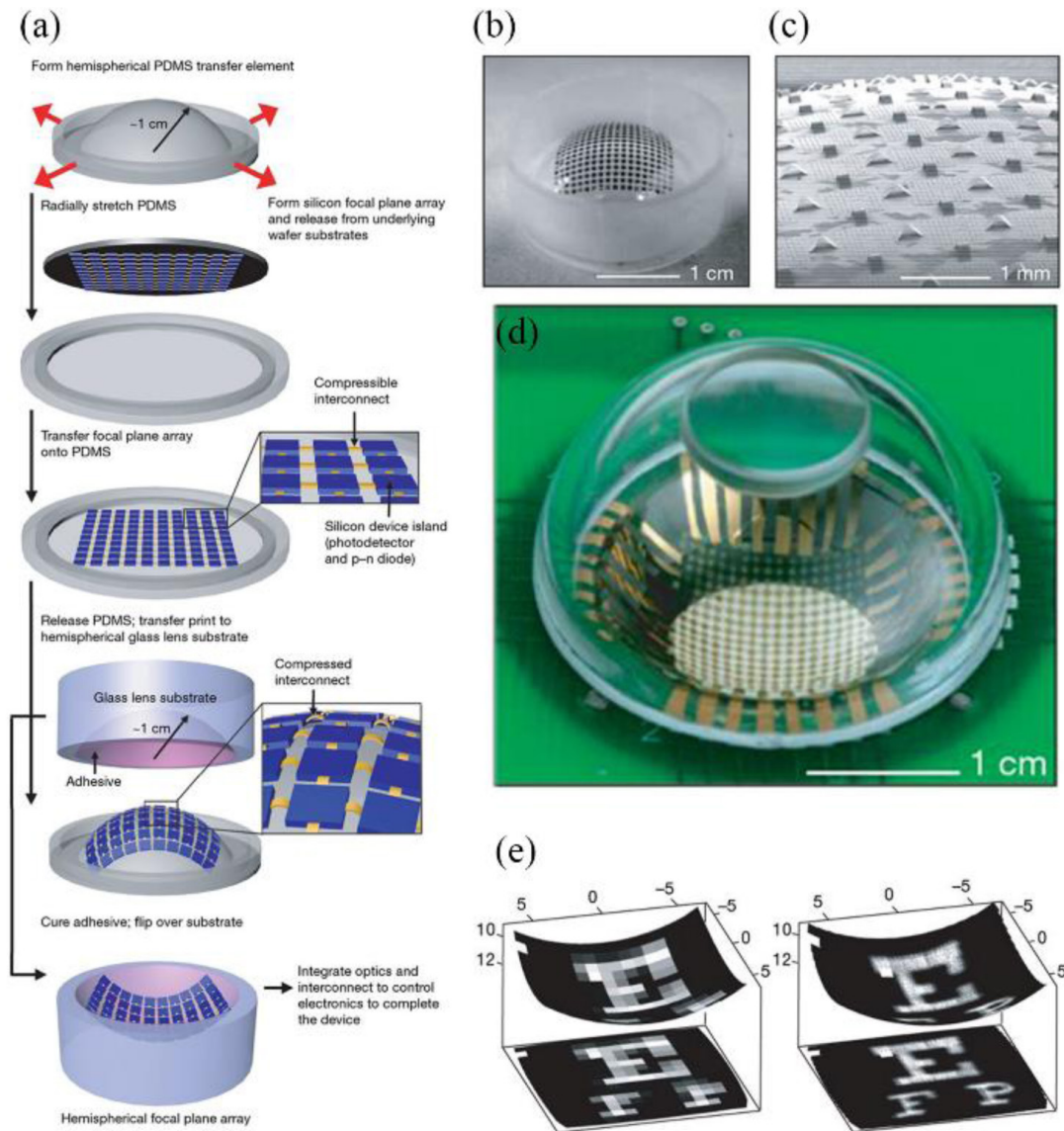
Figure 14. (a) Schematic illustration of the fabrication process of the electronic camera eye. (b) Photograph of a hemispherical PDMS transfer element with a compressible focal plane array on its surface. (c) An SEM image of a portion of the array in (b), illustrating the compressible interconnects. (d) Photograph of a hemispherical electronic eye camera. (e) The output images of the electronic eye camera. The images on the left and right were acquired without and with scanning strategy, respectively. Adapted with permission from Springer Nature Customer Service Centre GmbH: Nature. [52] © 2008.

In order to improve the pixel density of the curved imaging sensors, research has been focusing on fabricating the sensor array directly on Si substrates. Jin *et al.* at University of Illinois shown their early attempt on fabricating an array of α-Si: H photoconductive sensors on a spherical glass substrate by a soft-lithography patterning process followed by a deposition of α-Si and metal thin structures [55]. Because such fabrication process is not well compatible with the standard semiconductor manufacturing techniques, and the deposited Si layer has much lower performance in photoconductivity, to date no results of this approach are reported to produce a working imaging sensors. An alternative approach to the curved imaging sensors on Si substrates is the fabrication of the sensor array on a flat Si by the standard semiconductor manufacturing techniques, and then bended it into curved shapes. It has been proven that by thinning the Si to tens of

micrometres, bending it to a relatively small curvature could be achieved. However, due to the mechanical properties of the material, a principal trade-off between the fundamental questions, (1) can required curvature be demonstrated on large-size imaging sensors and (2) how well the sensors perform electro-optically after the bending, always exists and become the most interesting topic in this research field.

Dinyari *et al.* [56] and Rim *et al.* [46] introduced a spring structure between the individual pixel islands, increasing the flexibility during the bending. A curved Si structure (with size $1 \times 1\,cm^2$ and curvature radius of 1 cm) was fabricated based on such design, as shown in figure 15. Fabrication of such curved Si die requires expensive SOI substrates. To further decrease the cost of fabrication, mechanical and chemical thinning process was utilized to produce thin Si structures from regular Si wafers. In addition, pressures were applied
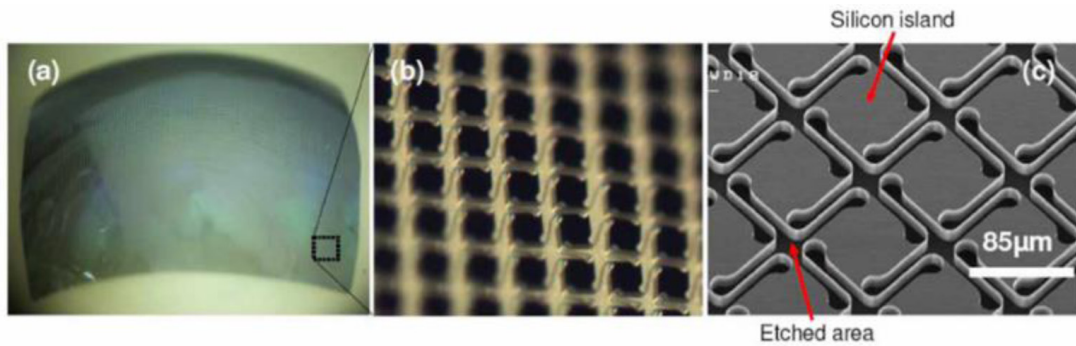
Figure 15. (a) Photo of a fabricated curved Si die. (b) Details of the curved die at an off-axis location, showing the spring structures between the pixel islands. (c) SEM image of the pixel islands and the spring structures. Reproduced from [46]. CC BY 3.0.

to bend the thin Si into curved structure without introducing complicated and fragile spring structures. For example, Olaf Iwert [57] and co-workers at University of Arizona and European Southern Observatory (ESO) demonstrated a bending process by the negative vacuum pressure. Both working convex and concave frontside-illuminated imaging sensors with size of $6 \times 6 \, cm^2$ and curvature radius of 50 cm were demonstrated, as shown in figures 16(a) and (b). Dumas *et al.* [58] demonstrated a bending process by a mechanical pressure, and a $10 \times 10 \, mm^2$ CCD with curvature radius of 40 mm was fabricated. The CCD sensor was integrated in a camera, and an image in near-infrared (NIR) spectrum was obtained.

Although these bending process shown possibility to produce working curved imaging sensors, the curvature of the sensor is limited and the yield is still low due to the damages of the thin Si induced by the pressures. As described in Olaf Iwert's work, the fabrication process needs to be strictly controlled and the material has to be carefully selected to avoid the cracking or damage of the device during the bending process [57]. To address these problems, researchers at Microsoft [59] improved the bending process, and demonstrated a working curved CMOS imager with curvature of 26.7° as shown in figure 17(a), comparing to <20° curvatures of previous works. As demonstrated in figure 17(b), in the conventional bending process to produce curved imaging sensors, the edges of the thinned Si membranes (red line) were fixed while pressure or vacuum is applied, and the deformation is resisted by radial in-plane tensile loads that grow nonlinearly with increasing deflection. By comparison, the improved approach forms an unconstrained die through pressurized flexible membrane (blue line) that leaves the edges free to translate, thus largely eliminating radial tensile forces and reducing the strain energy density.

Although there exists various unsolved problems such as low yield and limited bending curvatures, deformation of a thinned Si membrane with pixel array into the curved shapes has been proven to be the most promising technology to fabricate commercialization viable curved imaging sensors. In 2014, Sony has released their first prototype of the curved imaging sensor fabricated by this method, and demonstrated a significant improvement of the imaging performance compared to the flat sensors [60]. Compared to the other approaches to the curved sensors, the wafer thinning and bending process can be completely integrated into the
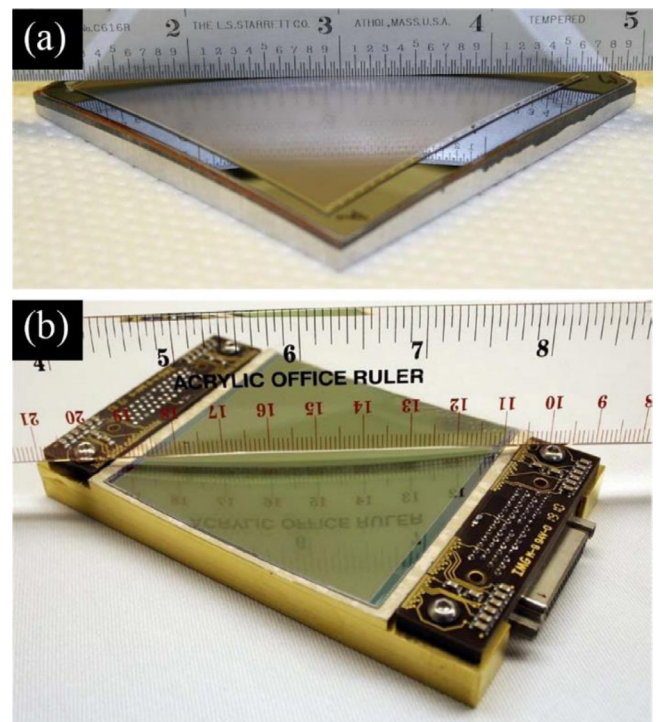

Figure 16. Photos of convex (a) and concave (b) imaging sensors. Reproduced with permission from [57]. © (2012) COPYRIGHT Society of Photo-Optical Instrumentation Engineers (SPIE).

existing semiconductor processing, and thus largely reduce the cost of manufacturing and duration of the R&D circle. In addition, this approach demonstrated the capability of fabricating 100% fill-factor imaging sensors with comparable electro-optical properties. As for transferring the sensor array onto flexible polymer substrates, the research will focus on those low-resolution imaging applications that requires tunable field-of-view.

3.3. Tunable irises

Tunable irises of mammal eyes can control the amount of light passing through the lenses by varying the size of the iris opening depending on the ambient light intensity. This simple and effective mechanism has been used to develop artificial irises. Several different types of tunable liquid irises have been developed to be utilized in micro-optical systems [61–64].
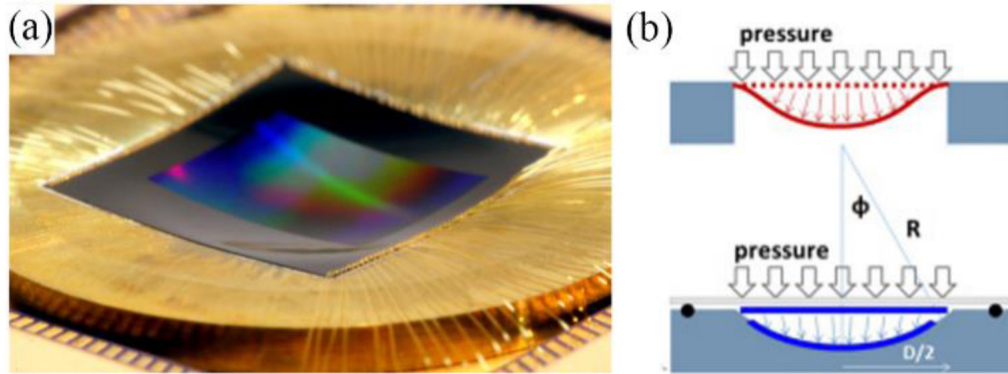
Figure 17. (a) Photo of a highly curved imaging sensor. The curvature of the shown sensor is 26.7°. (b) Comparison between the conventional (upper image) and the improved bending process (lower image). In the improved bending process, the edges of the Si membrane (blue line) are free to translate. Reproduced from [59]. CC BY 3.0.

The tunable liquid irises were utilized for not only modulating light intensity but also adjusting the f-number and depth of field, preventing scattering light, and reducing spherical aberration. In addition to liquid irises, wearable or implantable artificial irises have been demonstrated, which can self-adaptively control the amount of light through the irises by sensing or reacting to the ambient light intensity. These self-adaptive artificial irises could be helpful to patients of aniridia, albinism, iris coloboma, and trauma-induced iris defect [65–67].

3.3.1. Tunable liquid irises. Müller *et al.* proposed a tunable liquid iris that used microfluidic structures and capillary force [61]. The optofluidic device was constructed by photolithographically defined multilevel resist structures, fluid ports drilled utilizing an ultraviolet (UV) laser, and injection of an opaque liquid that controlled the aperture diameter and light transmittance. Since the capillary pressure depended on the height of the chamber, the meniscus was pinned at each step of the chamber. Thus, the opaque liquid was filled at the outer ring first and subsequently moved inward towards the centre of the chamber (figure 18(a)). The research group compared the optical performance of a mechanical diaphragm and the optofluidic iris by capturing images with different *f*-numbers of the system. The optofluidic iris successfully tuned the *f*-number and provided comparable imaging quality at high *f*-number but reduced contrast at low *f*-number.

In addition to the optofluidic iris using microfluidic structures and capillary pressure, other approaches have been demonstrated for tunable liquid irises that used dielectrophoresis [62], electrowetting [63], and electromagnetic [64] effects, which can manipulate the opaque liquid filled in fluidic channels. As a result, the devices could tune the aperture diameter.

3.3.2. Liquid crystal rings. Polymer-dispersed liquid crystals (PDLCs) were used to develop an artificial iris [65], which consisted of eight PDLC rings that can change its states from opaque to transparent by applying a bias voltage (figure 18(b)). The reason of using PDLC in this work is its higher light transmittance (as high as 70%) compared to the aligned pure LCs whose transmittance is limited to 50% due to the necessity of a polarizer. The PDLC rings controlled the intensity of

transmitted light depending on the ambient light intensity by using an integrated control circuit with a photodiode. When the artificial iris was tested under ambient light intensities from 0 lux to 2500 lux, it could effectively modulate the light intensity. The maximum value of the modulated light intensity was 720.5 lux at the ambient light intensity of 1375 lux. This artificial iris can potentially be utilized for robotic vision.

3.3.3. Photo-reactive materials. Artificial irises with self-regulating light transmission were developed by using photo-reactive materials [66, 67]. Na *et al.* demonstrated an artificial iris that had spoke patterns mimicking the iris frill of a human eye and could control the light transmission by spiropyran dyes embedded in a transparent polymer (figure 18(c)). Although the dynamic response of the artificial iris was relatively slow (tens of seconds) compared with the human iris (on the order of ms), the artificial iris effectively attenuated the light transmission as the intensity of incident light increased. Thanks to the resemblance to the human iris and self-regulating characteristics, this proposed device has a potential to be used in contact lenses or as implantable artificial irises.

4. Bioinspired compound eyes

4.1. Artificial compound eyes on planar substrates

A number of artificial compound eyes (ACEs) have been developed and fabricated on planar substrates owing to the readily available fabrication processes and ease of integration with conventional image sensors. The optical designs are relatively straightforward to develop camera modules by integrating these ACEs with the image sensors. Although wide FoV is not achieved due to the flatness of the devices, the ACEs can provide sufficiently thin imaging systems.
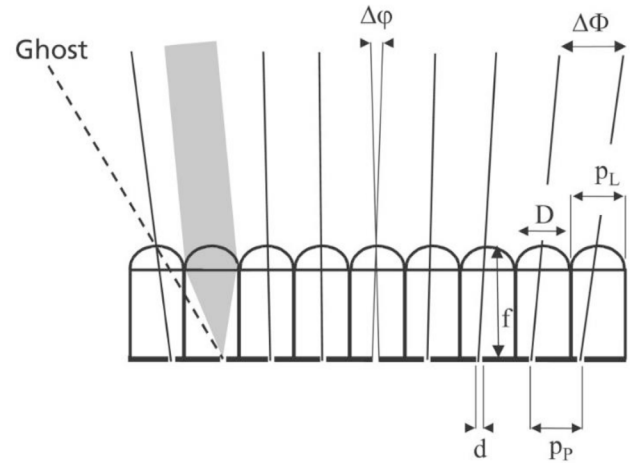
4.1.1. Artificial apposition compound eyes. Duparré *et al.* developed artificial apposition compound eyes on planar substrates that can be easily integrated with conventional image sensors [68, 69]. The optical device consists of a microlens array (MLA) on a glass substrate and a pinhole array at the bottom of the substrate (figure 19). Each microlens generates
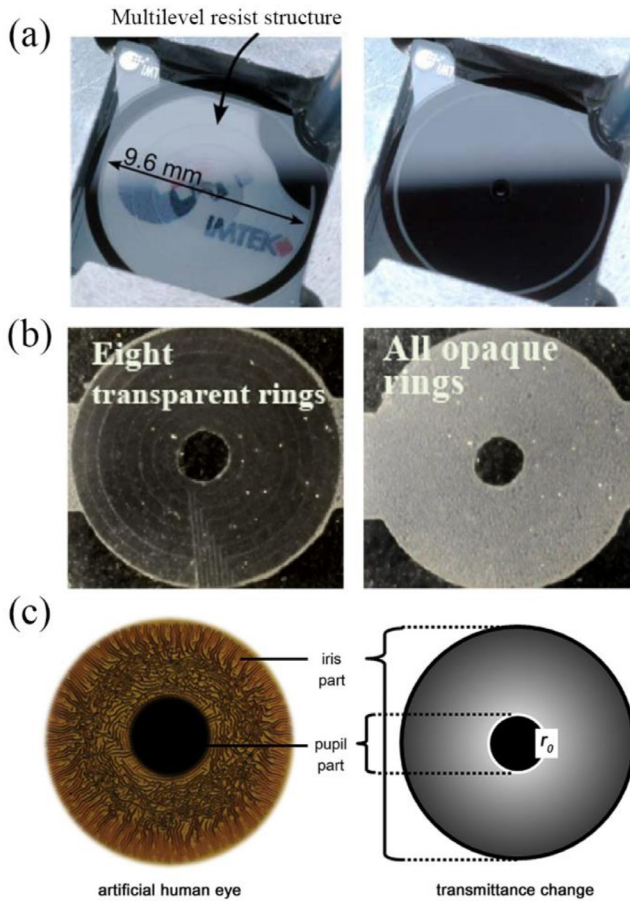
Figure 18. Artificial irises. (a) Optical images of a tunable liquid iris with microfluidic structures. The tunable liquid iris is optically opened and closed through liquid actuation (bottom). © 2010 IEEE. Adapted with permission, from [61]. (b) Optical images of the artificial iris with all opaque (left) and all transparent (right) PDLC rings. Adapted from [65], Copyright (2011), with permission from Elsevier. (c) An illustration of an artificial eye composed of a pupil part and an iris part that resemble the iris frills of the human eye (left). A schematic of the artificial eye (right). In contrast with the human iris, the artificial iris controls the light transmittance by using a reversible photoreactive material without change in the pupil size. Reprinted from [67], Copyright (2013), with permission from Elsevier.

Figure 19. Principle of an artificial apposition compound eye on a planar substrate. A planar artificial compound eye consists of an MLA with a diameter D, a focal length f, and a pitch P_L on the front side of a spacing structure, and a pinhole array with pinhole diameters d and a pitch P_P on the focal plane of the microlenses. The channel directions of view are pointing outward because of the difference in pitch, $P_L - P_P$, of the microlens and pinhole arrays, which results in an interommatidial angle $\Delta\Phi$. The acceptance angle $\Delta\varphi$ of a channel is determined by the ratio of the pinhole diameter d and the focal length f, and diffraction effects of the microlenses are determined by λ/D, where λ is the wavelength of light. Optical isolation between adjacent channels must be implemented to prevent crosstalk and ghost images. Reproduced with permission from [69]. © The Optical Society (OSA).

a small subimage of the object. The imaging system obtained a magnified Moiré image by adjusting the difference in pitch between the MLA and the pinhole array, $\Delta P = P_L - P_P$. The difference in pitch determines the viewing directions of each optical channel. If the pitch of the pinhole array is smaller than that of the MLA, the optical axes of the channels are directed outward. Accordingly, an upright Moiré image results. If the pitch of the pinhole array is larger than that of the MLA, the image is inverted. The difference in pitch also affects the interommatidial angle of the artificial apposition compound eye, $\Delta\Phi = \tan^{-1}(\Delta P/f)$, and the Moiré magnification, $P_P/\Delta P$. The overall image size of the device is determined by the Moiré magnification, hence the thickness of the device is completely independent of the image size. This arrangement delivers a much thinner device than a classical objective lens with the same magnification. The acceptance angle $\Delta\varphi$ is one of the key parameters of the device for determination of resolution and sensitivity. The trade-off lies in that it has to be small for high resolution and large for high sensitivity.

The artificial apposition compound eyes were fabricated by wafer-scale lithography processes. Two different types of artificial apposition compound eyes were demonstrated, depending on whether the device had opaque walls or not. The device without opaque walls used a thin 4-inch glass wafer as a spacing structure between MLAs and pinhole arrays. The master patterns for the MLAs were fabricated on a Si wafer using photolithography with reflow process. The MLAs were replicated by moulding into UV curable polymer on the front side of the glass wafer. The pinhole arrays were constructed on the backside of the glass wafer by patterning a thin metal film. The wafers were diced and directly mounted onto the detector array to capture images. However, this device cannot avoid the crosstalk between adjacent channels. To avoid ghost images from crosstalk, opaque walls were added between channels. The device with opaque walls used an SU-8 photopolymer and a highly absorbing polymer as a spacer. High-aspect-ratio SU-8 columns were fabricated to make transparent channels, and gaps between SU-8 columns were filled with a highly absorptive polymer to form the opaque walls. Microlens and pinhole arrays were formed by the same fabrication procedures. Since the spacing structure was formed on the thick supporting substrate, the device with opaque walls cannot be directly mounted onto the detector array device. For characterization, the captured images of the device with opaque walls were relayed onto a CCD camera.

Radial star and line patterns were imaged to measure the optical performance of the artificial apposition compound eye. The achieved resolution of the device was 1.5 line pairs per degree (LP/°) with 2 μm pinholes. The opaque walls effectively eliminated ghost images that were caused by cross talk.

After the demonstration of this artificial apposition compound eye, the same research group developed another artificial compound eye inspired by neural superposition eye of insects to resolve a problem of the artificial apposition compound eye, which is the intrinsic trade-off between resolution and sensitivity, as previously pointed out [70]. If other parameters are fixed, the sensitivity of the device is increased along with an increasing pinhole size, which decreases the resolution of the device. Unlike in the previous artificial apposition compound eye, the solution was using a multi-channel imaging system and redundant sampling to increase the sensitivity without sacrificing the resolution. This artificial neural superposition eye also suppressed temporal noise and provided color image by adding a color filter in each channel.

As natural compound eyes, the planar type of artificial apposition compound eyes employs spherically shaped microlenses, which is not an optimized design to achieve wide FoV. To solve this problem, Li *et al.* designed and fabricated a freeform MLA that can be directly mounted to a commercial image sensor [71]. They fabricated the freeform MLA using diamond broaching to first make a metal mould and microinjection moulding to produce lenses at a low cost. The freeform MLA has an FoV of 48° × 48°. To minimize crosstalk among adjacent channels, a micro aperture array was added between the freeform MLA and an image sensor. The measured result showed that the freeform MLA was able to form the images and to provide wide FoV as expected by the design.

4.1.2. Artificial superposition compound eyes. Superposition compound eyes have better sensitivity than apposition compound eyes because the effective pupil size is larger than the size of a single channel. This is the reason why most nocturnal insects and marine crustaceans that live in dim environments possess superposition compound eyes, whereas diurnal insects have the apposition compound eyes. Furthermore, the resolution of the superposition eye type can be almost as good as the diffraction limit allows. Therefore, this eye type can solve a problem of the apposition eye type, which is the trade-off between resolution and sensitivity. However, the superposition compound eyes need a clear zone, which requires a longer optical system.

In 1940, Dennis Gabor described an optical system that could be seen as an artificial counterpart of the superposition compound eyes, known as 'Gabor Superlens' [72]. After this invention, Hembd-Sölner *et al.* reported the first experimental demonstration of Gabor Superlens [73]. The manufactured superlenses succeeded to confirm Gabor's theoretical analysis, but it had relatively high system thickness due to the long focal length. Stollberg *et al.* significantly reduced the size of the Gabor Superlens and improved its optical performance such as FoV and resolution by micro-optics technology [74].

The miniaturized Gabor Superlens consists of two separate components that have three MLAs and four aperture layers
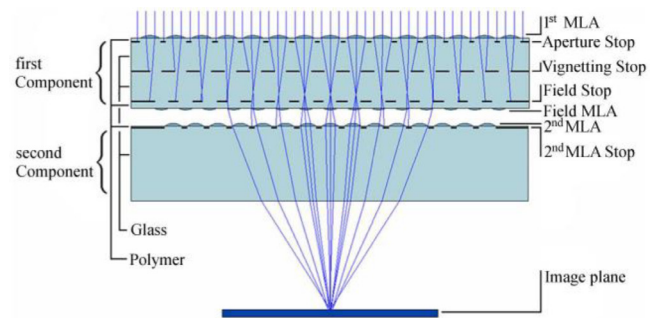

Figure 20. Schematic diagram of an optimized Gabor Superlens and ray-tracing at zero-degree incident angle. The optimized Gabor Superlens consists of two separate components that have three microlens arrays and four aperture layers. Reproduced from [74]. CC BY 3.0.

(figure 20). Unlike the Gabor Superlens that has two MLAs, one more MLA, the field MLA, is added between the first and second MLAs to reduce vignetting and increase FoV and contrast of the image by reducing the stray light from adjacent channels. Four aperture layers also suppress the inter-channel crosstalk and ghost images. The aperture stop limits the cone of light and the vignetting stop further controls the crosstalk between adjacent channels. The light sensitivity of the superlens is determined by the field stop because it controls the amount of channels contributing to an image point. The second MLA stop blocks the light that passes through the gaps between the microlenses of the second MLA.

The diameter of the field stop is related to the resolution and sensitivity of the Gabor Superlens. The larger diameter of the field-stop ensures that more channels can focus light onto a single image point, hence higher sensitivity of the optical system. In contrast, since more contributing channels gather light from outer channels that bring forth aberrated rays, the size of the focused spot increases and the resolution decreases.

The two components of the Gabor Superlens were carefully aligned (accuracy better than 1 μm with active alignment) in front of a CCD sensor to measure the optical performance. The optical performance of the fabricated Gabor Superlens matched well with simulated results. The fabricated Gabor Superlens had larger effective pupil diameter (864 ± 38 μm) and higher resolution (2.0 LP/°) than previous artificial apposition compound eyes. On the contrary, the Gabor superlens was thicker than the artificial apposition compound eye due to its higher number of components and complexity.

4.1.3. Cluster eyes. A research group at the Fraunhofer Institute developed several thin imaging systems inspired by natural compound eyes. However, both artificial apposition and superposition compound eyes have a low image resolution. To overcome this issue, the same group found a solution from the compound eye of Xenos Peckii, a wasp parasite. Unlike the apposition compound eye that has one photoreceptor corresponding to each lens, Xenos Peckii has more than one hundred photoreceptor cells on the retina of each eyelet, which detects a partial image within the overall FoV, and the partial images are then combined to form a high-resolution image (figure 21(a)). Brückner *et al.* developed a microoptical
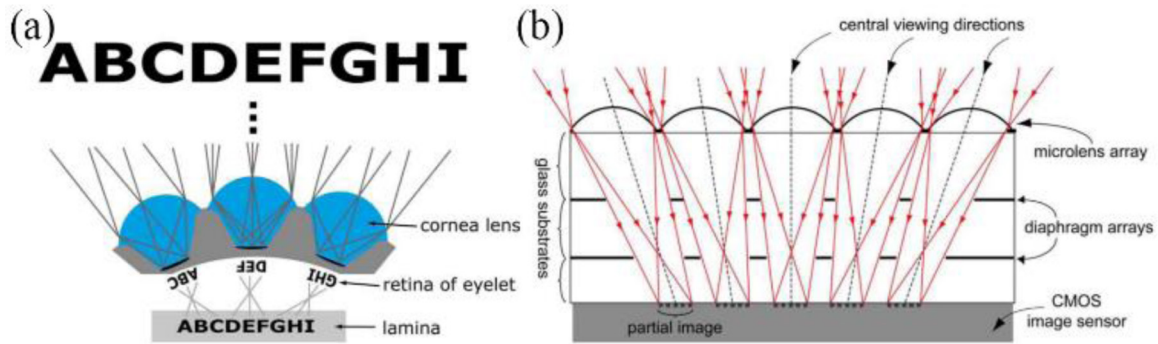
Figure 21. Schematic diagrams of the compound eye of Xenos Peckii and the electronic cluster eye (eCley). (a) Each separate eyelet detects different part of the object space and the partial images are combined to form a real image of the object space in the lamina. (b) Each microlens in an eCley forms a partial image on the attached CMOS image sensor and multiple diaphragm arrays prevent crosstalk among the adjacent channels. The partial images are stitched by image processing to achieve a high-resolution image. Reproduced from [75]. CC BY 3.0.

imaging device called an electronic cluster eye (eCley), which consists of a MLA and several diaphragm arrays and is directly mounted on an image sensor (figure 21(b)) [75]. Thanks to the small lens sags of the eCley, the MLA were fabricated by wafer-level technologies such as photolithography, thermal photoresist reflow, and UV moulding. Three horizontal diaphragm arrays were placed under the MLA to minimize optical crosstalk among adjacent channels. In each optical channel, the eCley captured different part of the whole FoV. Subsequently, these partial images were stitched together digitally to form a high-resolution image of the full FoV and close to VGA resolution (700×550 pixels) could be achieved with a 1.4 mm device thickness, which is about half of that of a comparable single-lens imaging system. The distortion of each partial image was corrected by image processing; thus, the final image could be reconstructed with minimal distortion.

A freeform MLA design was suggested to improve the spatial resolution of the eCley imaging system [76–78]. In order to overcome the limitation of the fabrication method utilizing photoresist-reflow-based microlens, Dunkel *et al.* developed a new fabrication method to fabricate freeform MLAs by using the combination of diamond machining and a step-and-repeat micro imprint process [77, 78]. The optical module consists of two freeform MLAs and three aperture layers containing 15×9 channels. To avoid crosstalk among adjacent imaging channels, three layers of apertures were fabricated by bonding two glass wafers with lithographically structured apertures. The eCley imaging system achieved a high-resolution image in the 720p format (1280×720 pixels) after a stitching process.

The Fraunhofer Institute research group also developed a different type of a cluster eye called an optical cluster eye (oCLEY), which consists of multiple MLAs and aperture arrays [79, 80]. The oCLEY can achieve a high resolution image by combining partial images, the same as the eCley. Since the optics of the oCLEY can optically stitch all partial images and reconstruct a final image at the image sensor without any overlap of the partial images, the oCLEY does not require a post-processing for stitching the partial images to achieve a final image, in contrast with the eCley.

In addition to the cluster eyes developed by the Fraunhofer Institute research group, a group at the Korea Advanced Institute of Science and Technology (KAIST) recently reported an ultrathin digital camera inspired by the Xenos Peckii eye [81]. The ultrathin digital camera has a microprism array to achieve wide FoV by refracting light from a large viewing angle, a light absorbing structure and apertures to prevent optical crosstalk between adjacent channels, and a MLA to focus light onto the CMOS image sensor (figure 22(a)). Featured components of this ultrathin digital camera are the concave microprism array and the light absorbing structure, compared with previous devices (figures 22(b) and (c)). These are the key components for the realization of wide FoV and high spatial resolution. The concave microprism array was fabricated by a ball lens imprinting process to define the curved shape and backside lithography that can reduce alignment error between the microprism array and the aperture. The light absorbing structure was fabricated through capillary filling of black SU-8. Thanks to the microprism array, the total FoV of the ultrathin digital camera is 68 degrees with a device thickness of 1.4 mm.

For higher resolution, the images captured from the microprism array were reconstructed utilizing a super-resolution approach. The measured MTF50 was 154 cycles/mm for the single channel and 181 cycles/mm for the reconstructed image. The MTF50 was not improved much by the reconstruction process. However, the MTF values in high the spatial frequency of the reconstructed image were significantly increased compared to the single channel image, meaning that the reconstruction process improved the edge sharpness of the image.

4.1.4. Thin observation module by bound optics (TOMBO). In 2001, Tanida *et al.* first demonstrated a compact image system called thin observation module by bound optics (TOMBO) [82]. The architecture of the TOMBO system is relatively simple compared with the other planar ACEs. Multiple identical optical units formed the TOMBO system and each optical unit consisted of a microlens, a separation structure, and a photodetector (figure 23). A low resolution image was acquired from each optical unit first, and then a high resolution image
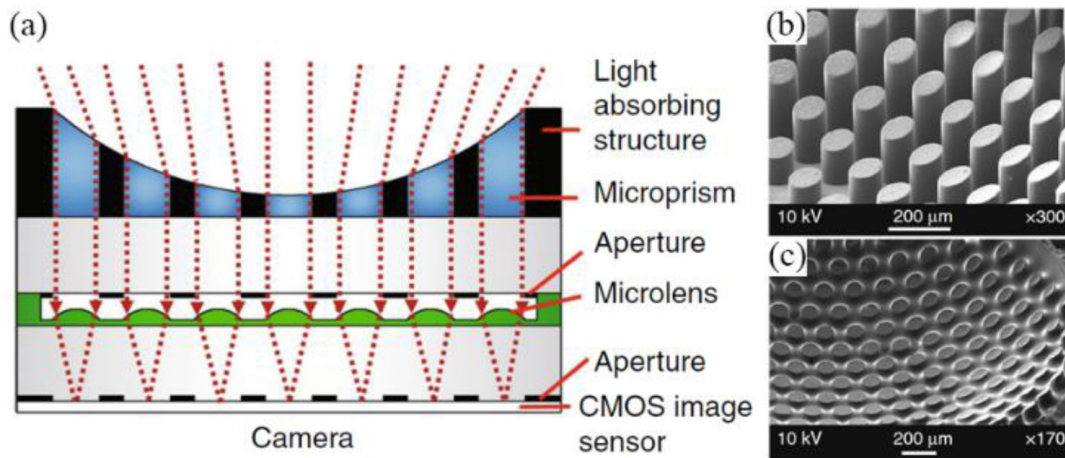
Figure 22. An ultrathin digital camera inspired by a Xenos Peckii eye. (a) Schematic diagram and optical path of an ultrathin digital camera that consists of a light-absorbing polymer, concave microprisms, microlenses, aperture layers, and an image sensor. SEM images of the concave microprism array (b) before and (c) after filling with the light-absorbing polymer. Reproduced from [81]. CC BY 3.0.

was reconstructed by image sampling and a backprojection method. Unlike the approaches taken for the other ACEs, the researchers of the TOMBO system especially focused on developing various reconstruction process. Kitamura *et al.* improved the image resolution by developing a pixel rearrangement method [83]. Nitta *et al.* further developed another image reconstruction process called iterative backprojection and combined it with the pixel rearrangement method to improve the image resolution and signal to noise ratio [84].

4.1.5. Planar emulation of compound eyes. Most of the planar type ACEs were developed to achieve high resolution optical images in a small form factor. Keum *et al.* developed a new method that emulates the cross-sectional anatomical structures of the natural compound eyes on a 2D plane [85]. This method can be utilized to better understand the visual principles of natural compound eyes and help with the design of ACEs. Fluorescent dye (Rhodamine 6G) doped photoresist (SU-8) was used for the visualization of the light propagation inside the emulated compound eyes and the measurement of the angular sensitivities. Since the anatomical structures were fabricated via photolithography, this method can easily emulate ten different types of natural compound eyes by changing the design of the masks. In this work, the researchers emulated two representative compound eye types, i.e. a simple apposition type and a reflecting superposition one, among ten different types of natural compound eyes.

The emulated compound eyes fabricated with Rhodamine 6G doped photoresist clearly showed light propagation inside the individual ommatidium (figure 24). Both emulated simple apposition eye and reflecting superposition eye showed light propagation comparable with that of natural compound eyes. In the case of the emulated simple apposition eye, only a few of the ommatidia allowed the light to propagate through the waveguides, when the direction of the illuminated light is within an accepted angle. The intensity of the off-axis light was significantly decreased due to the multiple reflection on the sidewall of the conical structure. In the case of the
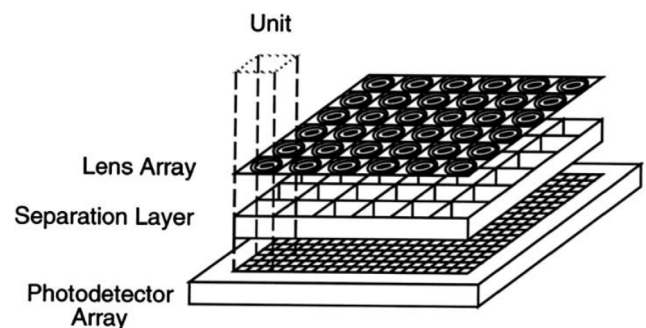
Figure 23. The architecture of the TOMBO system that consists of a microlens array, a separation layer, and a photodetector array. Each sub-optical unit provides a low resolution image, and an image reconstruction process combines the low resolution images and reconstructs a high resolution one. Reproduced with permission from [82]. © The Optical Society (OSA).

emulated reflecting superposition eye, illuminated light was internally reflected inside of the conical structures and superposed at the end of the clear zone. The direction of reflected light in the clear zone can be determined depending on odd or even number of reflections. The incident light with odd number of reflections was focused on one single spot while the light with even number of reflections directed away from the focus.

To measure the angular sensitivity function (ASF) that determines the angular resolution of the compound eyes, the researchers used fluorescence photodetector arrays (FPDA) fabricated with Rhodamine 6G doped photoresist. The FPDA were embedded at the ends of the waveguides for the simple apposition type or in the clear zone for the reflecting superposition type for the detection of the directional light through the microlenses. The measured ASFs for the simple apposition type and the reflecting superposition type showed a uniform acceptance angle of 3.0 ± 0.2 degrees and 3.1 ± 0.2 degrees, respectively. The results successfully demonstrated that both emulated compound eyes have comparable acceptance angle with those of natural compound eyes.
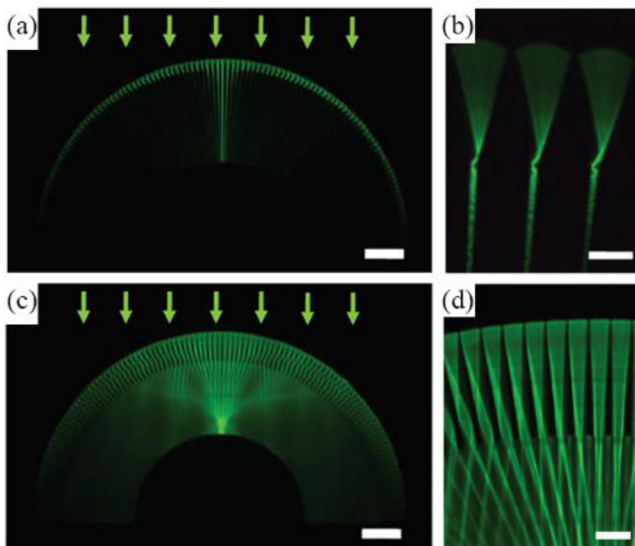
Figure 24. Visualization of light propagation through emulated compound eyes on a 2D plane. (a) Light propagation through an emulated simple apposition eye. (b) An enlarged view of the microlenses and waveguides. The amount of coupled light into the waveguides of the ommatidium depends on the angle between the incident direction of the illuminated light and the orientation of the ommatidium. (c) Light propagation through an emulated reflecting superposition eye. (d) An enlarged view of the conical structures and clear zone. Reflected light through the conical structures propagates in two different directions, depending on the number of reflections on the conical structure. Scale bars are 200 μm in (a) and (c), 25 μm in (b), and 50 μm in (d). Adapted with permission from [85] John Wiley & Sons. Copyright © 2012 WILEY-VCH Verlag GmbH & Co. KGaA, Weinheim.

### 4.2. Artificial compound eyes on curved surfaces

Conventionally, the ACEs are achieved on flat substrates due to tremendous challenges of fabricating optical units on curved surfaces. Limited by the planar configuration, it is difficult to achieve the wide FoV larger than 90° on these flat ACEs. To mimic the natural compound eyes with omnidirectionally arranged optics and wide FoV, several micro-fabrication techniques have been developed in the past two decades, and curved optics for both apposition and superposition compound eyes were realized.

4.2.1. Apposition compound eyes on curved surfaces. The development of the laser direct writing technology provides a promising method to fabricate 3D microstructures on curved substrates. With a tight-focused femtosecond laser beam, features at the nanometre-scale can be generated on polymers by means of the two-photon polymerization process [86, 87], which makes it possible to fabricate micro-optical units such as microlenses with smooth surfaces. Wu *et al.* demonstrated a curved MLA inspired by the apposition compound eyes utilizing an improved femtosecond laser direct writing technology [88], as shown in figure 25. Each lens has a hexagonal shape with diameters on the order of 10 μm, which offers a fill factor of 100%. The surface roughness of the microlenses is about 2.5 nm, which can provide high quality imaging and light focusing properties. This technology has the potential

to achieve curved micro-optics of apposition compound eyes with an FoV beyond 90°. Nevertheless, the fabrication efficiency of such laser direct writing process is intrinsically low because the laser beam must be scanned to form the structure point by point. Therefore, it is not practical to fabricate large-area MLAs on curved surfaces through this type of fabrication process. In addition, the two-photon polymerization process can only be performed on photosensitive resists that might have lower transmittance rate in visible-NIR spectral range than other polymer and glass materials.

Chen and co-workers developed a high-efficiency fabrication process to generate large-area MLAs on glasses by combining the femtosecond laser irradiation with a chemical etching process, namely femtosecond laser enhanced chemical etching process [89]. Instead of scanning the laser beam to form the microstructures, this method only requires a single shot of the laser beam for each microlens, and the concave hemispherical microstructures with smooth surfaces can be fabricated by the accompanying chemical etching process. This method can significantly improve the efficiency of the fabrication process. Tens of thousands of microlenses with diameters ranging from a few micrometres to hundreds of micrometres can be fabricated within 3 h. Based on this approach, Liu *et al.* from the same research group demonstrated an apposition ACE encompassing 7600 hexagon-shaped microlenses on a hemispherical polymethylmethacrylate (PMMA) shell with a diameter of 3.55 mm, and accomplished an FoV of 150°, as shown in figure 26 [90]. First, the concave MLA was fabricated on a glass substrate by the femtosecond laser enhanced chemical etching process. Then, a convex MLA was replicated on a flat PMMA film. The flat film with the MLA was bent to the hemispherical shell with a heated glass ball (95 °C). The temperature of the glass ball needed to be precisely controlled, so that the microlenses would not be damaged during the bending process. An alternative approach was developed by Bian *et al.* to avoid the distortion of the microlenses during the bending process [91]. The mould with concave microlenses were directly fabricated on a concave hemispherical glass substrate, and the apposition ACEs were reversely replicated on the polymers. One advantage of the femtosecond laser enhanced chemical etching process is that the shape, arrangement and curvature of the microlenses can be flexibly adjusted by the laser parameters. This capability allows for fabrication of MLAs with non-uniform shapes and lens densities. Chen's group demonstrated such MLA on a curved surface, mimicking the apposition compound eyes of dragonflies, which has the potential to improve the resolving power of the ACE devices [92].

The laser based fabrication processes can achieve omnidirectionally-aligned microlenses equivalent to the facet lenses of natural compound eyes. However, in natural apposition compound eyes, the facet lenses are usually connected with photoreceptor cells by the crystalline cones, forming the optically isolated ommatidia. Lee and co-workers demonstrated a novel fabrication process based on soft lithography followed by a self-writing process that could generate artificial light-guiding polymer cones connected with the microlenses [93]. Such polymer cones are anatomically as well as functionally close to their natural counterparts, as shown
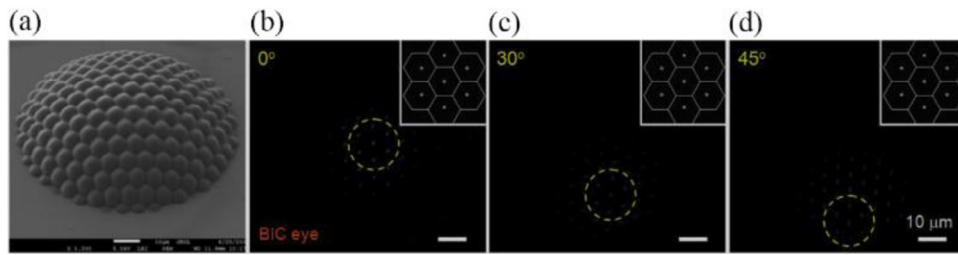
Figure 25. (a) SEM image of a microlens array on a curved surface. (b)–(d) The light spots focused by the microlenses when the incident angle of the light source is at 0°, 30° and 45°, respectively. No distortions of the focused light spots are observed, showing excellent focusing capability of the fabricated device. Scale bars: 10 μm. Reprinted from [90], with the permission of AIP Publishing.
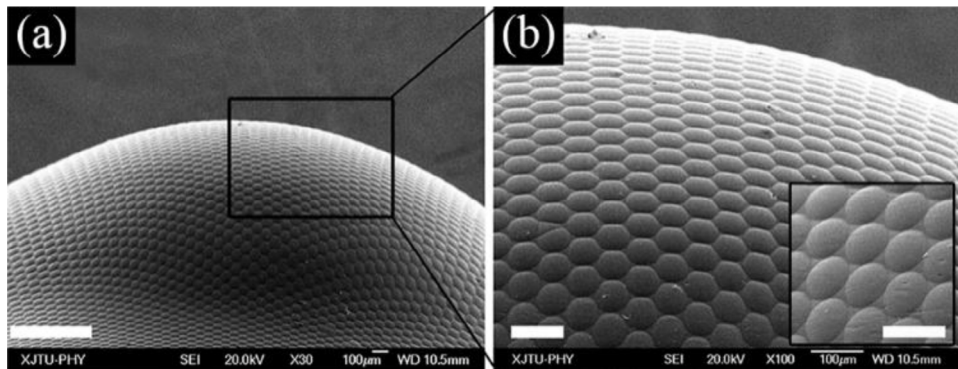
Figure 26. (a) An SEM image of the omnidirectional microlens array. The scale bar is 1 mm. (b) Enlarged SEM images of the microlenses on top of the hemispherical shell. The scale bar is 100 μm. Inset: the microlenses on the outer ring of the hemispherical shell (the scale bar is 100 μm). From [93]. Reprinted with permission from AAAS.

in figures 27(a)–(d), which can collect the light from the microlenses to the photodetectors. The synthesis of artificial polymer light-guiding cones was achieved by using a microlens-assisted self-writing of waveguides and two cross-linking mechanisms in a photosensitive polymer resin. UV light was focused by the microlenses moulded by a photosensitive polymer resin and was self-trapped after passing the focal plane because of the refractive index change during the photopolymerization process, as shown in figures 27(e) and (f). The light can be coupled into and propagate along the waveguides through the microlenses, as demonstrated in figure 27(g).

Besides the laser-based fabrication processes to fabricate artificial apposition compound eyes, several other technologies have also been developed. For example, Kuo *et al.* developed a technology to manufacture curved MLAs by combining the self-assembly of colloidal crystals, soft lithography and thermo-pressing processes [94]. Wang *et al.* proposed a novel hierarchic reflow method that involves multiple layers of photoresists to fabricate MLAs on millimetre-scale photoresist domes, which is compatible with the standard semiconductor manufacturing process [95]. Zhao *et al.* developed a single-step process for fabricating curved MLAs by injecting sol-gel glass droplets onto curved substrates [96].

4.2.2. Superposition compound eyes on curved surfaces. Owing to their unique structures and imaging mechanism, compared with the apposition compound eyes, superposition compound eyes have several additional advantages. For example, because each photoreceptor in the superposition compound eye receives the light collected from multiple adjacent optical units, the photosensitivity of the eye could be much higher than the apposition compound eyes whose photoreceptor is connected to a single lenslet [1]. The reflecting superposition compound eyes (RSCEs) in some decapods (e.g. shrimps, lobsters and crayfish) are also known to possess superior optical properties such as minimum chromatic aberration and wide applicable spectral range due to their unique lens-free, reflection-based imaging mechanism [97].

These fascinating characteristics, once implemented into existing optical imaging devices and systems, could benefit a wide variety of demanding applications in real-time motion tracking, surveillance, medical imaging and astronomy. However, the majority of research on RSCEs can only demonstrate the incorporation of the principles of RSCEs into large-scale apparatus such as astronomical telescopes and inspection equipment only within the spectrum of x-ray wavelengths [98–100].

Up till now, life-sized, device-level artificial RSCE that can form real, sharp images in the visible spectrum has only been accomplished by Jiang and co-workers [101]. The results of their RSCE device are shown in figure 28. The reflecting mirrors on the RSCE were achieved by a 410×410 array of high aspect-ratio Si micro-square tubes coated by a thin layer of aluminium (Al) film with a thickness of 400 nm (figures 28(a)–(c)), fabricated utilizing MEMS techniques. The Si micro-square-tubes were then transferred onto a hemispherical PDMS dome with a radius of curvature of 1.1 cm (figure 28(d)), so that light from an object can be reflected and focused by smoothened facets (figure 28(e)) of the adjacent micro-square-tubes onto the image plane to form a real image.
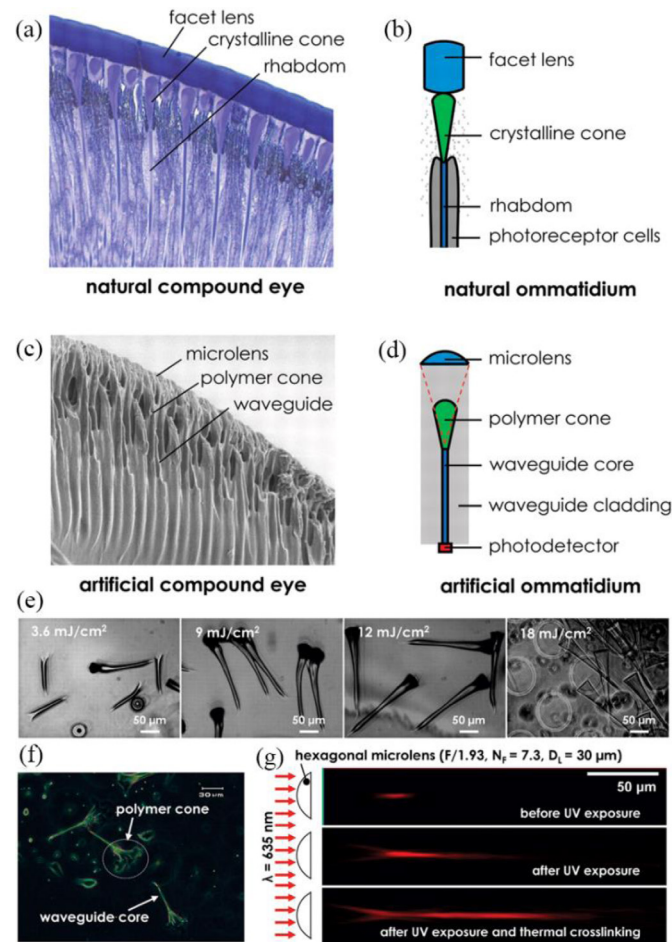
Figure 27. (a) An optical micrograph of a natural compound eye. (b) A schematic illustration of an optical unit in a natural compound eye. (c) An SEM image of the fabricated artificial compound eye. (d) A schematic illustration of an artificial ommatidium. (e) Waveguide cores and polymer cones fabricated by a self-writing process with different power of UV exposures. (f) A dark-field micrograph of waveguide cores and polymer cones. (g) Confocal micrographs of coupling light at 635 nm into the artificial ommatidium before UV exposure (top), after UV exposure (middle), and after UV exposure and thermal cross-linking (bottom). [88] John Wiley & Sons. © 2014 WILEY-VCH Verlag GmbH & Co. KGaA, Weinheim.

To fully characterize the performance of the artificial RSCE in terms of focusing, imaging capabilities and image quality, real focused images were generated by a collimated laser beam (figure 28(f)) and a non-collimated point source (e.g. a laser beam diffused by a piece of ground glass) illuminated on real objects (figures 28(g)–(i)). All the images shown in figure 28 were acquired without any post-image processing. The intensity ratio between the focused image and the surrounding cruciform pattern characteristic to RSCEs, a key factor associated with the overall image quality, was dictated by the aspect ratio of each square-micro-tube. This ratio was 3, close to that found in natural RSCEs (i.e. 2–3) [102]. One of the most attractive features of RSCEs unmatched by existing refraction-based optical imaging devices is their ability to achieve minimum chromatic aberrations in the focused images, which can be demonstrated in figures 28(j) and (k) with a non-collimated white light source. The focused image produced by the artificial RSCE (figure 28(j)) showed no signs of chromatic aberration while that produced by a conventional, commercial plano-convex lens (figure 28(k)) clearly revealed strong chromatic aberration along the boundaries separating the bright

and dark parts of the image (fringes of colors of purple and yellow).

4.2.3. Curved artificial compound eyes with image sensors. Pixel-to-pixel integration of a curved MLA with the matching image sensor to form a curved artificial compound eye is still a challenging task. Therefore, only a few works have been demonstrated to achieve functional curved ACEs. Rogers and co-workers published the first artificial compound eye that mimics the hemispherical, compound apposition layouts of natural arthropod eyes [103]. Based on the concepts of flexible photodetector arrays [52, 53] that they developed and stretchable electronics [104], an artificial apposition compound eye with a 16-by-16 convex MLA butt-coupled with matching photodetectors was assembled into a nearly hemispherical configuration with an FoV of 160°. Figure 29(a) presents schematic illustrations of the two main subsystems of the devices [103]. The first subsystem provides optical imaging function with the microlenses fabricated on a PDMS sheet. The second subsystem enables photo-detection and electrical readout, which consists of a matching array of thin,
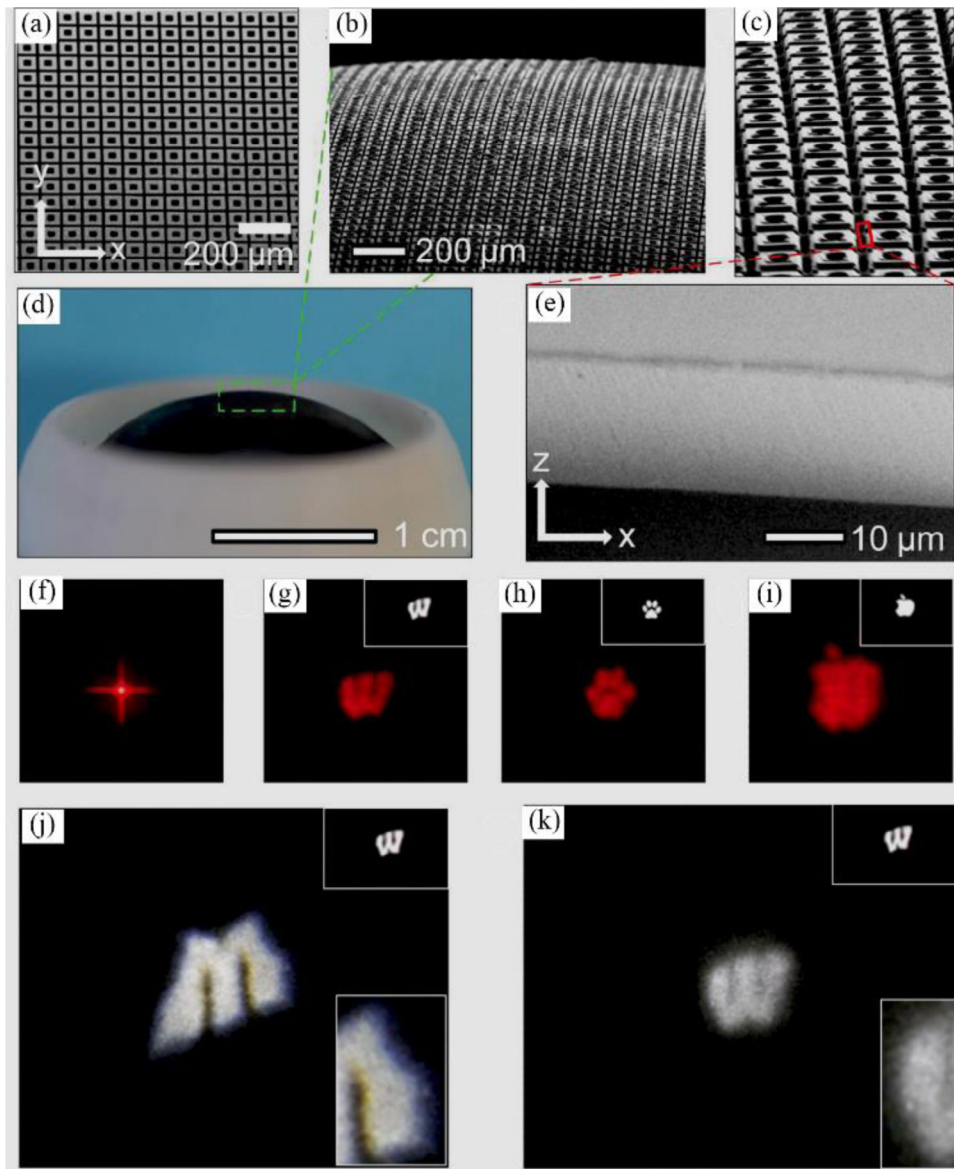
Figure 28. Results of an artificial RSCE. (a)–(e) SEM images and photo of the artificial RSCE. The Si micro-tubes are fabricated and transferred onto a hemispherical PDMS shell. The polishing process can generate smooth inner surface of the tubes than can reflect and focus the light onto the imaging plane. (f) The focused laser point by the device. Multiple reflections of the light inside the tube form the cross pattern. (g)–(i) Real images formed by the device. (j) and (k) Images of the logo of University of Wisconsin-Madison formed by a refractive camera lens and the artificial RSCE, respectively. Chromatic aberrations can be observed in the image generated by the camera lens. Adapted with permission from [101] John Wiley & Sons. © 2014 WILEY-VCH Verlag GmbH & Co. KGaA, Weinheim.

Si photodiodes and blocking diodes in an open mesh configuration with the capability for matrix addressing. The hydraulic actuation could accurately transform the planar layout, in which these separate subsystems were constructed and bonded together, into a fully hemispherical shape (figure 29(b)) without any change in optical alignment or adverse effect on electrical or optical performance. The complete device is demonstrated in figure 29(c). In this proof-of-concept work, the angular resolution of the compound eye was relatively low due to the limited number of pixels of the device. In order to capture high resolution images, a complete image reconstruction strategy was developed in both hardware and algorithm, by scanning the device in two orthogonal directions with a step of 1.1°. Figure 29(d) shows two reconstructed images of

complicated patterns. The authors successfully demonstrated the advantages of the hemispherical compound eye imaging device in terms of wide FoV, low off-axis aberrations and nearly infinite depth of field.

Aside from hemispherical ACEs based on flexible electronics and optics, Floreano *et al.* proposed another approach to the design and fabrication of curved ACEs, named CurvACE [105]. The process is based on a planar fabrication technology for an array of artificial ommatidia, followed by high-precision cutting (dicing) of the rigid ommatidia layers to add bendability. The design, fabrication process and the photo of the fabricated device are demonstrated in figure 30. The artificial ommatidia consist of three layers that are fabricated on rigid printed circuit boards (PCB) employing standard
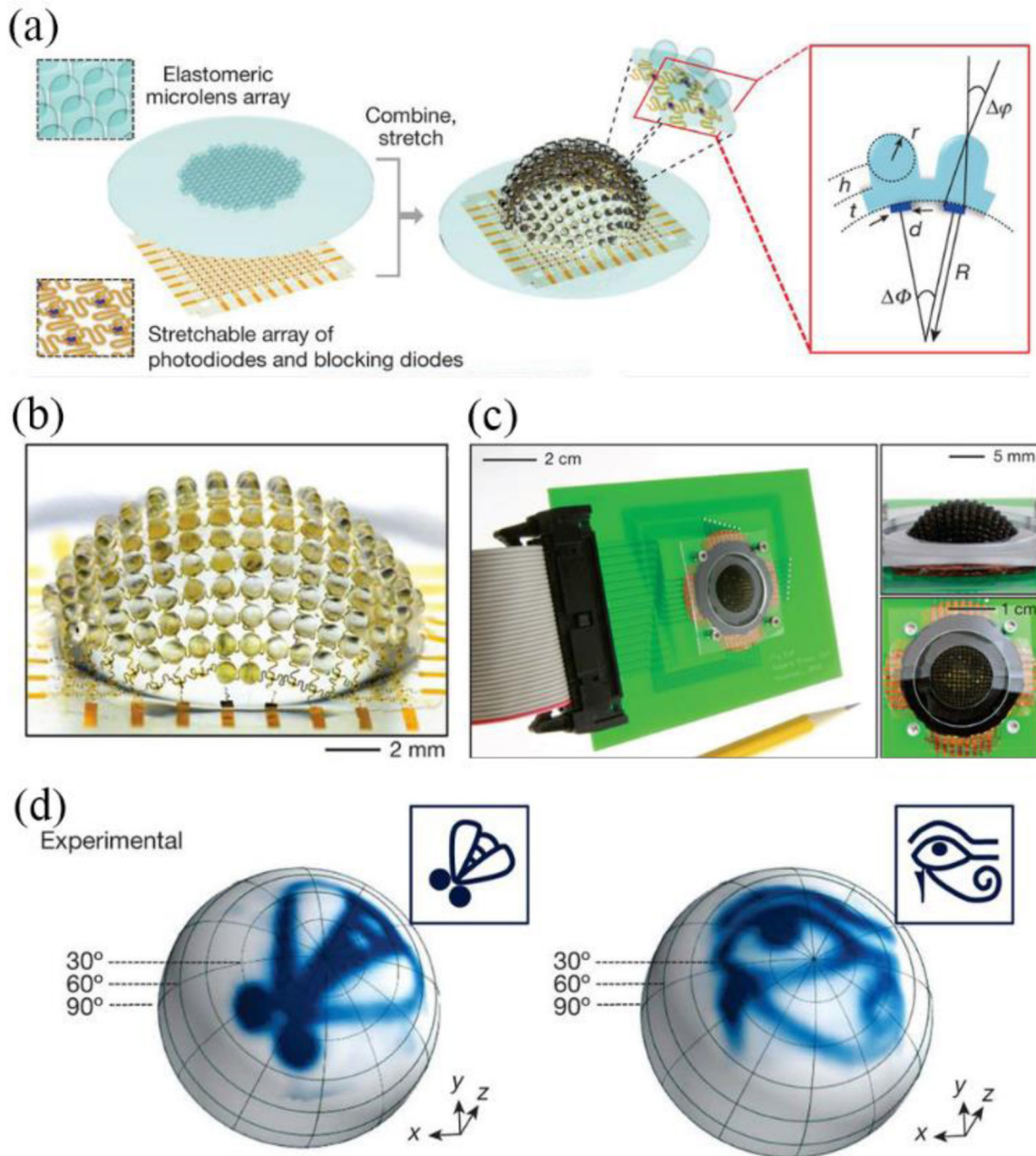
Figure 29. Results of a hemispherical artificial compound eye. (a) Illustrations of an array of elastomeric microlens and their supporting posts joined via a membrane (above) and a corresponding collection of Si photodiodes and blocking diodes interconnected by filamentary serpentine wires and configured for matrix addressing (below). (b) Image of the device after deformation into the hemispherical shape. (c) Photograph of the complete device mounted on a printed circuit board as an interface to external control electronics. (d) Pictures of line-art illustrations of a fly and a 'Horus eye' captured with the device. Adapted with permission from Springer Nature Customer Service Centre GmbH: Nature. [103] © 2013.

microengineering technologies. Next, the rigid optical and photodetector layer stack is precisely separated in columns of ommatidia with a chip dicing saw down to the flexible interconnection layer, which remains intact. This approach to artificial compound eye ensures accurate and reproducible alignment of the optical components and photodetectors, enabling fabrication of high-resolution imaging device that is comparable to its natural counterparts. However, the diced boards can only be bended in one direction, forming a semi-3D configuration of the device, as shown in figure 30(b).

Therefore, the FoV of the artificial compound eye fabricated by this process can only be expanded in one direction.

4.3. ARS on compound eyes

Single- or multi-layer coatings have been conventionally applied on optical surfaces to reduce light reflection and to make high performance photonic devices. However, the anti-reflective coatings suffer several limitations such as narrow wavelength range, limited angle of incident light to achieve
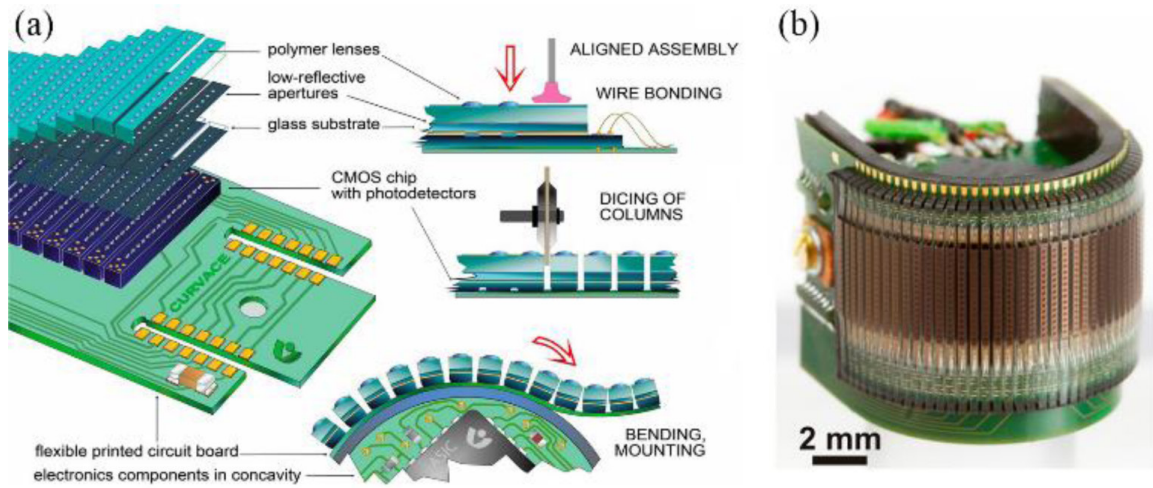
Figure 30. (a) Design and fabrication process of CurvACE. The artificial ommatidia consist of three layers: optical (microlenses and apertures), photodetector (CMOS chip), and interconnection (PCB). The layers are aligned and assembled in a planar configuration. Then, the artificial ommatidia are diced in columns down to the flexible interconnection layer, remaining intact. Finally, the artificial ommatidia are bent and attached to a rigid semi-cylindrical substrate. (b) An optical image of CurvACE. Adapted with permission from [105]. Copyright © 2013 National Academy of Sciences.

antireflection, and lack of suitable materials. Because of these reasons, moth eye nanostructures have garnered intense research interest in recent decades due to its superior antireflection properties, both broadband and omnidirectional [106], and wide applications in photonic devices. Starting from the seminal work presented by Clapham *et al.* [107] that first succeeded in reproducing moth eye nanostructures, researchers have developed many methods to fabricate moth-eye inspired nanostructures on a variety of materials, and have realized advanced materials that exhibit low reflection, high transmission, or high absorption properties. These advanced materials have been used in many applications such as solar cells, imaging lenses, and lighting devices.

Researchers have been studying and optimizing antireflection properties in various materials from transparent ones for high transmission to translucent or opaque ones for high absorption.

4.3.1. High transmission of light. Replication methods using diverse templates or etching techniques have been developed to construct ARS on transparent polymer or glass substrates. One of the representative works of ARS on transparent materials is credited to Choi *et al.* who demonstrated a highly transparent polymer film that had parabolic nanostructures [108]. For transparent substrates, reflections occur on both sides of the substrate. Consequently, ARS were fabricated on both sides of the substrate to maximize light transmission. They used a multi-step anodization and etching method to optimize the shapes of nanostructures on an anodized aluminium oxide (AAO) template and replicated the nanostructures to PMMA substrates. As shown in the SEM images of figure 31(a), the shape of nanostructures was changed from resembling pillars to parabola with increasing number of anodization and etching steps. The film fabricated with 5-step anodization and etching exhibited average transmittance of 99.4% in the wavelength range from 400 nm to 800 nm and substantial improvement in the range of angle of incident light

compared with the smooth surface film. Despite the superior performance of ARS, though, their commercial implementation has been limited due to the low mechanical stability and low productivity. The same research group improved the mechanical stability and productivity by changing the structures from positive to negative ARS and developing a roll-to-roll thermal imprinting process [109].

The other approach to making highly transparent substrates is coating a film that has ARS on a target substrate [110–115]. This approach has the advantages of easy fabrication and avoiding modification of the target substrate. Using this approach, Raut *et al.* demonstrated an antireflective film with superior mechanical, chemical, and thermal stability for commercial applications [110]. They coated polyhedral oligomeric silsesquioxane-based (POSS) materials on both sides of glass substrates and fabricated ARS on the POSS materials by nanoimprint lithography. Figure 31(b) shows that ARS were well constructed on both sides of the glass substrate and they clearly suppress the light reflection on the glass substrate.

Etching, instead of replicating nanostructures from templates, is another technique to construct ARS on transparent substrates. Researchers have achieved highly transparent glass substrates by etching on both sides of the glass substrates [116, 117]. Oh *et al.* not only demonstrated the improvement of transmission, but also proposed other benefits, such as signal improvement in fluorescence and surface enhanced Raman scattering (SERS), and high contrast imaging by using self-ARS [117]. In their work, double-side glass nanopillar arrays (DS-GNA) served as self-ARS and silver (Ag) nanoislands were applied on GNA to make a plasmonic substrate (figure 31(c)).

ARS possess other intriguing functions such as self-cleaning [118–121] and antifogging [122]. The ARS constructed on hydrophobic materials or treated with hydrophobic materials exhibit super hydrophobicity and a self-cleaning effect because water dropped on the super-hydrophobic surface can easily roll off and collect particles in the process to clean the
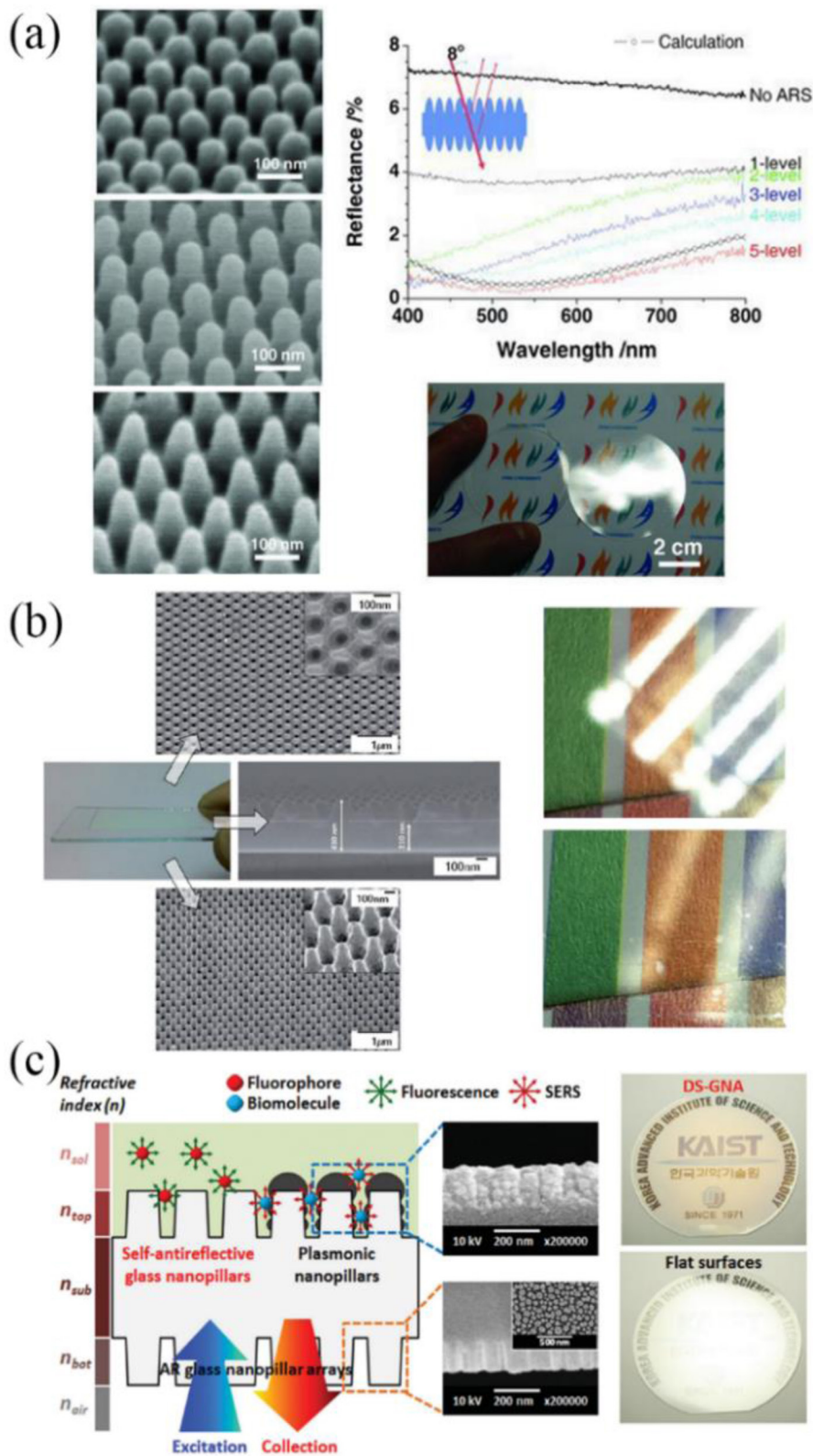
Figure 31. ARS for high transmission. (a) SEM images (left) of PMMA ARS replicated from AAO templates with a 1-step (top), 3-step (middle), 5-step (bottom) anodization and etching process, respectively. Measured and calculated transmittance values (top right) of the Adapted with permission from [108] John Wiley & Sons. Copyright © 2010 WILEY-VCH Verlag GmbH & Co. KGaA, Weinheim. (b) An optical image of a glass substrate with antireflective films and SEM images of ARS fabricated on both sides of the glass substrate (left). Optical images of reflected light (right) from the glass without (top) and with (bottom) ARS. Adapted with [110] with permission of The Royal Society of Chemistry. (c) Schematic diagram and SEM images of biophotonic surfaces with self-ARS (left). Glass nanopillar arrays (GNA) can increase signals of fluorescence and SERS. Light reflection from a glass substrate with double-side GNA (DS-GNA) (top right) and a flat glass substrate (bottom right). Adapted with permission from [117] John Wiley & Sons. © 2014 WILEY-VCH Verlag GmbH & Co. KGaA, Weinheim.
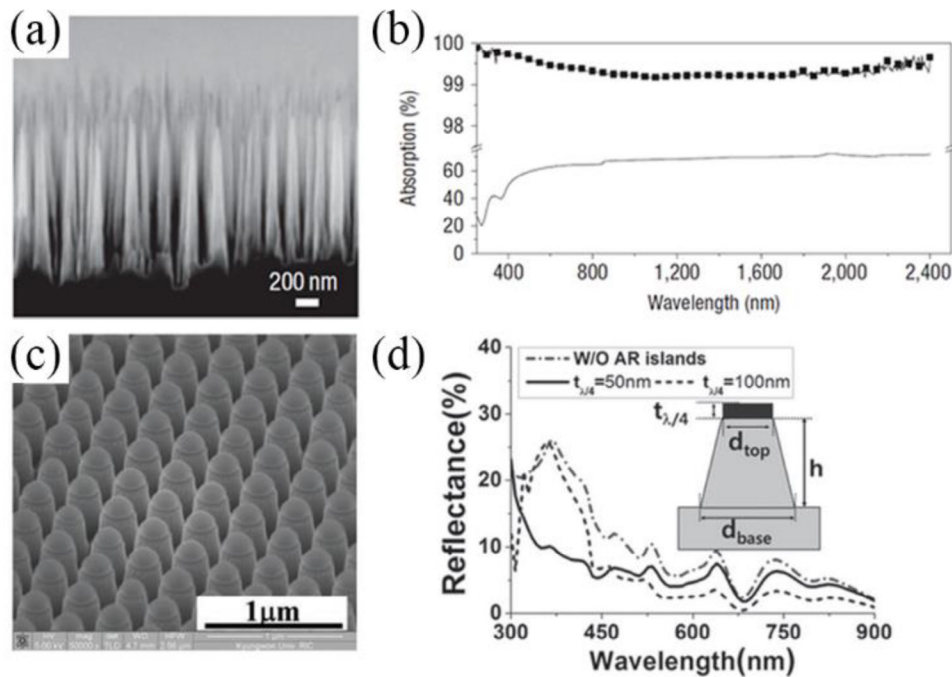
Figure 32. ARS for high absorption. (a) An SEM image showing a cross-sectional view of Si nanotips (SiNTs) 1600 nm long. Reproduced with permission from Springer Nature Customer Service Centre GmbH: Nature Nanotechnology. [126] © 2013. (b) Absorption values of Si substrates with (filled squares) and without (solid line) SiNTs in UV–VIS–NIR wavelength range. Reproduced with permission from Springer Nature Customer Service Centre GmbH: Nature Nanotechnology. [126] © 2013. (c) An SEM image of Si nano-conical-frustum (NCF) arrays integrated with PS nanoislands. Reproduced with permission from [123] John Wiley & Sons. Copyright © 2011 WILEY-VCH Verlag GmbH & Co. KGaA, Weinheim. (d) Simulation results with two different thicknesses (50 nm and 100 nm) of antireflective nanoislands on top of NCF arrays and without nanoislands (d_{top} = 300 nm, d_{base} = 500 nm, h = 500 nm). Reproduced with permission from [123] John Wiley & Sons. Copyright © 2011 WILEY-VCH Verlag GmbH & Co. KGaA, Weinheim.

surface. Especially for outdoor applications, this self-cleaning function is crucial to maintain optical performance of photonic devices. The antifogging function can be achieved utilizing ARS with hydrophilic materials or hydrophilic surface treatment. This function enables clear view through the substrate by avoiding light scattering of water droplets in moisturized environment.

4.3.2. High absorption of light. Highly absorptive ARS have been developed using various kinds of materials such as Si [123–126], GaP [127], InP [128], ZnO [129], and GaAs [130] over the past decades for highly efficient solar cells and other photonic device applications. Among the previous works, Huang *et al.* demonstrated outstanding performance of ARS on a Si substrate. They fabricated Si nanotips (SiNTs) on a large-area (6-inch diameter) Si substrate by high-density electron cyclotron resonance plasma etching (figure 32(a)) [126]. The SiNTs exhibited antireflection property in an extremely wide range of wavelengths, roughly from 0.3 to 1000 μm. The SiNTs 1.6 μm long showed high absorption values over the UV to NIR regions (figure 32(b)). The same research group also increased the length of SiNTs up to 16 μm, realizing antireflective property up to the terahertz region (THz, 200 to 1000 μm) from the SiNTs. The SiNTs showed not only broadband antireflection, but also wide-angle and polarization independent antireflective properties.

In contrast to the method using only tapered nanostructures to achieve gradient index of refraction, Park *et al.* proposed a combination of ARS and antireflection coating [123]. They

fabricated Si nano-conical-frustum (NCF) arrays integrated with antireflection nanoislands by colloidal lithography and a single-step deep reactive ion etching (DRIE) process (figure 32(c)). This method can suppress the reflection of light in the near-UV (NUV, 300 to 400 nm) spectral range without the need to fabricate nanostructures with sub-300 nm feature size (figure 32(d)). The NUV spectral range is important for the performance of Si solar cells because large portion of solar energy available to Si solar cells is in the shorter wavelength range (300 to 500 nm). The research group demonstrated that antireflection nanoislands on top of NCF arrays could effectively reduce reflectance in the NUV region.

4.3.3. Solar cell application. Beyond developing fabrication methods of ARS and measuring their optical properties, researchers have tried to implement the ARS in particular applications. Improving the efficiency of solar cell is one of the key applications of ARS, by enhancing the light transmission of the transparent substrate or the light absorption of the active layer.

Heo *et al.* improved the efficiency of solid-state dye-sensitized solar cells (ssDSSCs) by using moth-eye inspired nanostructures [118]. The ARS were constructed on the fluorine-doped tin oxide (FTO) glass by soft lithography (figure 33(a)). PFPE was selected as a mould material to achieve good pattern resolution, and ARS were replicated on a UV-curable resin. The efficiency of ssDSSCs with ARS was 7.3% at 100 mW cm^{-2}, higher than that of ssDSSCs without ARS (6.6%). Another research group also fabricated moth-eye inspired
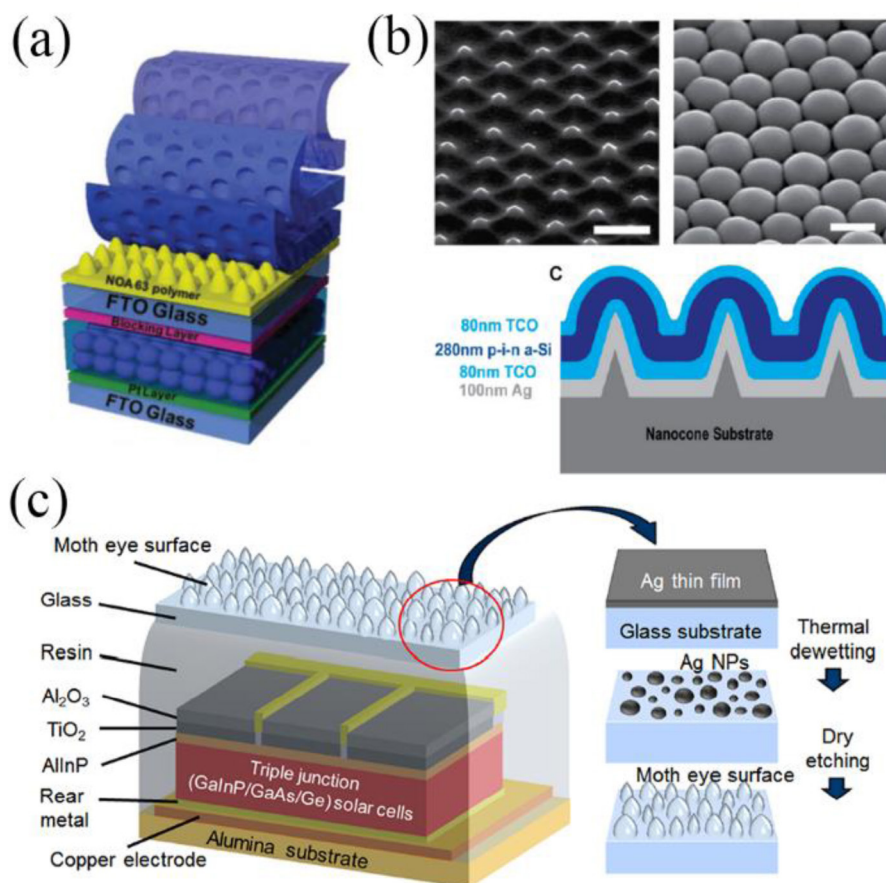
Figure 33. ARS in solar cells. (a) A schematic diagram of ssDSSCs with moth-eye inspired nanostructures fabricated on an FTO glass substrate using the NOA 63 UV-curable resin and a PFPE mould. Reproduced with permission from [118] John Wiley & Sons. © 2013 WILEY-VCH Verlag GmbH & Co. KGaA, Weinheim. (b) SEM images of nanocone (top left) and nanodome structures (top right). Scale bar: 500 nm. A schematic diagram of nanodome solar cells constructed by depositing multilayers of materials on nanocones. Reprinted with permission from [120]. Copyright (2010) American Chemical Society. (c) A schematic diagram of a CPV device with moth-eye inspired nanostructures (left) and the fabrication procedures (right). Reproduced from [132]. CC BY 3.0.

nanostructures on the glass substrate of their organic solar cells (OSCs) by using a PFPE mould and enhanced the power efficiency [131]. In contrast to the work of Heo *et al.*, nanostructures were also formed on the active layer, which made further improvement in the power efficiency by light trapping in the active layer of OSCs.

A research group at Stanford University developed nanodome structures to enhance the power efficiency of hydrogenated amorphous Si (a-Si:H) solar cells [120]. The nanodome solar cell was fabricated by depositing multilayers of materials consisting of Ag, transparent conducting oxide (TCO), and a-Si:H, on a nanocone quartz substrate (figure 33(b)). As in the moth-eye nanostructures, the shape of nanodome structures produces a graded refractive index profile that exhibits an antireflective effect. In addition, the nanodome structures efficiently coupled the incident light to and guided it in the a-Si:H layer, while the TCO layer reduced the surface reflection due to its lower refractive index than that of a-Si:H. Because of these effects, the nanodome solar cell achieved 94% of light absorption in the wavelength range of 400–800 nm, much higher than the flat film devices with 65% of light absorption. Furthermore, the power conversion efficiency of the

nanodome solar cells was improved by 25% compared to the flat film device.

A research group at Gwangju Institute of Science and Technology (GIST) used moth-eye nanostructures to improve the power efficiency of III–V based concentrated photovoltaic (CPV) systems [132]. Moth-eye inspired nanostructures were fabricated on a cover-glass substrate by forming thermally dewetted Ag nanoislands as etch masks and etching the glass substrate with inductively coupled plasma RIE (ICP-RIE) (figure 33(c)). The constructed moth-eye nanostructures exhibited broadband antireflection at wavelengths from 300 to 1800 nm, which is the light absorption range of III–V multijunction solar cells. Under both one-sun and concentrated light conditions, the cover glass with moth-eye nanostructures consistently showed enhanced power efficiency compared to the flat cover glass. The maximum efficiency of the device with moth-eye nanostructures was 42.16% at 196 suns, 7.41% higher than that of a flat cover glass.

4.3.4. Imaging applications. Imaging lenses are one of the main devices to implement antireflective coatings that can provide higher image quality by reducing light reflection loss,

improving image contrast, and eliminating ghost images. Single- or multi-layer coatings are conventionally applied on a lens surface. However, as mentioned above, a simple coating method cannot achieve broadband high transmission in a variety of materials. ARS were a promising solution to this issue, but a challenge is present to make nanostructures on a curved surface. In the recent decade, researchers have been developing methods to fabricate ARS on lens surfaces.

To enhance light transmission of microlenses, Jung *et al.* fabricated ARS on MLAs by oxygen plasma etching with an Ag nanoisland mask [133]. Figure 34(a) shows the SEM images of ARS on microlens surfaces and optical images of MLAs without (top right) and with (bottom right) ARS that clearly show that ARS can reduce light reflection on the microlens surfaces. The reflectance of the MLA with optimized ARS decreased to below 4% in a wide range from 490 nm to 630 nm in wavelength. Furthermore, the imaging brightness through the MLA with ARS was increased by 67% compared with that without the ARS. In addition to this etching method, other approaches have been developed to form ARS on MLAs. For example, self-assembled polystyrene (PS) nanospheres on polymer MLAs [134] and a combination of an AAO template and a photoimprinting method [135] were used to construct ARS on MLAs.

Thanks to the recent development of large-area nanofabrication technique on curved surfaces, ARS can now be fabricated on millimetre-scale optical lenses. Yanagishita *et al.* precisely machined Al blocks to form lens surfaces and anodized the Al block to fabricate ARS. Polymer lenses with ARS were then fabricated by nanoimprinting or injection moulding [136]. Figure 34(b) shows that ARS are well replicated onto a lens surface and are able to efficiently reduce light reflection. Lee *et al.* demonstrated an antireflective optical lens with glass nanoholes [137]. They etched a glass layer with an Ag nanohole mask by RIE and controlled the size of the holes via further wet etching to fabricate antireflective glass nanoholes. This method realized forming ARS on a commercial optical lens. Optical images of letters through a bare lens and a commercial optical lens with glass nanoholes are shown in figure 34(c). The lens with glass nanoholes demonstrated less light reflection and formed a clearer image compared with the bare lens. Besides, glass nanoholes are 2.5 times higher in hardness than nanopillars.

In addition to the works of ARS on lenses with fixed curvature, a recent work demonstrated a tunable lens with ARS for biomedical applications [138]. ARS were well replicated onto a flexible membrane using a nanohole template. The lens placed at the distal end of an endoscope could be tuned in focal length by pressure control (Figure 34(d)). The tunable lens with ARS exhibited higher transmittance and MTF 50 values than a tunable lens with a smooth surface across different curvatures. The resolving power of the lens with ARS was improved by up to 56%.

4.3.5. Lighting applications. In addition to the imaging or solar cell applications, moth eye nanostructures can improve light extraction efficiency of lighting elements such as light
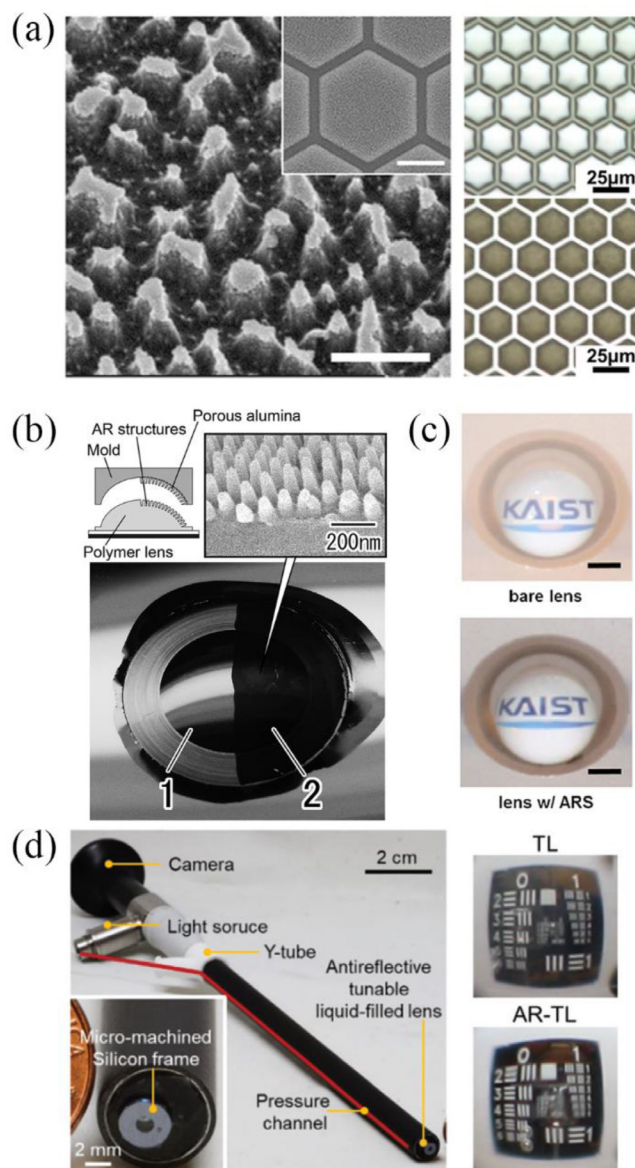
Figure 34. ARS for imaging applications. (a) SEM images of ARS on a polymer microlens array (left). Scale bar: 500 nm, (inset) 10 μm. Microscopic images of polymer microlens arrays (right) without (top) and with (bottom) ARS. Adapted with [133], with the permission of AIP Publishing. (b) An SEM image (top) of ARS on a lens and an optical image of a polymer lens without (1) and with (2) ARS, respectively. Reprinted from [136], with the permission of AIP Publishing. (c) Optical images of perspective views of a logo through a bare lens (top) and a lens with antireflective nanoholes (bottom). Reproduced from [137]. CC BY 3.0. (d) Optical images of a laparoscope with an antireflective tunable lens and the enlarged view of its distal end (left). Optical images of a USAF target through tunable lenses without (top) and with (bottom) ARS. Adapted from [138] with permission of The Royal Society of Chemistry.

emitting diodes (LEDs) or organic light emitting diodes (OLEDs). Due to the high refractive index of materials of LEDs or OLEDs, the generated light is trapped inside of the materials owing to the total internal reflection (TIR) or the Fresnel reflection. The moth eye nanostructures can resolve these problems by reducing the Fresnel reflection or by outcoupling the trapped light.
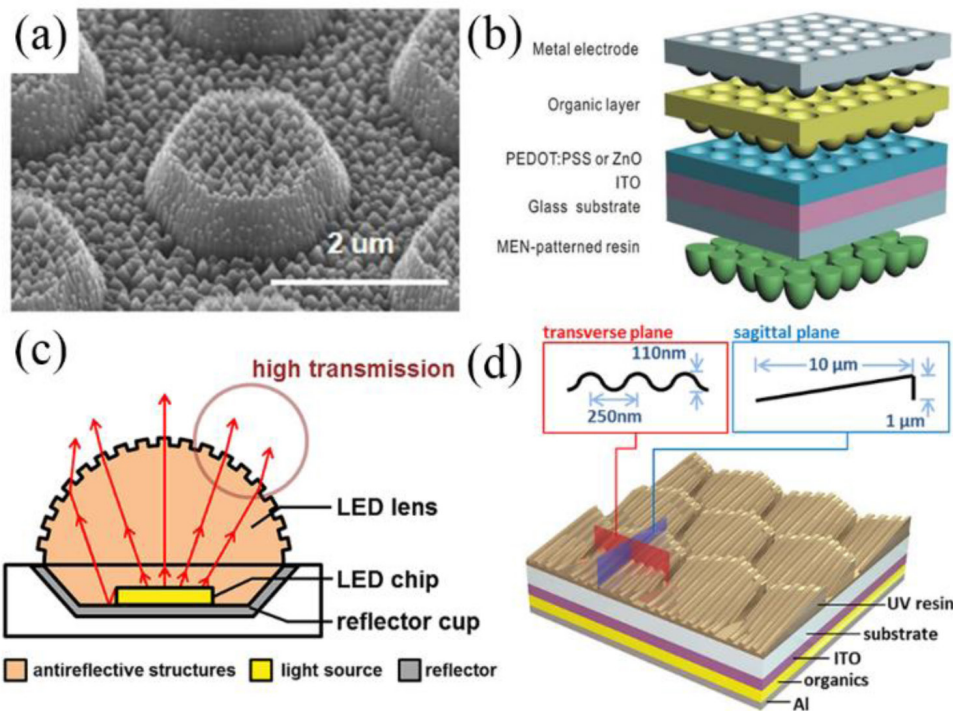
Figure 35. ARS for light extraction efficiency enhancement. (a) An SEM image of micro/nanostructures inspired from compound eyes on a GaP substrate. Reproduced from [139]. CC BY 3.0. Schematic diagrams of (b) organics-based optoelectronic devices (OLEDs and OSC) that have ARS inspired from moth eyes inside and outside of the device. Reproduced with permission from Springer Nature Customer Service Centre GmbH: Nature. [141] © 2015. (c) A high-power LED package that has a LED lens with ARS inspired from a firefly light organ. Adapted with permission from [142]. Copyright © 2012 National Academy of Sciences. (d) An OLED device that has hierarchical structures inspired from a firefly light organ. Reprinted with permission from [143]. Copyright (2016) American Chemical Society.

Song *et al.* improved the power efficiency of AlGaInP-based LEDs by using moth eye inspired micro/nanostructures [139]. In this study, it was demonstrated that the microstructures could extract the trapped light due to TIR above the critical angle, and the nanostructures could significantly suppress the Fresnel reflection below the critical angle by reducing the mismatch in refractive indices between the GaP substrate and the air. The micro/nanostructures were fabricated by RIE using two different etch masks that were thermally reflowed photoresist patterns and Ag nanoislands (figure 35(a)). After fabricating tapered microstructures by the first RIE process, an Ag thin film was deposited onto the microstructures and Ag nanoislands were formed by a dewetting process. The nanostructures on the microstructures were defined by the second RIE using Ag nanoislands as the etch mask. The light output power of AlGaInP LEDs with micro/nanostructures was increased by 72.47% compared with that of AlGaInP LEDs on a flat surface.

Moth eye inspired nanostructures can also be used to enhance the light extraction efficiency of OLEDs as well as LEDs. Li *et al.* demonstrated a simple method to improve the light extraction efficiency of white OLEDs by fabricating ARS on the fused silica substrate [140]. This method can increase the luminance efficiency of the OLED device by about 1.4 times in the normal direction compared with OLED device without any ARS. This relatively simple and efficient method can be applied to other OLEDs without modifying the design

or structures of OLEDs. In addition to this simple method, Zhou *et al.* developed an alternative method to enhance the light extraction efficiency of OLEDs by fabricating moth eye inspired nanostructures on internal and external layers (figure 35(b)) [141]. The same structure with different active layer was used to improve the efficiency of OSCs. The moth eye inspired nanostructures were constructed on the poly(3,4-ethylene dioxythiophene):polystyrene sulfonic acid (PEDOT:PSS) and ZnO for internal layers, and UV-curable resin for external layers by an imprinting process. The internal nanostructures of the PEDOT:PSS layer and the ZnO layer on an indium tin oxide (ITO) layer were fabricated for OLEDs and OSCs, respectively. The external nanostructures were fabricated on a glass substrate using UV-curable resin. The internal and external nanostructures can efficiently extract the trapped light by the scattering effect and increased transmittance of the ITO glass substrate. For the OLED with single electroluminescence (EL) units, the internal and external nanostructures can enhance the extraction quantum efficiency (EQE) by a factor of 1.69 and 1.77, respectively, compared with a conventional device. The combined double-nanostructure layers on both sides of the ITO glass substrate provide further enhancement of EQE by a factor of 2.46 compared with an OLED device without nanostructures. Furthermore, the OSCs with the moth eye inspired nanostructures showed improved light trapping performance compared with a flat substrate.

To improve the extraction efficiency of lighting devices, researchers tried to find a solution from bioluminescent light organs, such as a firefly light organ. Two different research groups at KAIST and the University of Namur, respectively, found intriguing photonic structures on the cuticles of firefly light organs. Interestingly, they found similar photonic structures in different species of fireflies. Kim *et al.* at KAIST studied the photonic structures on the light organs of two different species of fireflies including Luciola lateralis Motschulsky [142] and *Pyrocoelia rufa* [143]. They found longitudinal nanostructures from the light organ of Luciola lateralis Motschulsky and revealed the optical role of the nanostructures by both numerical analysis and experiment. The optical role of cuticular nanostructures is improving the light transmittance of the cuticle and enabling efficient light communication between fireflies by reducing the refractive index mismatch between the cuticle and the air. The bioinspired nanostructures were applied on an LED lens surface to achieve highly efficient LED lighting (figure 35(c)). The bioinspired LED lens can increase transmittance by up to 3% in visible spectrum under optimal lens curvature conditions compared with a smooth surface lens. The same research group also found hierarchical structures, longitudinal nanostructures on asymmetric microstructures, from the light organ of *Pyrocoelia rufa*. To reveal the optical role and properties of the hierarchical structures, they numerically analyzed and mimicked the hierarchical structures using combined fabrication methods such as geometry-guided resist reflow, PDMS oxidation, and replica moulding. The hierarchical structures can enhance light extraction by suppressing the TIR and Fresnel reflection. The asymmetric microstructures contribute to the extraction of trapped light above the critical angle by diffractive effect and changing the geometric conditions. The longitudinal nanostructures can reduce the Fresnel reflection by reducing the index mismatch and coupling out the trapped light above the critical angle by subwavelength diffraction. A bioinspired OLED panel was fabricated by combining the hierarchical structures on a glass substrate of an OLED device, which was in a similar configuration with a firefly light organ (figure 35(d)). The bioinspired OLED showed significant enhancement of EQE by up to 61% compared with an OLED device without the bioinspired structures. Furthermore, the bioinspired OLED have side-enhanced super-Lambertian emission, indicating that the hierarchical structures contribute to the emission of strong light signal in over a wide-angle range for efficient light communication between fireflies.

Another research group of University of Namur also found similar photonic structures on the light organ of a different species of firefly *Photuris* sp. (Lampyridae). They analyzed the photonic structures and revealed that the inclined microstructures can enhance the light extraction by helping the trapped light due to TIR escape [144]. They also fabricated bioinspired microstructures on a surface of a GaN-based LED and demonstrated improved extraction efficiency by up to 54% compared with a bare LED device [145].
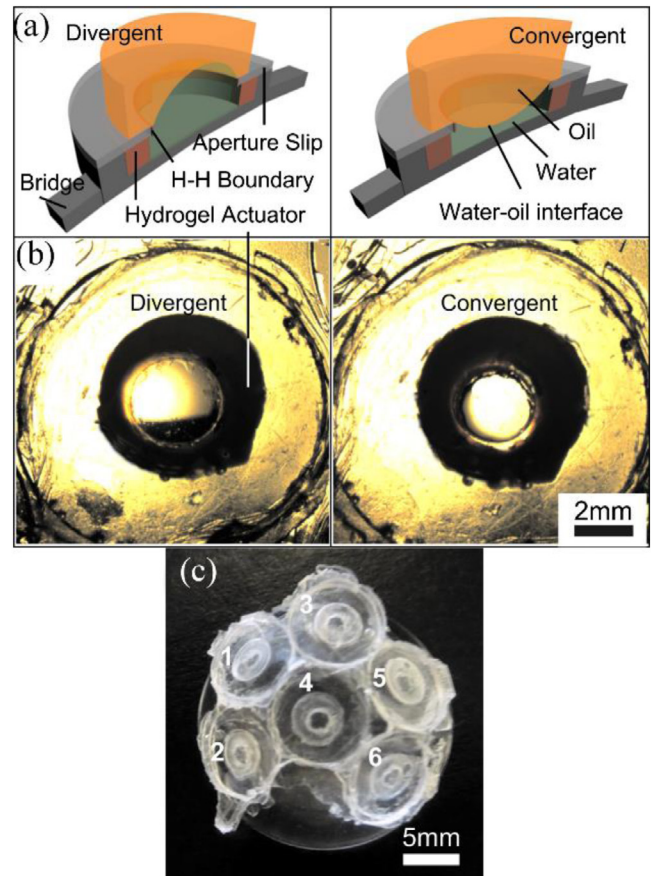

Figure 36. (a) Schematics of one microlens structure in divergent and convergent states, respectively. A round PDMS slip defining the lens aperture, a hydrogel actuator and the underlying polymer substrate form a water container. The sidewalls of the aperture are chemically treated hydrophilic by corona plasma discharge, while the top surfaces are naturally hydrophobic. A meniscus, used as a microlens, is formed through a curved interface between water and oil and is pinned by the hydrophilic–hydrophobic boundary, protruding upward at high pressure (divergent) and bulging downward at low pressure (convergent). (b) Photoimages of a microlens in the two states: divergent and convergent. The left image (divergent) is taken at around 50 °C; the right image (convergent) is taken at about 30 °C. (c) An image of a six-element microlens array on a dome with a diameter of 18 mm. Each microlens is labelled with a number. Reprinted from [15], with the permission of AIP Publishing.

5. Other visual systems

5.1. Inspired by both compound eyes and mammal eyes

The research described in section 4 mimicked the nature apposition compound eyes that possess a fixed focal length for each optical unit. Zhu *et al.* demonstrated an ACE device with a performance beyond its natural counterparts [15], integrating the capabilities of both compound eyes with wide FoV and mammal eyes (e.g. human eyes) with tunable focal length. As shown in figure 36, a six-element liquid-based MLA was fabricated on a dome. The focal length of each microlens could be individually tuned by a thermo-responsive hydrogel
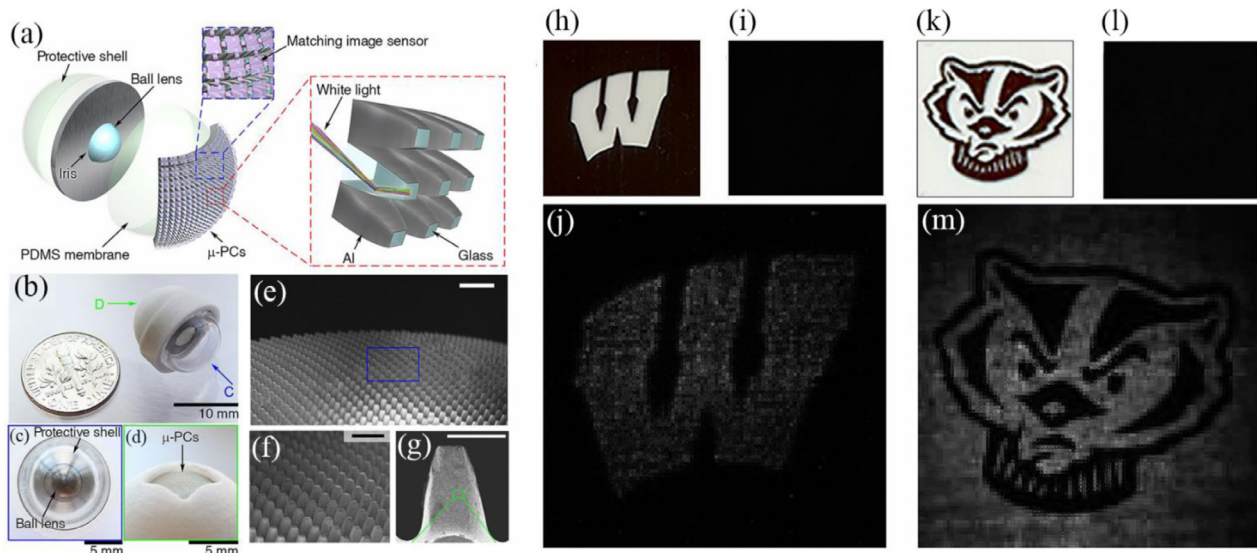
Figure 37. (a) Schematic illustrations of an artificial fish eye. (b)–(d) Photos of the artificial eye, its front view, and the BPE at the rear, respectively. (e)–(g) SEM images of the BPE transferred onto a hemispherical PDMS membrane and that of an individual μ-PC, respectively. The scale bars in (e)–(g) are 200 μm, 100 μm and 50 μm, respectively. (h)–(j) A scanned logo as the object, images obtained without and with BPE, respectively. (k)–(m) Another scanned logo with more complex structures, images acquired without and with the BPE, respectively. Adapted with permission from [160]. Copyright © 2016 National Academy of Sciences.

actuator. The range of the focal length varied from millimetres to infinity. The liquid microlenses were connected by PDMS bridges, which can be easily bent and wrapped onto curved surfaces. In their work, the six microlenses were arranged on caps subtending an angle of 116° (18 mm diameter dome) and 113° (20 mm diameter dome). The FoV of each microlens can be changed from 77° to 128°. Due to its broad potential applications in sensing, surveillance, security and military, this insect-human-hybrid eyes have become an attractive research topic. Several devices based on other actuation strategies have been developed [146–149].

5.2. Bioinspired photosensitivity enhancer

Improving the photosensitivity for low-light imaging devices is important for acquisition of visual information and is critical to many applications in medicine, military, security, and astronomy [150–154]. Current methods to improve photosensitivity generally resort to enhanced electronics, including the use of external image intensifiers or on-chip multiplication gain technologies, or highly photosensitive imaging sensors utilizing emerging photoactive materials [155–158]. These electronic devices are able to increase the overall photosensitivity of the imagers by several orders of magnitude; however, they have inevitable physical and material limitations [159].

Jiang and co-workers developed an all-optical approach to the improvement of the photosensitivity of imaging systems, which was inspired by the retinal structure of elephant nose fish [160]. In the retina of the elephant nose fish (Gnathonemus petersii), the collection of light (wavelength $\lambda \sim 615$ nm) in order to reach the photoreceptors is achieved by crystalline micro-cups with reflecting photonic crystal sidewalls [161]. This focusing mechanism of guiding light rays through an enclosed structure is much less prone to imperfection in optical elements, and thus provides a viable solution to accomplishing

superposition in man-made imagers. Figures 37(a)–(d) show the schematic illustration and the photo of an artificial fish eye for low-light vision. It consists of photosensitivity enhancer with thousands (48-by-48) of microphotocollectors (μ-PCs), as shown in figures 37(e)–(g), which are anatomically equivalent to the crystalline micro-cups in the retinae of the elephant nose fish. A ball lens that is mounted at the central iris generates a hemispherical image plane onto the μ-PCs that are arranged on a curved PDMS membrane. Each μ-PC is a glass microstructure with two opposite facets enclosed by four parabolic sidewalls coated with high-reflectivity Al. The incoming light from the large facet (input port, diameter $D_{in} = 77$ μm) is collected towards the small facet (output port, diameter $D_{out} = 20$ μm) by the parabolic sidewalls, consequently increasing the light intensity. In this manner, the μ-PCs realize superposition of the incoming light to the pixels on the imager. The resultant image can then be acquired by a matching image sensor.

To demonstrate the imaging capabilities of the bioinspired photosensitivity enhancer (BPE) that contained 48×48 μ-PCs, objects with a letter logo (figure 37(h)) and a more complex pattern (figure 37(k)) were used. At the low illumination condition (power intensity of light, $P = 0.05$ μW cm^{-2}), the images acquired by the CCD without the BPE could not be recognized (figures 37(i) and (l)). Much brighter images were obtained with the BPE and were easily seen (figures 37(j) and (m)). The spatial resolution of the eyes in the elephant-nose fish is reduced by its unique retina anatomical structure with crystalline microcups [161]. For the artificial device, a complete set of hardware and software strategy based on a super-resolution image reconstruction method was adopted to recover the resolution of images. In the example in figure 37(m), the resolution (384×384) was improved by 4 times, able to show fine spatial features and sharp boundaries of complex patterns.

5.3. Bioinspired polarization imaging sensors

Traditional image sensors can only detect intensity and wavelength of the light. There is a third characteristic of the light, namely, the polarization. In nature, some animals such as crustaceans, insects and aquatic creatures [162–164], can detect and make use of polarization of light. Inspired by these natural polarization-sensitive eyes, efforts have been made to develop image sensors that can detect the polarization of the incoming light. The earliest attempts to implement polarization imagers were made by integrating dichroic polymer thin films with orthogonal absorption axes on CMOS image sensors [165–167]. Another approach used micro-polarizer fabricated from a birefringent crystal deposited on top of the imagers [168, 169], which showed higher efficiency in separating orthogonal components of linearly polarized light than the dichroic polymer thin films [170].

All the methods mentioned above require complicated and expensive procedures that involve post-processing of image sensors and precise alignment of the polarization layers on top of sensor pixels. In addition, the filters on top of relatively thick oxide cause a poor extinction ratio for abnormal incident light beams since the incident light may strike the photodetector corresponding to a neighboring polarization filter [171]. In the past decade, thanks to fast development of nanotechnologies, more promising methods to realize polarization image sensosr were presented by integrating nanowire grids on the sensor pixel based on standard CMOS technology. For example, Tokuda *et al.* demonstrated a 30×30 polarization image pixel array with metallic nanowire grids covered on the photodiode region, and showed a sinusoidal variation of detected intensity as a function of the polarization orientation [172]. The extinction ratio was 2.03. Sarkar *et al.* showed a focal-plane nanowire grids in a more advanced, $0.18\ \mu$m standard CMOS process, and improved the extinction ratio to 6.3 and 7.7 with an orientation angle of 0° and 90°, respectively [173,174]. Recently, Garcia *et al.* demonstrated a low-power, high-resolution, color-polarization imager for real-time *in situ* imaging, which was inspired by the eyes of mantis shrimp [175, 176]. The imager could capture co-registered color and polarization information in real time with a resolution of 1280×720 and a dynamic range of 62 dB. The quantum efficiency was above 30% and the polarization extinction ratio was about 40 in each spectral channel, much higher than in previous works. The authors also demonstrated the capability of the device in underwater imaging of marine species that exploit both color and polarization information.

6. Conclusion and outlook

Numerous researchers have succeeded in developing a variety of different types of bioinspired artificial eyes and photonic devices over the past decades. These accomplishments have been made possible by overcoming technical limitations from various angles. Many researchers in a wide range of 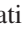fields have tried a variety of different approaches to duplicating the functions of natural eyes. Up till now, many technical issues have been solved thanks to the great effort and the technological progress in a multiplicity of areas such as materials science, mechanical and electrical engineering, and many others. As a result, researchers have successfully demonstrated artificial optical components inspired from animal eyes, including tunable lenses and irises, curved image sensors with single lenses or MLAs, microlens or micromirror arrays on flat or curved surfaces, MLAs coupled with waveguides, ARS, MLAs with focal length tunability, photosensitivity enhancers, and polarization imaging sensors. The distinct features of natural eyes have inspired researchers and brought about enormous achievements in the broad field of science and technology.

The significant progress in the bioinspired technologies can lead to the development of next-generation photonic devices. Since most of previous works focused on studying or reproducing a specific function of natural eyes, combining two or more functions in a single device is a potential approach. Furthermore, new technical issues have to be solved due to the broad applications of photonic devices. For example, in the biomedical applications, the researchers have to consider biocompatibility of the materials and the operating environment of the devices. Miniaturized and high quality imaging or lighting devices could potentially meet the demands of the biomedical field (e.g. endoscopy, laparoscopy, and robotic surgery). The bioinspired photonic devices have a huge potential and will no doubt advance optics, photonics, optoelectronics, robotics, and biomedical engineering.

ORCID iDs

Jae-Jun Kim ⓘ https://orcid.org/0000-0003-0722-3402
Hewei Liu ⓘ https://orcid.org/0000-0002-2977-1349
Alireza Ousati Ashtiani ⓘ https://orcid.org/0000-0001-9272-1929
Hongrui Jiang ⓘ https://orcid.org/0000-0001-8468-5454

References

[1] Land M F and Nilsson D-E 2012 *Animal Eyes* (Oxford: Oxford University Press)

[2] Chen A H, O'Leary D J and Howell E R 2000 Near visual function in young children. Part I: near point of convergence. Part II: amplitude of accommodation. Part III: near heterophoria *Ophthalmic Physiol. Opt.* **20** 185–98

[3] Charman W N 2008 The eye in focus: accommodation and presbyopia *Clin. Exp. Optom.* **91** 207–25

[4] Mathôt S 2018 Pupillometry: psychology, physiology, and function *J. Cogn.* **1** 1–23

[5] Kirschfeld K 1976 The resolution of lens and compound eyes *Neural Principles in Vision* ed F Zettler and R Weiler (Berlin: Springer) 354–70

[6] Franceschini N, Ruffier F and Serres J 2007 A bio-inspired flying robot sheds light on insect piloting abilities *Curr. Biol.* **17** 329–35

[7] Völkel R, Eisner M and Weible K J 2003 Miniaturized imaging systems *Microelectron. Eng.* **67–8** 461–72

[8] Dong L, Agarwal A K, Beebe D J and Jiang H 2006 Adaptive liquid microlenses activated by stimuli-responsive hydrogels *Nature* **442** 551–4

[9] Dong L, Agarwal A K, Beebe D J and Jiang H 2007 Variable-focus liquid microlenses and microlens arrays actuated by thermoresponsive hydrogels *Adv. Mater.* **19** 401–5

[10] Dong L and Jiang H 2006 pH-adaptive microlenses using pinned liquid–liquid interfaces actuated by pH-responsive hydrogel *Appl. Phys. Lett.* **89** 211120

[11] Zeng X and Jiang H 2008 Tunable liquid microlens actuated by infrared light-responsive hydrogel *Appl. Phys. Lett.* **93** 151101

[12] Zeng X, Li C, Zhu D, Cho H J and Jiang H 2010 Tunable microlens arrays actuated by various thermo-responsive hydrogel structures *J. Micromech. Microeng.* **20** 115035

[13] Zeng X, Smith C T, Gould J C, Heise C P and Jiang H 2011 Fiber endoscopes utilizing liquid tunable-focus microlenses actuated through infrared light *J. Microelectromech. Syst.* **20** 583–93

[14] Zhu D, Lo C-W, Li C and Jiang H 2012 Hydrogel-based tunable-focus liquid microlens array with fast response time *J. Microelectromech. Syst.* **21** 1146–55

[15] Zhu D, Li C, Zeng X and Jiang H 2010 Tunable-focus microlens arrays on curved surfaces *Appl. Phys. Lett.* **96** 081111

[16] Duan J, Liang X, Zhu K, Guo J and Zhang L 2017 Bilayer hydrogel actuators with tight interfacial adhesion fully constructed from natural polysaccharides *Soft Matter* **13** 345–54

[17] Wirthl D *et al.* 2017 Instant tough bonding of hydrogels for soft machines and electronics *Sci. Adv.* **3** e1700053

[18] Zhang W, Zappe H and Seifert A 2012 Polyacrylate tunable microlens with on-chip thermopneumatic actuation *Int. Conf. on Optical MEMS and Nanophotonics* (OMN) 57–8

[19] De Volder M and Reynaerts D 2010 Pneumatic and hydraulic microactuators: a review *J. Micromech. Microeng.* **20** 043001

[20] Zhang W, Aljasem K, Zappe H and Seifert A 2011 Completely integrated, thermo-pneumatically tunable microlens *Opt. Express* **19** 2347–62

[21] Lee J K, Park K-W, Lim G, Kim H-R and Kong S H 2012 Variable-focus liquid lens based on a laterally-integrated thermopneumatic actuator *J. Opt. Soc. Korea* **16** 22–8

[22] Ousati Ashtiani A and Jiang H 2013 Thermally actuated tunable liquid microlens with sub-second response time *Appl. Phys. Lett.* **103** 111101

[23] Ousati Ashtiani A and Jiang H 2014 Tunable microlens actuated via a thermoelectrically driven liquid heat engine *J. Appl. Phys.* **115** 243103

[24] Berge B and Peseux J 2000 Variable focal lens controlled by an external voltage: an application of electrowetting *Eur. Phys. J.* E **3** 159–63

[25] Berge B 2005 Liquid lens technology: principle of electrowetting based lenses and applications to imaging *18th IEEE Int. Conf. on Micro Electro Mechanical Systems* 227–30

[26] Lu Y-S, Tu H, Xu Y and Jiang H 2013 Tunable dielectric liquid lens on flexible substrate *Appl. Phys. Lett.* **103** 261113

[27] Yang C-C, Tsai C G and Yeh J A 2010 Miniaturization of dielectric liquid microlens in package *Biomicrofluidics* **4** 043006

[28] Kuiper S and Hendriks B H W 2004 Variable-focus liquid lens for miniature cameras *Appl. Phys. Lett.* **85** 1128–30

[29] Cheng C-C and Yeh J A 2007 Dielectrically actuated liquid lens *Opt. Express* **15** 7140–5

[30] Mugele F and Baret J-C 2005 Electrowetting: from basics to applications *J. Phys.: Condens. Matter* **17** R705–74

[31] Hendriks B H W, Kuiper S, Van As M A J, Renders C A and Tukker T W 2005 Electrowetting-based variable-focus lens for miniature systems *Opt. Rev.* **12** 255–9

[32] Ousati Ashtiani A and Jiang H 2016 Design and fabrication of an electrohydrodynamically actuated microlens with areal density modulated electrodes *J. Micromech. Microeng.* **26** 015004

[33] Chung S K, Zhao Y and Cho S K 2008 On-chip creation and elimination of microbubbles for a micro-object manipulator *J. Micromech. Microeng.* **18** 095009

[34] Bauer F, Fousson E and Zhang Q M 2006 Recent advances in highly electrostrictive P(VDF-TrFE-CFE) terpolymers *IEEE Trans. Dielectr. Electr. Insul.* **13** 1149–54

[35] Xia F, Cheng Z, Xu H, Li H, Zhang Q, Kavarnos G J, Ting R Y, Abdel-Sadek G and Belfield K D 2002 High electromechanical responses in a poly(vinylidene fluoride-trifluoroethylene-chlorofluoroethylene) terpolymer *Adv. Mater.* **14** 1574–7

[36] Xia F, Tadigadapa S and Zhang Q M 2006 Electroactive polymer based microfluidic pump *Sensors Actuators* A **125** 346–52

[37] Choi S T, Lee J Y, Kwon J O, Lee S and Kim W 2011 Varifocal liquid-filled microlens operated by an electroactive polymer actuator *Opt. Lett.* **36** 1920–2

[38] Carpi F, Frediani G, Turco S and De Rossi D 2011 Bioinspired tunable lens with muscle-like electroactive elastomers *Adv. Funct. Mater.* **21** 4152–8

[39] Maffli L, Rosset S, Ghilardi M, Carpi F and Shea H 2015 Ultrafast all-polymer electrically tunable silicone lenses *Adv. Funct. Mater.* **25** 1656–65

[40] Wei K, Domicone N W and Zhao Y 2014 Electroactive liquid lens driven by an annular membrane *Opt. Lett.* **39** 1318–21

[41] Jin B, Lee J-H, Zhou Z, Zhang G, Lee G-B, Ren H and Nah C 2016 Adaptive liquid lens driven by elastomer actuator *Opt. Eng.* **55** 017107

[42] Shian S, Diebold R M and Clarke D R 2013 Tunable lenses using transparent dielectric elastomer actuators *Opt. Express* **21** 8669–76

[43] Lee S W and Lee S S 2007 Focal tunable liquid lens integrated with an electromagnetic actuator *Appl. Phys. Lett.* **90** 121129

[44] Kidger M J 2001 *Fundamental Optical Design* (Bellingham: SPIE press) (https://doi.org/10.1117/3.397107)

[45] Iwert O and Delabre B 2010 The challenge of highly curved monolithic imaging detectors *Proc. SPIE* **7742** 774227

[46] Rim S-B, Catrysse P B, Dinyari R, Huang K and Peumans P 2008 The optical advantages of curved focal plane arrays *Opt. Express* **16** 4965–71

[47] Milojkovic P and Mait J N 2012 Space-bandwidth scaling for wide field-of-view imaging *Appl. Opt.* **51** A36–47

[48] Swain P K, Channin D J, Taylor G C, Lipp S A and Mark D S 2004 Curved CCDs and their application with astronomical telescopes and stereo panoramic cameras *Proc. SPIE* **5301** 109–29

[49] Reshidko D and Sasian J 2015 Optical analysis of miniature lenses with curved imaging surfaces *Appl. Opt.* **54** E216–23

[50] Stamenov I, Agurok I P and Ford J E 2013 Optimization of two-glass monocentric lenses for compact panoramic imagers: general aberration analysis and specific designs: erratum *Appl. Opt.* **52** 5348–49

[51] Hung P J, Jeong K, Liu G L and Lee L P 2004 Microfabricated suspensions for electrical connections on the tunable elastomer membrane *Appl. Phys. Lett.* **85** 6051–3

[52] Ko H C *et al.* 2008 A hemispherical electronic eye camera based on compressible silicon optoelectronics *Nature* **454** 748–53

[53] Jung I, Xiao J, Malyarchuk V, Lu C, Li M, Liu Z, Yoon J, Huang Y and Rogers J A 2011 Dynamically tunable hemispherical electronic eye camera system with adjustable zoom capability *Proc. Natl Acad. Sci.* **108** 1788–93

[54] Jung I, Shin G, Malyarchuk V, Ha J S and Rogers J A 2010 Paraboloid electronic eye cameras using deformable arrays of photodetectors in hexagonal mesh layouts *Appl. Phys. Lett.* **96** 021110

[55] Jin H-C, Abelson J R, Erhardt M K and Nuzzo R G 2004 Soft lithographic fabrication of an image sensor array on a curved substrate *J. Vac. Sci. Technol.* B **22** 2548–51

[56] Dinyari R, Rim S-B, Huang K, Catrysse P B and Peumans P 2008 Curving monolithic silicon for nonplanar focal plane array applications *Appl. Phys. Lett.* **92** 091114

[57] Iwert O, Ouellette D, Lesser M and Delabre B 2012 First results from a novel curving process for large area scientific imagers *Proc. SPIE* **8453** 84531W

[58] Dumas D, Fendler M, Baier N, Primot J and le Coarer E 2012 Curved focal plane detector array for wide field cameras *Appl. Opt.* **51** 5419–24

[59] Guenter B *et al.* 2017 Highly curved image sensors: a practical approach for improved optical performance *Opt. Express* **25** 13010–23

[60] Itonaga K *et al.* 2014 A novel curved CMOS image sensor integrated with imaging system *2014 Symp. on VLSI Technology (VLSI-Technology): Digest of Technical Papers* (https://doi.org/10.1109/VLSIT.2014.6894341)

[61] Müller P, Spengler N, Zappe H and Mönch W 2010 An optofluidic concept for a tunable micro-iris *J. Microelectromech. Syst.* **19** 1477–84

[62] Ren H and Wu S-T 2010 Optical switch using a deformable liquid droplet *Opt. Lett.* **35** 3826–28

[63] Yu C-C, Ho J-R and Cheng J-W J 2014 Tunable liquid iris actuated using electrowetting effect *Opt. Eng.* **53** 057106

[64] Seo H W, Chae J B, Hong S J, Rhee K, Chang J-H and Chung S K 2015 Electromagnetically driven liquid lens *Sensors Actuators* A **231** 52–8

[65] Hsu T-C, Lu C-H, Huang Y-T, Shih W-P and Chen W-S 2011 Concentric polymer-dispersed liquid crystal rings for light intensity modulation *Sensors Actuators* A **169** 341–6

[66] Shareef F J, Sun S, Kotecha M, Kassem I, Azar D and Cho M 2016 Engineering a light-attenuating artificial iris *Invest. Ophthalmol. Vis. Sci.* **57** 2195–202

[67] Na J-H, Park S C, Sohn Y and Lee S-D 2013 Realizing the concept of a scalable artificial iris with self-regulating capability by reversible photoreaction of spiropyran dyes *Biomaterials* **34** 3159–64

[68] Duparré J, Dannberg P, Schreiber P, Bräuer A and Tünnermann A 2004 Artificial apposition compound eye fabricated by micro-optics technology *Appl. Opt.* **43** 4303–10

[69] Duparré J, Dannberg P, Schreiber P, Bräuer A and Tünnermann A 2005 Thin compound-eye camera *Appl. Opt.* **44** 2949–56

[70] Brückner A, Duparré J, Dannberg P, Bräuer A and Tünnermann A 2007 Artificial neural superposition eye *Opt. Express* **15** 11922–33

[71] Li L and Yi A 2012 Design and fabrication of a freeform microlens array for a compact large-field-of-view compound-eye camera *Appl. Opt.* **51** 1843–52

[72] Gabor D 1940 UK Patent 541 753

[73] Hembd-Sölner C, Stevens R F and Hutley M C 1999 Imaging properties of the gabor superlens *J. Opt. A: Pure Appl. Opt.* **1** 94–102

[74] Stollberg K, Brückner A, Duparré J, Dannberg P, Bräuer A and Tünnermann A 2009 The Gabor superlens as an alternative wafer-level camera approach inspired by superposition compound eyes of nocturnal insects *Opt. Express* **17** 15747–59

[75] Brückner A, Duparré J, Leitel R, Dannberg P, Bräuer A and Tünnermann A 2010 Thin wafer-level camera lenses inspired by insect compound eyes *Opt. Express* **18** 24379–94

[76] Brückner A, Oberdörster A, Dunkel J, Reimann A, Müller M and Wippermann F 2014 Ultra-thin wafer-level camera with 720p resolution using micro-optics *Proc. SPIE* **9193** 91930W

[77] Dunkel J, Wippermann F, Brückner A, Reimann A, Müller M and Bräuer A 2014 Fabrication of refractive freeform array masters for artificial compound eye cameras *Proc. SPIE* **9130** 91300P

[78] Dunkel J, Wippermann F, Reimann A, Brückner A and Bräuer A 2015 Fabrication of microoptical freeform arrays on wafer level for imaging applications *Opt. Express* **23** 31915–25

[79] Duparré J, Schreiber P, Matthes A, Pshenay-Severin E, Bräuer A, Tünnermann A, Völkel R, Eisner M and Scharf T 2005 Microoptical telescope compound eye *Opt. Express* **13** 889–903

[80] Meyer J, Brückner A, Leitel R, Dannberg P, Bräuer A and Tünnermann A 2011 Optical cluster eye fabricated on wafer-level *Opt. Express* **19** 17506–19

[81] Keum D, Jang K-W, Jeon D S, Hwang C S H, Buschbeck E K, Kim M H and Jeong K-H 2018 Xenos peckii vision inspires an ultrathin digital camera *Light Sci. Appl.* **7** 80

[82] Tanida J, Kumagai T, Yamada K, Miyatake S, Ishida K, Morimoto T, Kondou N, Miyazaki D and Ichioka Y 2001 Thin observation module by bound optics (TOMBO): concept and experimental verification *Appl. Opt.* **40** 1806–13

[83] Kitamura Y *et al.* 2004 Reconstruction of a high-resolution image on a compound-eye image-capturing system *Appl. Opt.* **43** 1719–27

[84] Nitta K, Shogenji R, Miyatake S and Tanida J 2006 Image reconstruction for thin observation module by bound optics by using the iterative backprojection method *Appl. Opt.* **45** 2893–900

[85] Keum D, Jung H and Jeong K-H 2012 Planar emulation of natural compound eyes *Small* **8** 2169–73

[86] Kawata S, Sun H-B, Tanaka T and Takada K 2001 Finer features for functional microdevices *Nature* **412** 697–8

[87] Cumpston B H *et al.* 1999 Two-photon polymerization initiators for three-dimensional optical data storage and microfabrication *Nature* **398** 51–4

[88] Wu D, Wang J N, Niu L G, Zhang X L, Wu S Z, Chen Q D, Lee L P and Sun H B 2014 Bioinspired fabrication of high-quality 3D artificial compound eyes by voxel-modulation femtosecond laser writing for distortion-free wide-field-of-view imaging *Adv. Opt. Mater.* **2** 751–8

[89] Chen F, Liu H, Yang Q, Wang X, Hou C, Bian H, Liang W, Si J and Hou X 2010 Maskless fabrication of concave

microlens arrays on silica glasses by a femtosecond-laser-enhanced local wet etching method *Opt. Express* **18** 20334–43

[90] Liu H, Chen F, Yang Q, Qu P, He S, Wang X, Si J and Hou X 2012 Fabrication of bioinspired omnidirectional and gapless microlens array for wide field-of-view detections *Appl. Phys. Lett.* **100** 133701

[91] Bian H, Wei Y, Yang Q, Chen F, Zhang F, Du G, Yong J and Hou X 2016 Direct fabrication of compound-eye microlens array on curved surfaces by a facile femtosecond laser enhanced wet etching process *Appl. Phys. Lett.* **109** 221109

[92] Sherk T E 1978 Development of the compound eyes of dragonflies (Odonata). III. Adult compound eyes *J. Exp. Zool.* **203** 61–79

[93] Jeong K-H, Kim J and Lee L P 2006 Biologically inspired artificial compound eyes *Science* **312** 557–61

[94] Kuo W-K, Kuo G-F, Lin S-Y and Yu H H 2015 Fabrication and characterization of artificial miniaturized insect compound eyes for imaging *Bioinspir. Biomim.* **10** 056010

[95] Wang M, Wang T, Shen H, Zhao J, Zhang Z, Du J and Yu W 2016 Subtle control on hierarchic reflow for the simple and massive fabrication of biomimetic compound eye arrays in polymers for imaging at a large field of view *J. Mater. Chem.* C **4** 108–12

[96] Zhao F, Xie Y, He S, Fu S and Lu Z 2005 Single step fabrication of microlens arrays with hybrid HfO$_2$–SiO$_2$ sol-gel glass on conventional lens surface *Opt. Express* **13** 5846–52

[97] Vogt K 1980 Die Spiegeloptik des Flußkrebsauges *J. Comp. Physiol.* A **135** 1–19

[98] Jannson T, Kostrzewski A, Gertsenshteyn M, Grubsky V, Shnitser P, Agurok I, Bennahmias M, Lee K and Savant G 2007 Animal eyes in homeland security systems *Proc. SPIE* **6538** 65381R

[99] Jannson T and Gertsenshteyn M 2006 Hard x-ray focusing optics for concealed object detection *Proc. SPIE* **6213** 621302

[100] Angel J R P 1979 Lobster eyes as x-ray telescopes *Astrophys. J.* **233** 364–73

[101] Huang C-C, Wu X, Liu H, Aldalali B, Rogers J A and Jiang H 2014 Large-field-of-view wide-spectrum artificial reflecting superposition compound eyes *Small* **10** 3050–7

[102] Chapman H N, Nugent K A and Wilkins S W 1991 X-ray focusing using square channel-capillary arrays *Rev. Sci. Instrum.* **62** 1542–61

[103] Song Y M *et al.* 2013 Digital cameras with designs inspired by the arthropod eye *Nature* **497** 95–9

[104] Someya T 2013 *Stretchable Electronics* (Weinheim: Wiley-VCH)

[105] Floreano D *et al.* 2013 Miniature curved artificial compound eyes *Proc. Natl Acad. Sci.* **110** 9267–72

[106] Stavenga D G, Foletti S, Palasantzas G and Arikawa K 2006 Light on the moth-eye corneal nipple array of butterflies *Proc. R. Soc.* B **273** 661–7

[107] Clapham P B and Hutley M C 1973 Reduction of lens reflexion by the 'moth eye' principle *Nature* **244** 281–2

[108] Choi K, Park S H, Song Y M, Lee Y T, Hwangbo C K, Yang H and Lee H S 2010 Nano-tailoring the surface structure for the monolithic high-performance antireflection polymer film *Adv. Mater.* **22** 3713–8

[109] Choi K, Park S H, Song Y M, Cho C and Lee H S 2012 Robustly nano-tailored honeycomb structure for high-throughput antireflection polymer films *J. Mater. Chem.* **22** 17037–43

[110] Raut H K, Dinachali S S, He A Y, Ganesh V A, Saifullah M S M, Law J and Ramakrishna S 2013 Robust and durable polyhedral oligomeric silsesquioxane-based anti-reflective nanostructures with broadband quasi-omnidirectional properties *Energy Environ. Sci.* **6** 1929–37

[111] Kuo W-K, Hsu J-J, Nien C-K and Yu H H 2016 Moth-eye-inspired biophotonic surfaces with antireflective and hydrophobic characteristics *ACS Appl. Mater. Interfaces* **8** 32021–30

[112] Zhang J, Shen S, Dong X X and Chen L S 2014 Low-cost fabrication of large area sub-wavelength anti-reflective structures on polymer film using a soft PUA mold *Opt. Express* **22** 1842–51

[113] Galeotti F, Trespidi F, Timò G and Pasini M 2014 Broadband and crack-free antireflection coatings by self-assembled moth eye patterns *ACS Appl. Mater. Interfaces* **6** 5827–34

[114] Lee S H, Leem J W and Yu J S 2013 Transmittance enhancement of sapphires with antireflective subwavelength grating patterned UV polymer surface structures by soft lithography *Opt. Express* **21** 29298–303

[115] Wu F, Shi G, Xu H, Liu L, Wang Y, Qi D and Lu N 2013 Fabrication of antireflective compound eyes by imprinting *ACS Appl. Mater. Interfaces* **5** 12799–803

[116] Ji S, Park J and Lim H 2012 Improved antireflection properties of moth eye mimicking nanopillars on transparent glass: flat antireflection and color tuning *Nanoscale* **4** 4603–10

[117] Oh Y-J, Kim J-J and Jeong K-H 2014 Biologically inspired biophotonic surfaces with self-antireflection *Small* **10** 2558–63

[118] Heo S Y, Koh J K, Kang G, Ahn S H, Chi W S, Kim K and Kim J H 2014 Bifunctional moth-eye nanopatterned dye-sensitized solar cells: light-harvesting and self-cleaning effects *Adv. Energy Mater.* **4** 1300632

[119] Ko D-H, Tumbleston J R, Henderson K J, Euliss L E, DeSimone J M, Lopez R and Samulski E T 2011 Biomimetic microlens array with antireflective 'moth-eye' surface *Soft Matter* **7** 6404–7

[120] Zhu J, Hsu C-M, Yu Z, Fan S and Cui Y 2010 Nanodome solar cells with efficient light management and self-cleaning *Nano Lett.* **10** 1979–84

[121] Daglar B, Khudiyev T, Demirel G B, Buyukserin F and Bayindir M 2013 Soft biomimetic tapered nanostructures for large-area antireflective surfaces and SERS sensing *J. Mater. Chem.* C **1** 7842–8

[122] Li J, Zhu J and Gao X 2014 Bio-inspired high-performance antireflection and antifogging polymer films *Small* **10** 2578–82

[123] Park H, Shin D, Kang G, Baek S, Kim K and Padilla W J 2011 Broadband optical antireflection enhancement by integrating antireflective nanoislands with silicon nanoconical-frustum arrays *Adv. Mater.* **23** 5796–800

[124] Zhu J, Yu Z, Burkhard G F, Hsu C-M, Connor S T, Xu Y, Wang Q, McGehee M, Fan S and Cui Y 2009 Optical absorption enhancement in amorphous silicon nanowire and nanocone arrays *Nano Lett.* **9** 279–82

[125] Boden S A and Bagnall D M 2008 Tunable reflection minima of nanostructured antireflective surfaces *Appl. Phys. Lett.* **93** 133108

[126] Huang Y-F *et al.* 2007 Improved broadband and quasi-omnidirectional anti-reflection properties with biomimetic silicon nanostructures *Nat. Nanotechnol.* **2** 770–4

[127] Diedenhofen S L, Vecchi G, Algra R E, Hartsuiker A, Muskens O L, Immink G, Bakkers E P A M, Vos W L and Gómez Rivas J 2009 Broad-band and omnidirectional antireflection coatings based on semiconductor nanorods *Adv. Mater.* **21** 973–8

[128] Diedenhofen S L, Janssen O T A, Grzela G, Bakkers E P A M and Gómez Rivas J 2011 Strong geometrical dependence of the absorption of light in arrays of semiconductor nanowires *ACS Nano* **5** 2316–23

[129] Lee Y-J, Ruby D S, Peters D W, Mckenzie B B and Hsu J W P 2008 ZnO nanostructures as efficient antireflection layers in solar cells *Nano Lett.* **8** 1501–5

[130] Song Y M, Jang S J, Yu J S and Lee Y T 2010 Bioinspired parabola subwavelength structures for improved broadband antireflection *Small* **6** 984–7

[131] Chen J-D, Zhou L, Ou Q-D, Li Y-Q, Shen S, Lee S-T and Tang J-X 2014 Enhanced light harvesting in organic solar cells featuring a biomimetic active layer and a self-cleaning antireflective coating *Adv. Energy Mater.* **4** 1301777

[132] Song Y M, Jeong Y, Yeo C I and Lee Y T 2012 Enhanced power generation in concentrated photovoltaics using broadband antireflective coverglasses with moth eye structures *Opt. Express* **20** A916–23

[133] Jung H and Jeong K-H 2012 Monolithic polymer microlens arrays with antireflective nanostructures *Appl. Phys. Lett.* **101** 203102

[134] Wang T, Yu W, Li C, Zhang H, Xu Z, Lu Z and Sun Q 2012 Biomimetic compound eye with a high numerical aperture and anti-reflective nanostructures on curved surfaces *Opt. Lett.* **37** 2397–9

[135] Yanagishita T, Nishio K and Masuda H 2009 Anti-reflection structures on lenses by nanoimprinting using ordered anodic porous alumina *Appl. Phys. Express* **2** 022001

[136] Yanagishita T, Hidaka T, Suzuki M and Masuda H 2016 Polymer lenses with antireflection structures prepared using anodic porous alumina molds *J. Vac. Sci. Technol.* B **34** 021804

[137] Lee Y, Bae S-I, Eom J, Suh H-C and Jeong K-H 2018 Antireflective glass nanoholes on optical lenses *Opt. Express* **26** 14786–91

[138] Bae S-I, Lee Y, Seo Y-H and Jeong K-H 2019 Antireflective structures on highly flexible and large area elastomer membrane for tunable liquid-filled endoscopic lens *Nanoscale* **11** 856–61

[139] Song Y M, Park G C, Jang S J, Ha J H, Yu J S and Lee Y T 2011 Multifunctional light escaping architecture inspired by compound eye surface structures: from understanding to experimental demonstration *Opt. Express* **19** A157–65

[140] Li Y, Li F, Zhang J, Wang C, Zhu S, Yu H, Wang Z and Yang B 2010 Improved light extraction efficiency of white organic light-emitting devices by biomimetic antireflective surfaces *Appl. Phys. Lett.* **96** 153305

[141] Zhou L, Ou Q-D, Chen J-D, Shen S, Tang J-X, Li Y-Q and Lee S-T 2014 Light manipulation for organic optoelectronics using bio-inspired moth's eye nanostructures *Sci. Rep.* **4** 4040

[142] Kim J-J, Lee Y, Kim H G, Choi K-J, Kweon H-S, Park S and Jeong K-H 2012 Biologically inspired LED lens from cuticular nanostructures of firefly lantern *Proc. Natl Acad. Sci. USA* **109** 18674–8

[143] Kim J-J, Lee J, Yang S-P, Kim H G, Kweon H-S, Yoo S and Jeong K-H 2016 Biologically inspired organic light-emitting diodes *Nano Lett.* **16** 2994–3000

[144] Bay A, Cloetens P, Suhonen H and Vigneron J P 2013 Improved light extraction in the bioluminescent lantern of a *Photuris* firefly (Lampyridae) *Opt. Express* **21** 764–80

[145] Bay A, André N, Sarrazin M, Belarouci A, Aimez V, Francis L A and Vigneron J P 2013 Optimal overlayer inspired by *Photuris* firefly improves light-extraction efficiency of existing light-emitting diodes *Opt. Express* **21** A179–89

[146] Shahini A, Jin H, Zhou Z, Zhao Y, Chen P-Y, Hua J and Cheng M M-C 2017 Toward individually tunable compound eyes with transparent graphene electrode *Bioinspir. Biomim.* **12** 046002

[147] Wang L, Li F, Liu H, Jiang W, Niu D, Li R, Yin L, Shi Y and Chen B 2015 Graphene-based bioinspired compound eyes for programmable focusing and remote actuation *ACS Appl. Mater. Interfaces* **7** 21416–22

[148] Zeng H, Borteh H and Zhao Y 2011 A bioinspired 3D artificial compound eye with focus-tunable single lenses

Proc. 15th Int. Conf. Miniaturized Systems for Chemistry and Life Sciences (μTAS) 1980–2

[149] Wei K, Zeng H and Zhao Y 2014 Insect-human hybrid eye (IHHE): an adaptive optofluidic lens combining the structural characteristics of insect and human eyes *Lab Chip* **14** 3594–602

[150] Lee T-W 2009 *Military Technologies of the World* (Westport: Praeger Security International)

[151] Weissleder R, Tung C-H, Mahmood U and Bogdanov A 1999 *In vivo* imaging of tumors with protease-activated near-infrared fluorescent probes *Nat. Biotechnol.* **17** 375–8

[152] Hofmann M, Eggeling C, Jakobs S and Hell S W 2005 Breaking the diffraction barrier in fluorescence microscopy at low light intensities by using reversibly photoswitchable proteins *Proc. Natl Acad. Sci.* **102** 17565–9

[153] Morris P A, Aspden R S, Bell J E C, Boyd R W and Padgett M J 2015 Imaging with a small number of photons *Nat. Commun.* **6** 5913

[154] Boyce P B 1977 Low light level detectors for astronomy *Science* **198** 145–8

[155] Dickson J F 1976 On-chip high-voltage generation in MNOS integrated circuits using an improved voltage multiplier technique *IEEE J. Solid-State Circuits* **11** 374–8

[156] Wang X F, Uchida T, Coleman D M and Minami S 1991 A two-dimensional fluorescence lifetime imaging system using a gated image intensifier *Appl. Spectrosc.* **45** 360–6

[157] Lopez-Sanchez O, Lembke D, Kayci M, Radenovic A and Kis A 2013 Ultrasensitive photodetectors based on monolayer MoS_2 *Nat. Nanotechnol.* **8** 497–501

[158] Liu C-H, Chang Y-C, Norris T B and Zhong Z 2014 Graphene photodetectors with ultra-broadband and high responsivity at room temperature *Nat. Nanotechnol.* **9** 273–8

[159] Vashchenko V A and Sinkevitch V F 2008 *Physical Limitations of Semiconductor Devices* (New York: Springer)

[160] Liu H, Huang Y and Jiang H 2016 Artificial eye for scotopic vision with bioinspired all-optical photosensitivity enhancer *Proc. Natl Acad. Sci.* **113** 3982–5

[161] Kreysing M *et al* 2012 Photonic crystal light collectors in fish retina improve vision in turbid water *Science* **336** 1700–3

[162] Bandai K, Arikawa K and Eguchi E 1992 Localization of spectral receptors in the ommatidium of butterfly compound eye determined by polarization sensitivity *J. Comp. Physiol.* A **171** 289–97

[163] Bainbridge R and Waterman T H 1957 Polarized light and the orientation of two marine crustacea *J. Exp. Biol.* **34** 342–64

[164] Chiou T-H, Kleinlogel S, Cronin T, Caldwell R, Loeffler B, Siddiqi A, Goldizen A and Marshall J 2008 Circular polarization vision in a stomatopod crustacean *Curr. Biol.* **18** 429–34

[165] Kalayjian Z, Andreou A, Wolff L B and Williams J 1995 Integrated 1-D polarization imagers *Proc. of 29th Annual Conf. Information Science System* 163–8

[166] Kalayjian Z K, Andreou A G and Wolff L B 1997 1D polarisation contrast retina *Electron. Lett.* **33** 38–40

[167] Kalayjian Z K and Andreou A G 1999 A silicon retina for polarization contrast vision *IJCNN'99. Int. Joint Conf. on Neural Networks. Proc. (Cat. No. 99CH36339)* **4** 2329–32

[168] Hamamoto T, Toyota H and Kikuta H 2001 Microretarder array for imaging polarimetry in the visible wavelength region *Proc. SPIE* **4440** 293–300

[169] Momeni M and Titus A H 2006 An analog VLSI chip emulating polarization vision of octopus retina *IEEE Trans. Neural Netw.* **17** 222–32

[170] Andreou A G and Kalayjian Z K 2002 Polarization imaging: principles and integrated polarimeters *IEEE Sens. J.* **2** 566–76

[171] Zhang M, Wu X, Cui N, Engheta N and Van Der Spiegel J 2014 Bioinspired focal-plane polarization image sensor design: from application to implementation *Proc. IEEE* **102** 1435–49

[172] Tokuda T, Yamada H, Sasagawa K and Ohta J 2009 Polarization-analyzing CMOS image sensor with monolithically embedded polarizer for microchemistry systems *IEEE Trans. Biomed. Circuits Syst.* **3** 259–66

[173] Sarkar M, Bello D S S, Van Hoof C and Theuwissen A 2010 Integrated polarization analyzing CMOS image sensor for autonomus navigation using polarized light *Proc. 5th IEEE Int. Conf. Intell. Syst.* 224–9

[174] Sarkar M, San Segundo Bello D S S, Van Hoof C and Theuwissen A 2011 Integrated polarization analyzing CMOS image sensor for material classification *IEEE Sens. J.* **11** 1692–703

[175] Garcia M, Edmiston C, Marinov R, Vail A and Gruev V 2017 Bio-inspired color-polarization imager for real-time *in situ* imaging *Optica* **4** 1263–71

[176] Garcia M, Davis T, Blair S, Cui N and Gruev V 2018 Bioinspired polarization imager with high dynamic range *Optica* **5** 1240–6
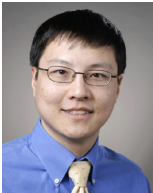
Hongrui Jiang received the B.S. degree in physics from Peking University, Beijing, China, and the M.S. and Ph.D. degrees in electrical engineering from Cornell University, Ithaca, NY, in 1999 and 2001, respectively. From 2001 to 2002, he was a Postdoctoral Researcher with the Berkeley Sensor and Actuator Center, University of California at Berkeley. He is currently the Vilas Distinguished Achievement Professor and the Lynn H. Matthias Professor in Engineering with the Department of Electrical and Computer Engineering, a Faculty Affiliate with the Department of Biomedical Engineering, the Department of Materials Science and Engineering, and the Department of Ophthalmology and Visual Sciences, and a Member of the McPherson Eye Research Institute with the University of Wisconsin–Madison. His research interests are in microfabrication technology, biological and chemical microsensors, microactuators, optical microelectromechanical systems, smart materials and micro-/nanostructures, lab-on-chip, and biomimetics and bioinspiration.

Dr. Jiang is a Fellow of the Institute of Physics, the Royal Society of Chemistry, the American Institute for Medical and Biological Engineering, and the Institute of Electrical and Electronics Engineers. He was a recipient of the US National Science Foundation CAREER Award and the US Defense Advanced Research Projects Agency Young Faculty Award in 2008, the H. I. Romnes Faculty Fellowship of the University of Wisconsin–Madison in 2011, the US National Institutes of Health Director's New Innovator Award in 2011, the Vilas Associate Award of the University of Wisconsin in 2013, and the Research to Prevent Blindness Stein Innovation Award in 2016.